QUANTUM ERROR MITIGATION AND AUTONOMOUS CORRECTION USING DISSIPATIVE ENGINEERING AND COUPLING TECHNIQUES

by

David Rodríguez Pérez

A thesis submitted to the Faculty and the Board of Trustees of the Colorado School of Mines in partial fulfillment of the requirements for the degree of Doctor of Philosophy (Physics).

Golden, Colorado

Date _____

Signed: _____

David Rodríguez Pérez

Signed: _____

Dr. Eliot Kapit
Thesis Advisor

Golden, Colorado

Date _____

Signed: _____

Dr. Frederic Sarazin
Professor and Head
Department of Physics

ABSTRACT

Realizations of quantum computing devices have progressed significantly, with each choice of architecture possessing advantages and disadvantages. Superconducting qubits are able to perform very fast gates, and benefit from standard manufacturing, but they suffer from very short coherence times compared to other architectures like trapped ions or spin qubits. This presents one of the greatest challenges towards achieving fault-tolerant quantum computing with superconducting architectures—improving coherence times. To that end, considerable research has been devoted to engineering qubits with longer lifetimes. Likewise, several error correction protocols have been introduced to provide a route towards fault-tolerance using noisy qubits, where a logical qubit is encoded in a collective state of many physical qubits, using stabilizer operations to detect and correct single qubit errors, thereby prolonging the logical state lifetime. However, the quantum resources required for the thousands of logical qubits needed for a factorization algorithm can be on the order of tens of millions of physical qubits for realistic error rates using surface codes. This would also require an immense amount of resources for the classical post-processing and decoding, a challenge for which there has not been a well established solution. The work in this thesis focuses on the implementation of logical qubits with autonomous error correction using dissipative engineering, in which high-coherence qubit devices are stabilized by coupling to lossy ancilla. The systems studied here have the advantage that a logical manifold can be encoded with a much smaller number of physical qubits compared to more traditional digital error correction codes, thus are called small logical qubits. This thesis presents results on improving autonomous error correction using numerically optimized pulse shaping for time parameterized coupling strength in different small logical qubits. It also presents results on a proposed scheme for error mitigation for the implementation of two-qubit gates—a dominant source of error in NISQ algorithms. Lastly, this thesis presents ongoing work with the simulation of dissipative engineering for variational quantum algorithms to improve algorithm performance.

TABLE OF CONTENTS

ABSTRACT iii

LIST OF FIGURES vii

LIST OF TABLES xvii

ACKNOWLEDGMENTS xviii

CHAPTER 1 QUANTUM ERROR CORRECTION 1

1.1 Modeling noise in qubits 3

1.2 Digital quantum error correction 6

1.2.1 Surface code 8

1.3 Autonomous quantum error correction 12

1.3.1 Cat codes 17

1.3.2 Very Small Logical Qubit 19

CHAPTER 2 IMPROVED AUTONOMOUS ERROR CORRECTION USING VARIABLE DISSIPATION IN SMALL LOGICAL QUBIT ARCHITECTURES 24

2.1 Introduction 25

2.2 Single-qubit stabilization 26

2.2.1 System 26

2.2.2 Results 29

2.3 Three-qubit flip code 32

2.3.1 System 32

2.3.2 Results 35

2.4 VSLQ 37

2.4.1 System 37

2.4.2 Results 40

2.5 Conclusion 43

2.6 Acknowledgements 45

CHAPTER 3 ERROR-DIVISIBLE TWO-QUBIT GATES 46
3.1 Introduction 46
3.1.1 Error divisibility 47
3.2 Principles of implementation 50
3.2.1 Example Waveforms 52
3.3 Hardware implementations 54
3.4 VQE example 55
3.5 Conclusions 58
3.6 Acknowledgements 58
CHAPTER 4 SURVEYING THE DETUNINGS PARAMETER SPACE FOR THE VSLQ-STAR 59
4.1 Defining a new codespace 59
4.2 Exploring the detuning space 65
4.2.1 Same transmon and resonator energies 66
4.2.2 Different transmon and resonator energies 71
4.3 Logical lifetime results 77
CHAPTER 5 DIGITIZING PULSE-SHAPED QUADRATURES IN THE RELAXATIONAL QUANTUM EIGENSOLVER 79
5.1 The Variational Quantum Eigensolver (VQE) 79
5.2 Adding driven dissipative engineering 82
5.3 Results using two-quadrature coupling 85
CHAPTER 6 CONCLUSIONS 91
6.1 Proposing a pulse-reset scheme 91
6.2 Error-divisible gates 92
6.3 The VSLQ-Star protocol 93
6.4 Relaxational quantum eigensolver 94
6.5 Future directions 95
REFERENCES 97

APPENDIX A MASTER EQUATION SIMULATOR FOR GENERAL STATES AND HAMILTONIANS 110

APPENDIX B SURFACE CODE MEASURE-CYCLE EXAMPLE 113

APPENDIX C SIMULATION DATA 117

C.1 Error-divisible two-qubit gates 117

APPENDIX D MISCELLANEOUS REFERENCES 121

D.1 Rotating Frame Hamiltonian derivation for two-qubit system 121

D.2 Circuit implementations for SWAP and iSWAP gates 123

D.3 The Clifford group 124

APPENDIX E PERMISSIONS FOR COPYRIGHTED MATERIAL 126

E.1 License for figure 1.6 126

E.2 License for chapter 2 126

LIST OF FIGURES

Figure 1.1 Bloch sphere representation of a qubit. The z basis is used as the computational basis by nomenclature, with x and y states represented in the z basis. Phase noise can be visualized as rotations around the axes by stray $\bar{\boldsymbol{\sigma}}$ operations (in green), and energy relaxation is visualized as the vector $|\psi\rangle$ relaxing towards the north pole $|0\rangle$ (in red). ... 1

Figure 1.2 Time evolution of a qubit that is flipping along the z-axis between the ground state $|0\rangle$ and the first excited state $|1\rangle$ in the z-basis, in the presence of noise (interactions with the environment). This noise causes a loss in qubit coherence that is described by an exponential decay. From this exponential fit, the qubit lifetime T_1 is defined. 2

Figure 1.3 The surface code consists of n data qubits and $(n-1)$ stabilizer qubits (white and black dots, respectively). (a) Each data qubit is coupled to four stabilizer qubits, and each stabilizer qubit is coupled to four data qubits, except at the boundary where data qubits are coupled to two or three stabilizer qubits and stabilizer qubits are coupled to three data qubits (you cannot have a stabilizer qubit coupled to two data qubits). Operations on the logical qubit are done by chains of operations connecting the boundaries (X_L in blue and magenta, Z_L in red). Both (b) and (c) show error-detection cycles for X- and Z-error syndromes, in which the data and stabilizer qubits go through a series of CNOT entangling gates. (b) One Z-stabilizer qubit is the target qubit for CNOTs with data qubits d_1, d_2, d_3, and d_4, whereas (c) an X-measure qubit is the control qubit for CNOTs with data qubits d_1, d_2, d_3, d_4. 9

Figure 1.4 A simplified example of a high-coherence qubit device (loss rate Γ_q) and a lossy linear resonator (Γ_r), demonstrating the always-on, off-resonant drive mechanism that autonomously increases the occupation probability of the first-excited state of the qubit device. By driving the transition $|0_q 0_r\rangle \rightarrow |1_q 1_r\rangle$ (blue line), the nonlinearity δ ensures that it is off-resonant with $|1_q 0_r\rangle \rightarrow |2_q 1_r\rangle$ (opaque blue), leaving the target state $|1_q 0_r\rangle$ unchanged. The procedure follows the steps in the opaque orange region—1. The qubit device experiences a photon loss at a rate Γ_q (red), which is ideally low relative to Γ_r. 2. The always-on drive is resonant with $|0_q 0_r\rangle \rightarrow |1_q 1_r\rangle$, and induces transitions between the two states. 3. The lossy resonator undergoes photon losses at a fast rate Γ_r (green, $\Gamma_r \gg \Gamma_q$), inducing $|1_q 1_r\rangle \rightarrow |1_q 0_r\rangle$ with high likelihood. This returns the system to the original state. Spurious occupations of higher-energy states in the resonator can safely be ignored due to the high decay rate. And finally, note that this mechanism can be applied to "correct" transitions into other unwanted states—for example, constantly driving a photon exchange resonant with the transition $|2_q 0_r\rangle \rightarrow |1_q 1_r\rangle$ would correct leakage. 13

Figure 1.5 As a classical analogy, quantum state stabilization by a continuous drive with a non-Markovian reservoir [1] is much like Kapitza's pendulum. Here, we take a rigid pendulum, which has two equilibrium states—a stable equilibrium point when pointing straight down, and an unstable equilibrium point when pointing straight up. By driving fast, constant oscillations so that the pendulum bounces up and down, the straight up, unstable equilibrium point is stabilized. 15

Figure 1.6 Bloch sphere representation of cat code logical states, reproduced with permission from [2]. The states $|\pm\alpha\rangle$ are represented as Wigner functions for $\alpha = 2$. The logical space is defined as $\{|0_L\rangle, |1_L\rangle\} \rightarrow \{|+\rangle, |-\rangle\}$. 17

Figure 1.7 Circuit diagram for an implementation of the VSLQ, which consists of two high-coherence transmons (labeled l and r in blue) and two lossy resonators (Sl and Sr in red). The coupling mechanism between the transmons is a four-photon exchange, and a two-photon pump for the transmon-resonator coupling. The error correction steps are illustrated on the right: 1. (Blue) The state is initially stabilized in the logical manifold with the continuous 4-photon exchange term $\tilde{X}_l\tilde{X}_r$, $\tilde{X} \rightarrow a^\dagger a^\dagger + aa$. 2. (Red) Photon loss experienced from the right transmon at a rate $2\Gamma_P$, which is ideally low. 3. (Orange) Transmon-resonator drive $\Omega(a_r^\dagger a_{Sr}^\dagger + a_r a_{Sr})$ exites for the transmon and resonator. Like in figure 1.4, this operation is off-resonant except in the event of a photon loss in the primary transmon. 4. (Green) Photon loss in the resonator at rate Γ_S, which is ideally high. With high likelihood, the resonator decays back to its ground state before the driven transmon-resonator coupling returns to the error state. 19

Figure 2.1 Scheme for the pulse-reset cycles. We denote the coupling duration as t_p (green), in which the qubit device and resonator are coupled using an optimized pulse shape. The reset cycle, t_r (red), is determined using a simple scan over different values to determine what gives the lowest residual error rate for each different T_1. We denote the loss rates as Γ_r for the resonator (or lossy qubit) and Γ_q for the qubit (or high-coherence qubit device), and the coupling strength as Ω. During t_p we set $\Gamma_r = \Gamma_q$ and $\Omega = \Omega_{opt}(t)$, while during t_r we have $\Gamma_r \gg \Gamma_q$ and $\Omega = 0$. It is assumed that qubit reset protocols, such as the one described in [3], can be performed efficiently, giving us an effective $\Gamma_r \gg \Gamma_q$..... 27

Figure 2.2 A high-coherence qubit device coupled to a lossy qubit or resonator with a coupling strength Ω. (a) An energy level diagram of the system. We only consider the ground state and first excited state of the resonator due to its lossy nature, making occupations of any higher states extremely unlikely. The protocol follows a photon loss in the primary qubit device (1), followed by the coupled excitation of both qubit device and resonator at strength Ω (2), and finally the relaxation of the resonator (3). (b) Optimized pulse shape for the operation $|0_q 0_r\rangle \rightarrow |1_q 1_r\rangle$ from a gradient ascent optimization. We let $N = 20$ in Eq. (2.3), and initialize $c_1^x = 2\pi \times 20$ MHz, $c_{n\neq 1}^x = 0$, and all $c_n^y = 0$, letting them vary by ϵ until we achieve a target state fidelity of 0.9989. All photon loss is turned off in this optimization, with the goal of trying to minimize errors induced by this mechanism itself. (c) We track the occupation probabilities of the transitions $|0_q 0_r\rangle \rightarrow |1_q 1_r\rangle$ (blue), $|1_q 0_r\rangle \rightarrow |1_q 0_r\rangle$ (orange), and $|1_q 0_r\rangle \rightarrow |2_q 1_r\rangle$ (green) from the qubit-resonator coupling (for compactness, the legend labels forego the subscripts: $|n_q m_r\rangle \equiv |nm\rangle$). The goal is to excite both qubit device and resonator in the event of a photon loss, leaving the target state unchanged while minimizing off-resonant transitions into the leakage state. 28

Figure 2.3 Residual error rate scaling with the fidelity calculated at the end of one pulse-reset cycle. 32

Figure 2.4 The effects of the $\Omega_y(t)$ terms on off-resonant, blue-sideband transitions for $\delta = 2\pi \times \{100, 200, 350\}$ MHz. There is a clear correlation between the effective oscillating counterterm and the size of δ. This is shown by tracking the occupation of the target state $|1_q 0_r\rangle$ (bottom plots), as well as the leakage state $|2_q 1_r\rangle$ in Fig. 2.2(c), having initialized in the target state $|1_q 0_r\rangle$. 33

Figure 2.5 Results for the three qubit code using $J = 2\pi \times 20$ MHz and $\Gamma_R = 30\ \mu\text{s}^{-1}$. (a) The optimized pulse shape for the target operations in Eq. (2.7), as well as (b) tracking the occupation probability for $|000\rangle_P$, where a final operation fidelity of 0.99999635 is achieved. Note that the states in the legend are only the primary qubits subspace and that the operation evolution is without decoherence. (c) Improvement factor T_L/T_E for the states $|000\rangle_P$ and $|111\rangle_P$, with increasing error times T_E. The state evolutions for these last results do include decoherence. Results in (a) and (b) were obtained with no bit-flip errors, while results in (c) do include bit=flip errors. 36

Figure 2.6 A possible implementation of the logical qubit, similar to [4]. The high-coherence primary qubits are in blue boxes, and the lossy resonators (or qubits) are in red boxes. The approximated rotating wave Hamiltonian [Eq. (2.9)] is achieved by modulating the flux drives in the diagram. We refer to the elements of this circuit as shadow left and shadow right (Sl and Sr respectively) for the lossy resonators (red boxes), and simply left and right (l and r) for the primary qubits (blue boxes)..... 37

Figure 2.7 Results for the VSLQ. (a) Optimized $\Omega_x(t)$ and $\Omega_y(t)$ pulse shapes. (b) High-fidelity target operation of 0.99991 while leaving the target states unchanged. (c) We see the effects of lifetimes for X_L eigenstates and Y_L eigenstates, using definitions from [4]. Blue and green are the improvement factors using fixed operating parameters (Table 2.1) for the X_L and Y_L eigenstates, respectively, while orange and red are the improvement factors using pulse-reset cycles. Again, (a) and (b) do not include decoherence, while (c) does..... 40

Figure 2.8 Short-time evolution for the VSLQ X_L eigenstates (left) and Y_L eigenstates (right). We compare using fixed parameters from Table 2.1 versus using pulse-reset (flushed) cycles for $T_1 = 30, 60$ μs. 41

Figure 3.1 Illustration of our proposed error divisibility protocol. (a) Two-qubit rotation θ_0 at gate time t_g, along with fractional rotations θ_0/n at corresponding gate times t_g/n. Note that these waveforms are only meant to demonstrate the idea of error-divisible fractional rotations at fractional gate times, and do not represent actual waveforms (amplitudes and frequencies—shown in (b)—can be different for each partial gate). (b) Example gate strength waveform for achieving error divisibility using a Gaussian gate envelope superimposed with a fast-oscillating counterterm. (c) Corresponding probability of gate $U(t)$ inducing transitions outside of $|11\rangle$ throughout the gate evolution in (b), where $U(t) = T\exp\left(-2\pi i \int_0^{t_g} \Omega(t)\left(|01\rangle\langle 10| + |10\rangle\langle 01|\right) dt\right)$ with coupling strength $\Omega(t)$ like in (b). An ideal exchange operation would preserve unity throughout the gate, but accounting for nonlinear leakage states, we see off-resonant transitions outside of $|11\rangle$, creating these dips in (c), the maximum indicated by the red-dashed. In typical operating regimes, the coupling strength in (b) is on the order of tens of MHz, $t_g \approx 30$ ns, and the maximum dip from unity—which varies by the target rotation—can be $< 10^{-2}$ for appropriate parameter choices. 49

Figure 3.2 Waveforms given by equation 3.4 for different rotations of iSWAP (top) and XX (bottom) gates. Waveforms for equation 3.4a and equation 3.4b are labelled simply as "cos" and "tanh", respectively, in the legend. The first row of both iSWAP and XX waveforms use $\alpha = 2$ in equation 3.3, while the bottom rows use $\alpha = 1$ to restrict the waveforms' positivity. The full rotation waveforms are on the far left, subsequent plots reduce the target rotation and corresponding gate time by the fractional series $\{3/4,\ 1/2,\ 1/4,\ 1/6,\ 1/8,\ 1/12\}$ 51

Figure 3.3 Intrinsic gate error results for fractional gate rotations for iSWAP (top, 36 ns gate for full π rotation) and XX (bottom, 24 ns for full π rotation) gates using both positive-definite (pos) and freely oscillating gate envelopes equation 3.4a (cos) and equation 3.4b (tanh). For fractional iSWAP gates, we achieve a gate error $< 10^{-4}$ down to $1/8^{\text{th}}$ of a gate using tanh envelopes and $1/6^{\text{th}}$ for XX gates..... 52

Figure 3.4 Circuit diagram for a single layer of VQE implementing the Hamiltonian equation 3.9 using six qubits. The "θ" labels next to the iSWAP and CPHASE gates denote their partial rotations by angle θ. 55

Figure 3.5 Comparisons for VQE percent of ground state results using a stock gate set (blue square), continuous gates (orange star), and the proposed error-divisible gate scheme (green triangle). 56

Figure 4.1 Four-point star illustration of the Hamiltonian in equation 4.18. The codewords for this protocol are all stabilized using two-photon processes with the $|11\rangle$ state as a sort of intermediary state to achieve an effective four-photon process. The $|20\rangle - |02\rangle$ codeword is stabilized using red-sideband transmon-transmon couplings detuned by ν_0, while the $|22\rangle - |00\rangle$ codeword is stabilized using blue-sideband transmon-transmon couplings, detuned by ν_1. This helps illustrate the fact that including the detunings for transitions with the $|11\rangle$ state does not actually change the energies of the codewords themselves. This visual mapping motivates the name for this new protocol—the VSLQ-star..... 63

Figure 4.2 Energy illustration for eigenstates of interest for the VSLQ-star Hamiltonian. We see on the left that the codewords for $|0_L\rangle$ (blue box) and $|1_L\rangle$ (red box) are energetically separated from states containing $|11\rangle$ ($\pm 2W$ energies), and are degenerate with a third eigenstate $|\psi\rangle$ (green box). This third degenerate state spoils error correction, so we include detunings ν_0 and ν_1 to break the three-fold degeneracy and separate the $|\psi\rangle$ eigenstate from the codewords. Imperatively, the codewords $|0_L\rangle \equiv |22\rangle - |00\rangle$ and $|1_L\rangle \equiv |20\rangle - |02\rangle$ are still degenerate zero-energy eigenstates, now separated from the third states and still separated from the $|11\rangle$ eigenstates, allowing proper error correction to the appropriate parent logical states in the event of a photon loss. The energy shifts for the $\pm 2W$ eigenstates are simply denoted by $\Delta^{\pm}_{\nu_0,\nu_1}$ and $\Delta^{\psi}_{\nu_0,\nu_1}$ for the $|\psi\rangle$ eigenstate to indicate that they have been shifted by some amounts which are not linearly related to each other. This only illustrates the core idea that the third eigenstate $|\psi\rangle$ is now separated from the codewords, and that the detunings maintain an energy separation between the codewords and the $\pm 2W$ eigenstates. 64

Figure 4.3 Detunings space for $|0_L\rangle$. Note the preference for $\nu_0 \neq -\nu_1$, as well as a strong preference for $\nu_1 \approx 0$ with arbitrary ν_0. 66

Figure 4.4 Detunings space for $|1_L\rangle$. While still seeing the preference $\nu_0 \neq -\nu_1$, we also now see $\nu_0 \neq \nu_1$. Contrary to what is observed in figure 4.3, there is an almost near opposite preference for $\nu_0 = 0$ and arbitrary ν_1. This is consistent to what is expected from the applications of ν_0 and ν_1 to the different two-photon processes. 67

Figure 4.5 Detunings space for $|+_L\rangle = |0_l\rangle + |1_L\rangle$ (left), and $|-_L\rangle = |0_L\rangle - |1_L\rangle$ (right). Note that they are identical spaces (with the simulated resolution). The preference for $\nu_0 \neq \pm\nu_1$ is consistent with the analysis in section 4.1, and results are effectively the same as averaging the results from figures 4.3 and 4.4. 67

Figure 4.6 Looking at a different choice of coupling strength Ω, we see a more generous choice of detunings to achieve a big improvement in the logical lifetimes for $|+_L\rangle$..... 68

Figure 4.7 Using a smaller energy scale W, there is a very noticeable performance hit to the $|+_L\rangle$ logical lifetime. 69

Figure 4.8 Using a smaller Ω for $W = 5$ MHz gives a very noticeable improvement. While these lifetimes are still shorter of the ones observed in figures 4.5 and 4.6, it is a very dramatic improvement over the results in figure 4.7 (drawing attention to the color scale). 70

Figure 4.9 One last check using an even smaller drive for the coupling strength Ω while maintaining a primary transmons drive $W = 5$ MHz. This gains the benefit of less sensitivity to the detunings, but the logical lifetime improvement is not quite as it is in figure 4.7. 71

Figure 4.10 Looking at the detunings space using weak drives. Logical state lifetimes are longer than the constituent transmon lifetimes, and are somewhat consistent with the lifetimes observed using weak drives in section 4.2.1. 72

Figure 4.11 Increasing the transmon-resonator coupling strength to $\Omega = 0.5$ MHz. There isn't a significantly observed increase in logical lifetime performance compared to figure 4.10. 73

Figure 4.12 Increasing the transmon-resonator coupling further to $\Omega = 1.0$ MHz shows a very significant performance hit to the logical lifetimes compared to figures 4.10 and 4.11. Further, the preferred detunings here are $\nu_0 = \nu_1 = 0$, making this protocol basically insufficient at this choice of drives. 73

Figure 4.13 Detunings space using a stronger main drive W with weak coupling drive. Logical state lifetimes are consistent with the lifetimes observed using a weaker main drive $W = 2$ MHz. 74

Figure 4.14 Increasing the transmon-resonator coupling strength to $\Omega = 0.5$ MHz. There is a much more generous improvement in the logical lifetime over the single transmon lifetime, as well as the logical lifetimes in figure 4.13. . 75

Figure 4.15 Increasing the transmon-resonator coupling further to $\Omega = 1.0$ MHz shows a slight performance hit to the logical lifetimes compared to figure 4.14, but a handsome improvement over lifetimes in figure 4.13. 76

Figure 4.16 Logical lifetimes for $|0_L\rangle$ at different choices of drives and detunings. Detunings were chosen based on results in section 4.2.2. 77

Figure 4.17 Logical lifetimes for $|1_L\rangle$, where we see the same level of improvement as in figure 4.16. 78

Figure 4.18 Logical lifetimes for $|+_L\rangle$. Response to the choice of drives and detunings is inline with what is observed in figures 4.16 and 4.17. 78

Figure 5.1 Schematic for the idea behind the variational quantum eigensolver using n Trotter steps. A quantum state is initialized and fed through the quantum circuit highlighted in green. Examples of what the Trotter steps can look like are in equation 5.8, and figure 5.2. At the end of the quantum circuit, the expectation value of use case operations are measured with the final state. Afterwards, using classical post-processing, highlighted in red, provides feedback for re-running the quantum circuit. This feedback can entail classical optimization over a parameter space characteristic of the quantum system to better approximate the problem Hamiltonian ground state. 80

Figure 5.2 Illustration of modifications to a standard VQE setup as shown in figure 5.1. We have added a set of lossy shadow resonators to use for passive error correction. The protocol starts out the same as traditional VQE, but for a total number of Trotter steps n_f, we specify a Trotter step n after which we begin the driven-dissipative protocol between the primary qubits $|q_N\rangle$ and the lossy resonators $|s_{N_S}\rangle$ that has been a big focus of this thesis. The example Trotter step in this figure is the same as that from section 3.4, and is the problem Hamiltonian for results in this section. We also illustrate how the digitization of the DRAG-like qubit-resonator coupling is done, where the coupling strength Ω is turned into two quadratures Ω_x (green) and Ω_y (orange), which take on time-parameterized sinusoidal waveforms, similar to work done in chapter 2. 82

Figure 5.3 Parameter scans for the primary-shadow coupling Ω using a fixed value, and the shadow resonator energies ω_S. We see already that a strong photon loss error channel introduces a big performance hit in the ground state energy estimation, as good parameter choices indicated in these plots give slightly above 50% for 8 qubits, and down to about 35% for 14 and 16 qubits. for absolutely best parameter choices, we would expect the 18 qubit case to have the highest performance hit, but this parameter exploration provides a good quantitative and qualitative sense for the benefits of using the driven-dissipative error correction mechanism..... 87

Figure 5.4 Using a fixed $\omega_S = 3$, we do parameter scans for the primary-shadow coupling quadrature amplitudes Ω_0^x and Ω_0^y, exploring the overall amplitude (as opposed to more complex pulse-shaping). We see a general, though slight, advantage using the DRAG-like shapes for the coupling strength quadratures, particularly for the larger qubit systems. Note that the smaller number of qubit systems actually show a performance hit for the parameter space explored. 88

Figure 5.5 Looking at the performance of different system sizes using results from figures 5.3 and figure 5.4 for different photon loss rates. Here, it's hard to see much of a benefit, and in some particular cases the fixed coupling is better. Not that the fixed coupling results for 12 qubits are far from preferred parameters that would give better results, as is clear from figure 5.3. 89

Figure B.1 Simplified example of a surface code cycle projecting to the quiescent state and detecting physical qubit errors. (a) To keep this example manageable, only two data qubits and two stabilizer qubits are considered. (b) The cycle composed of pieces from figure 1.3(b) and (c), where the X-stabilizer cycle uses the stabilizer qubit as the control, and the Z-stabilizer cycle uses the Z-stabilizer as the target..... 113

Figure C.1 Fractional gates using the same set of parameters. $\{A, f, \alpha, c\} = \{82.645 \text{ MHz}, 1.868 \text{ GHz}, 1.333, 0.336\}$ to generate the waveforms at the top, giving the gate errors $\{1.21, 0.67, 0.30, 0.49, 0.29, 7.43, 102.99\} \times 10^{-6}$, shown in the bottom. 117

LIST OF TABLES

Table 2.1 Gradient ascent results for the lifetimes of logical X-eigenstates and Y-eigenstates—denoted T_X and T_Y, respectively, over the fixed parameter space of the VSLQ with $W = 2\pi \times 35$ MHz, and $\delta = 2\pi \times 350$ MHz. Note the lossy qubit energy approaches the energy from Eq. (2.9), $\omega_S = W + \delta/2 = 2\pi \times 210$ MHz. 42

Table C.1 Parameters for iSWAP waveform results in Fig. 3.2 and error rates in Fig. 3.3. 118

Table C.2 Parameters for XX waveform results in Fig. 3.2 and error rates in Fig. 3.3. Note the smaller full gate time compared to iSWAP gates. 119

Table C.3 Data for results plotted in Fig. 3.5, comparing the percent of the ground state energy that each type of gate set is able to produce. 120

ACKNOWLEDGMENTS

I would like to begin by thanking my parents—Fernando Rodríguez Casillas and Guadalupe Pérez Guillén, who are my first and most enduring teachers, and sacrificed so much so that my brothers and I are able to reach new heights.

I would also like to thank several members from our research group. Nick Materise for the many conversations that helped me achieve a much greater understanding of the physics in these projects. Zhijie Tang for helping develop the software used in these simulations. Eric Jones for helpful explanations that came particularly useful for the work on variational algorithms. Paul Varosy for being an incredibly helpful member for much of the work on RQE. And Eliot Kapit for being a great adviser and making all of this possible, thanks for taking a chance on me when I began this crazy journey.

Additional thanks to our experimental collaborators that are making a realization of this work a possibility. And special thanks to the National Science Foundation (NSF PHY-1653820) and the Army Research Office (ARO No. W911NF-18-1-0125) for funding all of this work, as well as the High Performance Computing teams at Tulane University (Cypress) and Colorado School of Mines (Wendian), where all of these simulations were run.

And finally, I would like to thank my wife Laura for all of the love and support she has given me all these years. Thank you for being an amazing partner, and allowing me to pursue my crazy ambitions at the cost of sacrificing some of your own. I will never be able to thank you enough.

Dedicated to Laura, Viggo, Giblet, and Baby.

CHAPTER 1

QUANTUM ERROR CORRECTION

Digital and Autonomous

I want to begin this discussion by briefly talking about quantum errors and quantum error correction (QEC), covering a well-known protocol - the Surface Code. A lot of content will be summarized from [5] and [6], which are very comprehensive reviews of engineered dissipation and Surface Codes, respectively. While the results presented in this thesis focus on error mitigation and applications of dissipative engineering for autonomous QEC (AQEC), a quick introduction to Surface Codes gives a motivation for exploring AQEC, as well as highlighting its benefits. But before even talking about why we even need QEC at all, it is useful to understand sources of error in superconducting architectures, and how they are modeled in simulations.

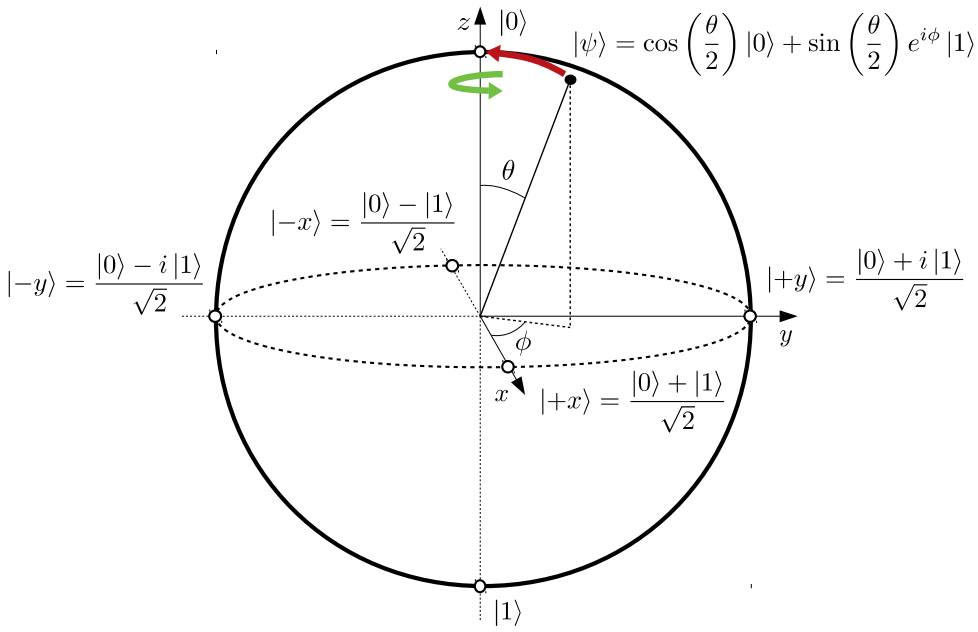

Figure 1.1: Bloch sphere representation of a qubit. The z basis is used as the computational basis by nomenclature, with x and y states represented in the z basis. Phase noise can be visualized as rotations around the axes by stray $\bar{\boldsymbol{\sigma}}$ operations (in green), and energy relaxation is visualized as the vector $|\psi\rangle$ relaxing towards the north pole $|0\rangle$ (in red).

The first section of this chapter introduces ways that noise can be modeled for open quantum systems, and the way in which the work in this thesis models noise for simulations. The next section then introduces codes for digital QEC, with a particular focus on the surface code. We limit the discussion in this chapter to some fundamental aspects that make the juxtaposition to AQEC methods in this work relevant. The last section in this chapter introduces AQEC and state stabilization using dissipative engineering. The discussion starts with cat codes—which are as of the time of this writing the only system to experimentally realize AQEC, and ends with the Very Small Logical Qubit (VSLQ) [7], a big focus of this thesis.

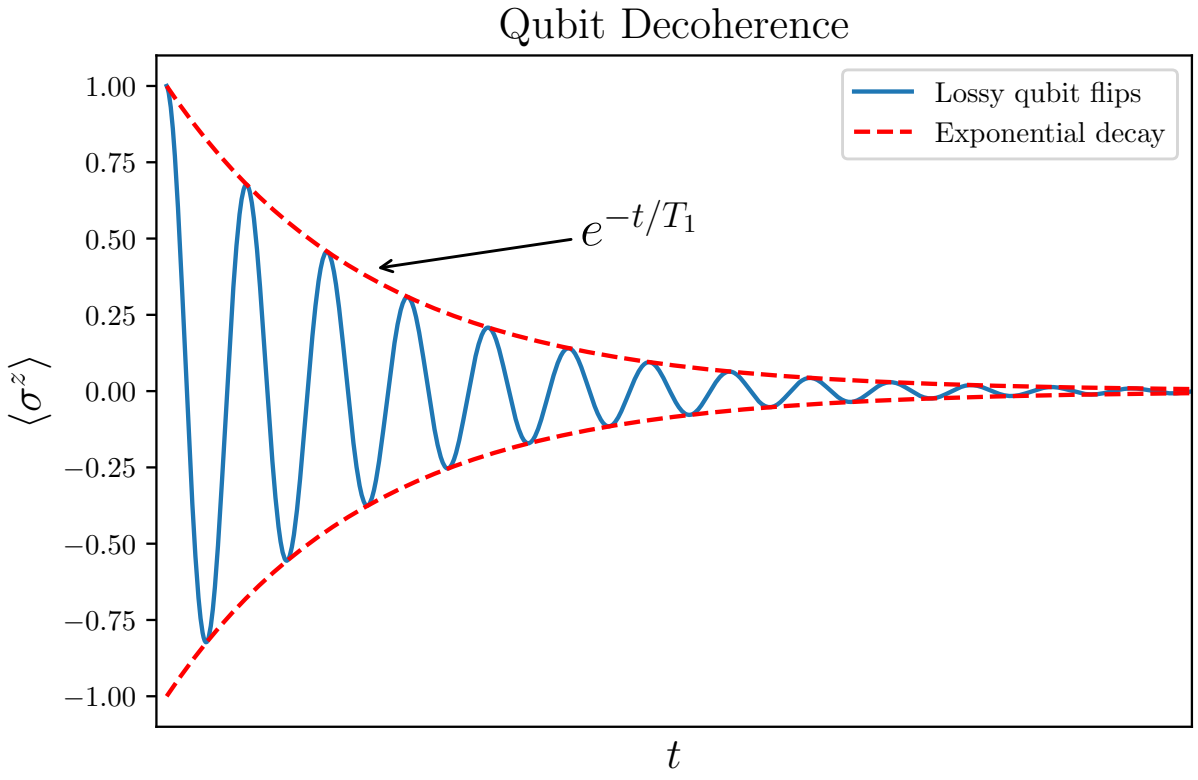

Figure 1.2: Time evolution of a qubit that is flipping along the z-axis between the ground state $|0\rangle$ and the first excited state $|1\rangle$ in the z-basis, in the presence of noise (interactions with the environment). This noise causes a loss in qubit coherence that is described by an exponential decay. From this exponential fit, the qubit lifetime T_1 is defined.

1.1 Modeling noise in qubits

A very thorough description of noise in superconducting qubits can be found in [8] and [5]. Here, I will focus on a description of noise used in our simulations. For a closed quantum system, the time evolution of a state $|\psi(t)\rangle$ is described by the Schrödinger equation

$$i\hbar\partial_t |\psi(t)\rangle = H |\psi(t)\rangle , \tag{1.1}$$

in which the action of the Hamiltonian H evolves the quantum state $|\psi(t)\rangle$. For a pure quantum state, we can describe the density matrix as $\rho(t) = |\psi(t)\rangle\langle\psi(t)|$. Furthermore, in the Bloch sphere picture for single qubit states, shown in figure 1.1, where

$$|\psi\rangle = \cos(\theta/2)\,|0\rangle + \sin(\theta/2)e^{i\phi}\,|1\rangle = \alpha\,|0\rangle + \beta\,|1\rangle , \tag{1.2}$$

with $\alpha, \beta \in \mathbb{C}$, we have

$$\rho = \begin{pmatrix} \cos^2\left(\frac{\theta}{2}\right) & e^{-i\phi}\cos\left(\frac{\theta}{2}\right)\sin\left(\frac{\theta}{2}\right) \\ e^{i\phi}\cos\left(\frac{\theta}{2}\right)\sin\left(\frac{\theta}{2}\right) & \sin^2\left(\frac{\theta}{2}\right) \end{pmatrix} = \begin{pmatrix} |\alpha|^2 & \alpha\beta^* \\ \alpha^*\beta & |\beta|^2 \end{pmatrix} . \tag{1.3}$$

The evolution for this qubit density matrix ρ as a closed quantum system can be described by the quantum Liouville equation

$$i\hbar\partial_t\rho = [H, \rho] , \tag{1.4}$$

replacing equation 1.1 in the density matrix picture. We are interested, however, in a description of noise, which manifests from spurious interactions with the environment. These interactions are characterized by a longitudinal and transverse relaxation rates Γ_1 and Γ_2, respectively. Γ_1 can be thought of as both excitations ($|0\rangle \to |1\rangle$) and relaxations ($|1\rangle \to |0\rangle$). However, assuming that a qubit is in a near-zero Kelvin operating regime such that $k_B T \ll \hbar\omega_q$, where $\hbar\omega_q$ is the qubit energy and k_B the Boltzmann constant, excitation rates are suppressed and Γ_1 can be visualized in figure 1.1 as a vector pointing south to $|1\rangle$, and relaxing towards the north pole to $|0\rangle$. The transverse relaxation rate, however, is defined as $\Gamma_2 = \Gamma_1/2 + \Gamma_\phi$, where Γ_ϕ is the dephasing rate. Γ_ϕ can be simply

illustrated as rotations about the z-axis in figure 1.1. Together, Γ_1 and Γ_ϕ characterize the decoherence rate of a qubit, Γ_2, and we can modify equation 1.3 for a description of noise [8],

$$\rho = \begin{pmatrix} 1 + \left(|\alpha|^2 - 1\right) e^{-\Gamma_1 t} & \alpha\beta^* e^{-\Gamma_2 t} \\ \alpha^*\beta e^{-\Gamma_2 t} & |\beta|^2 e^{-\Gamma_1 t} \end{pmatrix}. \tag{1.5}$$

Here, we can see that as $t \to \infty$, the qubit ends up completely in $|0\rangle$. The off-diagonal terms in this expression also have phase accrual terms $e^{i\Delta\omega t}$ to account for the difference in qubit frequency and rotating frame frequency, $\Delta\omega = \omega_q - \omega_{RF}$, which we simply choose to be zero here. We also note that by convention, we usually set $\hbar = 1$, and refer to ω_q as the qubit frequency and qubit energy interchangeably.

In this work, however, noise is simulated using the Lindblad picture, in which the time evolution of a quantum system ρ is described by the Lindblad master equation

$$\partial_t \rho = -\frac{i}{\hbar}\left[H, \rho\right] + \sum_n \Gamma_n \left(L_n \rho L_n^\dagger - \frac{1}{2}\left\{ L_n^\dagger L_n, \rho \right\} \right), \tag{1.6}$$

where ρ here can be an arbitrary quantum system and is not limited to qubits. Here, the L_n terms are collapse operators that characterize the noise channels for each part of the system, and Γ_n describes the noise rates—e.g. for a two-qubit system $|q_1 q_2\rangle$, L_1 and Γ_1 describe noise for the first qubit $|q_1\rangle$ and L_2 and Γ_2 describe noise for the second qubit $|q_2\rangle$. Equation 1.6 is a nonlinear, differential equation that can be easily solved numerically. The work presented in this thesis a Runge-Kutte 4th order method to numerically solve the master equation for different systems. This picture is quite general, and can be used to describe the evolution of qubits of different architectures. The only difference between different architectures in this picture will be the Hamiltonian used for the evolution, the collapse operators L_n and the loss rates Γ_n, the latter of which are a higher level characterization of lower level physical specifications. At this level of modeling, the key part is identifying the error channels that a particular architecture is susceptible to, so we can define the collapse operators. This work focuses on superconducting qubits, and more specifically assumes a transmon qubit [9] design—the most widely

adopted—though much of the work can be generalized to other superconducting qubit architectures.

Transmons are described the the Hamiltonian

$$H = 4E_C n^2 - E_J \cos\phi \tag{1.7}$$

where E_C is the total capacitance of the transmon's constituent capacitor and Josephson junction, E_J is the Josephson energy, n is the quantum charge operator and ϕ the phase operator, obeying the commutation relation

$$[\phi, n] = i, \quad n \to -i\frac{\partial}{\partial\phi}. \tag{1.8}$$

Making this substitution into equation 1.7, expanding the cosine term, and rewriting the n and ϕ operators in the quantum harmonic oscillator eigenbasis, we can rewrite equation 1.7 as

$$H = \omega_q a^\dagger a + \frac{\delta}{2} a^\dagger a^\dagger a a, \tag{1.9}$$

with $\delta = \omega_q^{0\to1} - \omega_q^{1\to2}$ being the nonlinearity, making the Hamiltonian resemble a Duffing oscillator [10]. This is a very useful representation of the qubit Hamiltonian since we can think of the quantum states of the transmon as the number of photons trapped in the antenna as $|0\rangle, |1\rangle, |2\rangle, ...$, making the ladder operator representation very intuitive. In this description, we refer to longitudinal noise as photon loss throughout this thesis. Furthermore, if excitations into higher states are suppressed, making a qubit where a single photon state intuitively maps to the qubit computational basis $\{|0\rangle, |1\rangle\}$ in figure 1.1, we can rewrite equation 1.9 as

$$H = \frac{\omega_q}{2}\sigma^z, \tag{1.10}$$

giving us a basic description of a transmon qubit.

We can consider an example in which a drive is applied to a qubit such that it undergoes continuous flipping between $|0\rangle$ and $|1\rangle$, described by the Hamiltonian $H = \frac{\omega_q}{2}\sigma^z + J\sigma^x$ applied to an initial state $|0\rangle$, where J determines the rate of oscillations.

Using equation 1.6, we describe the dynamics of this system with collapse operators $L \to \{a, a^\dagger\}$ and photon loss rate Γ, and produce the time evolution in figure 1.2. The photon loss rate determines the qubit lifetime $T_1 = 1/\Gamma$, which is generally on the order of tens of microseconds for superconducting qubits. Phase noise on the other hand is less pervasive at higher transition frequencies, while becoming prevalent at lower ones, dubbed so as $1/f$ noise. While the physics of this phenomenon is generally not well understood, a description of potential sources are more thoroughly explained in [11, 12]. Moreover, while there generally are other sources that can contribute to dephasing, $1/f$ noise is the most prominent in superconducting architectures. We can describe phase noise as Lindblad operators σ^z. Note that pure states in the z basis ($|0\rangle$ or $|1\rangle$) are insensitive to these spurious σ^z operations (although $\sigma^z |1\rangle \to -|1\rangle$, this does not affect the measurement outcome since a state vector pointing entirely along the z-axis won't see rotations about the z-axis). Likewise for x and y states for x and y errors, respectively.

The work presented in chapter 2 models noise in this manner, but it predominantly focuses on correcting photon losses and not phase errors, seeing as white noise photon losses are the limiting term in superconducting qubit coherence times $T_2 = 1/\Gamma_2$. The simulators for these projects were all developed in-house (appendix A), except for the RQE project in chapter 3. I now cover a very brief introduction to the ways in which errors are corrected in a surface code, though there are many similarities with other measurement-based QEC codes.

1.2 Digital quantum error correction

Most of the content I will be covering in this section will be a summary of the first sections in [6]. Generally speaking, the essence of QEC lies in encoding a logical qubit in the collective state of many physical qubits, using stabilizers to infer error patterns. This is an idea that has been well established in classical computing. The central mechanism by which these classical error correction codes work, as well as the quantum ones considered here, is redundancy. A very simple example to showcase this is the three-bit flip code

[13–15], which for classical error correction is a repetition code of length 3 [16]. For this classical correction code, information bits 1 and 0 are encoded using the corresponding three-bit sequences

$$\begin{aligned} 1 &\rightarrow 111 \\ 0 &\rightarrow 000, \end{aligned} \tag{1.11}$$

where the information bit is decoded as the majority vote of the three-bit sequences. As an example, the bit string 1001 would be encoded as 111 000 000 111. Assuming that the bit-flip error p is not too large, we can get, for example, 110 000 010 011, which using the majority vote rule gets decoded as the original bit string 1001. A logical error occurs when two or more bit flips occur for a three-bit sequence, where the probability that this happens is $p_{\text{flip}} = p^3 + 3p^3\,(1-p)$. And so, assuming that the bit-flip error $p < 1/2$, we are guaranteed that the information (logical) bits have a lower error rate than the individual component bits.

In practice, this is not an implemented EC code, but its simplicity provides a very useful explanation, and allows for an analogy to its quantum counterpart, the three-qubit flip code. This QEC code is described in more detail in section 2.3, in which we discuss for an application of dissipative engineering for autonomous QEC, serving as a segue to the very small logical qubit (VSLQ) [4] in section 2.4. Suffice to say here, that the main idea for the three-qubit flip code is exactly the same as that of its classical counterpart—the logical qubit equates to the majority vote of its substituent physical qubits. Just as in the classical case, the three-qubit flip code is more of a showcase for QEC, and not really a code that is seen as the way towards error-corrected fault-tolerant quantum computing. This requires more sophisticated codes, like the Bacon-Shor code [17], and the surface code [6]. While it remains an open question which qubit architecture will be the first to achieve fault-tolerance, and figuring out how to manage the massive data processing needed for large-scale quantum algorithms using logical qubits remains an unsolved challenge, the surface code is considered one of the most promising routes for superconducting qubits.

This leads us to a quick introduction on the fundamentals of the surface code.

1.2.1 Surface code

Of the different types of measurement-based error correction codes, we focus on the surface code (planar code) as it is the most realistic and "simple" of the approaches to fault-tolerance with superconducting qubits. This is largely due to the simplicity of a two-dimensional layout with nearest-neighbor coupling, as well as the very generous error rate threshold for fault-tolerance as high as ≈1%. The surface code is composed of a grid of qubits which are alternating data qubits and stabilizer qubits (also called "measure qubits" in [6]) as seen in figure 1.3(a). Each data qubit not along the boundary will couple to two X-stabilizer qubits and two Z-stabilizer qubits. This coupling helps identify whether a Z error or an X error has occurred when the stabilizer qubit is measured at the end of each cycle. The entangling operations in these cycles are such that, whatever the initial state of the data qubits, at the end of a measurement cycle, the data qubits will be in a state $\{|\Psi_{Z+}\rangle, |\Psi_{Z-}\rangle\}$ for a Z-stabilizer cycle or $\{|\Psi_{X+}\rangle, |\Psi_{X-}\rangle\}$ for an X-stabilizer cycle. This set of states form what is called the "quiescent" state, which is the resulting state over the entire grid after every group of data and stabilizer qubits go through the cycles in figure 1.3(b) and figure 1.3(c). This quiescent state remains unchanged after every cycle, which are done over the entire grid in lock-step. Note that the data qubits are never measured, so this quiescent state is never collapsed. Only the stabilizer qubits are measured at the end of every cycle, which let us know when there is a change in the quiescent state by a sign flip in the measurement. We illustrate a simplified example of this mechanism in appendix B. To think of this in simple terms, recognize that each data qubit has two degrees of freedom, while each stabilizer qubit presents two constraints. Thus, for n qubits we have $2n$ degrees of freedom, and for $(n-1)$ stabilizer qubits we have $2(n-1)$ constraints, leaving us with 2 overall degrees of freedom, which we use to define a logical qubit.

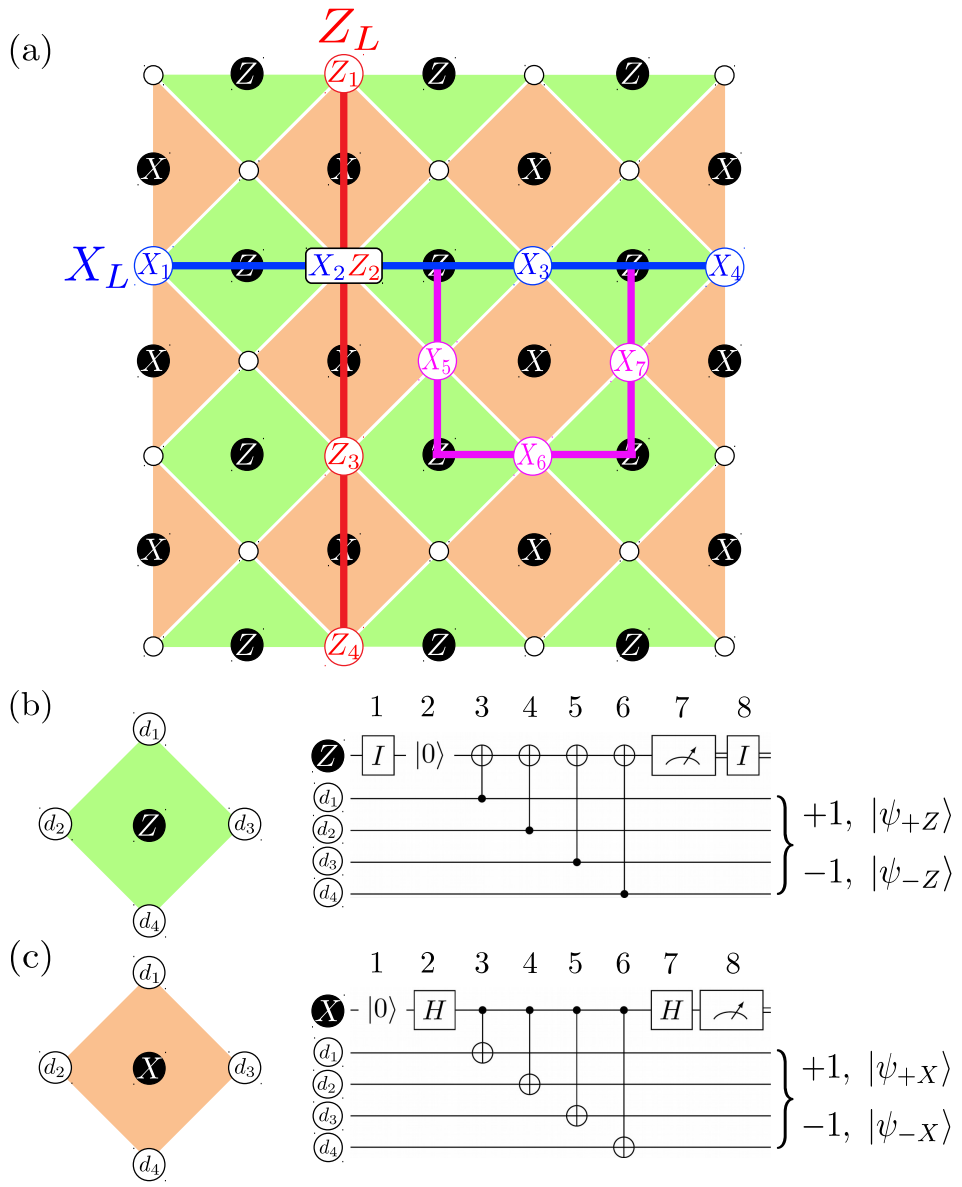

Figure 1.3: The surface code consists of n data qubits and $(n-1)$ stabilizer qubits (white and black dots, respectively). (a) Each data qubit is coupled to four stabilizer qubits, and each stabilizer qubit is coupled to four data qubits, except at the boundary where data qubits are coupled to two or three stabilizer qubits and stabilizer qubits are coupled to three data qubits (you cannot have a stabilizer qubit coupled to two data qubits). Operations on the logical qubit are done by chains of operations connecting the boundaries (X_L in blue and magenta, Z_L in red). Both (b) and (c) show error-detection cycles for X- and Z-error syndromes, in which the data and stabilizer qubits go through a series of CNOT entangling gates. (b) One Z-stabilizer qubit is the target qubit for CNOTs with data qubits d_1, d_2, d_3, and d_4, whereas (c) an X-measure qubit is the control qubit for CNOTs with data qubits d_1, d_2, d_3, d_4.

The type of stabilizer qubit that signals a sign flip lets us know what kind of error has occurred for one of the four neighboring data qubits. For an X or a Z error in a data qubit, the two X- or Z-stabilizer qubits would signify this with a sign flip in their measurement. As errors occur, the signs from the measurements of the stabilizer qubits change according to their corresponding error, Z-stabilizer qubits flip for X errors, and vice versa—recall from section 1.1 that a z state along the Bloch sphere is insensitive to Z errors, and likewise for x states and X errors. Only a z state will be able to see an X error, and vice versa, as is evident by performing these operations on Z-basis states,

$$\begin{aligned} Z|0\rangle &= \begin{pmatrix} 1 & 0 \\ 0 & -1 \end{pmatrix} \begin{pmatrix} 1 \\ 0 \end{pmatrix} = \begin{pmatrix} 1 \\ 0 \end{pmatrix} = |0\rangle\,, \; Z|1\rangle = \begin{pmatrix} 1 & 0 \\ 0 & -1 \end{pmatrix} \begin{pmatrix} 0 \\ 1 \end{pmatrix} = \begin{pmatrix} 0 \\ -1 \end{pmatrix} = -|1\rangle \\ X|0\rangle &= \begin{pmatrix} 0 & 1 \\ 1 & 0 \end{pmatrix} \begin{pmatrix} 1 \\ 0 \end{pmatrix} = \begin{pmatrix} 0 \\ 1 \end{pmatrix} = |1\rangle\,, \; X|1\rangle = \begin{pmatrix} 0 & 1 \\ 1 & 0 \end{pmatrix} \begin{pmatrix} 0 \\ 1 \end{pmatrix} = \begin{pmatrix} 1 \\ 0 \end{pmatrix} = |0\rangle \end{aligned} \tag{1.12}$$

and X-basis states,

$$\begin{aligned} Z|+x\rangle &= \begin{pmatrix} 1 & 0 \\ 0 & -1 \end{pmatrix} \frac{1}{\sqrt{2}} \begin{pmatrix} 1 \\ 1 \end{pmatrix} = \frac{1}{\sqrt{2}} \begin{pmatrix} 1 \\ -1 \end{pmatrix} = |-x\rangle \\ Z|-x\rangle &= \begin{pmatrix} 1 & 0 \\ 0 & -1 \end{pmatrix} \frac{1}{\sqrt{2}} \begin{pmatrix} 1 \\ -1 \end{pmatrix} = \frac{1}{\sqrt{2}} \begin{pmatrix} 1 \\ 1 \end{pmatrix} = |+x\rangle \\ X|+x\rangle &= \begin{pmatrix} 0 & 1 \\ 1 & 0 \end{pmatrix} \frac{1}{\sqrt{2}} \begin{pmatrix} 1 \\ 1 \end{pmatrix} = \frac{1}{\sqrt{2}} \begin{pmatrix} 1 \\ 1 \end{pmatrix} = |+x\rangle \\ X|-x\rangle &= \begin{pmatrix} 0 & 1 \\ 1 & 0 \end{pmatrix} \frac{1}{\sqrt{2}} \begin{pmatrix} 1 \\ -1 \end{pmatrix} = \frac{1}{\sqrt{2}} \begin{pmatrix} 1 \\ -1 \end{pmatrix} = |-x\rangle\,. \end{aligned} \tag{1.13}$$

Having detected errors that have occurred, the error types have to be identified and then corrected, but this is a process that is completely done classically. It is perfectly acceptable to perform a correcting quantum operation on the data qubit to negate the error. However, additional quantum operations introduce additional sources of error—even the cyclic measurements for the stabilizer qubits can introduce errors! These measurement

errors typically vanish by subsequent cycles, and are detected by consecutive sign changes on a single stabilizer qubit, as opposed to data qubit errors which will flip the signs of two or more stabilizer qubits in its vicinity. This means that multiple surface code cycles are required to establish a measurement value. Thus, in an effort to reduce the possible channels for error, instead of directly correcting data qubit errors that are detected, it is much easier to keep a record of them and account for them in classical software processing.

Operations on the logical manifold are operations that can manipulate the two degrees of freedom that make up the quiescent state. By applying an X operator to two data qubits adjacent to a stabilizer qubit, the resulting operation will commute with the corresponding Z- or X-stabilizer. By applying X operators to subsequent data qubits as in the blue line in figure 1.3(a), the resulting chain operation will commute with all stabilizer qubits in the connecting chain between the boundaries. The resulting state will be a quiescent state $|\psi_X\rangle$ that differs from the original quiescent state $|\psi\rangle$ by $|\psi_X\rangle = X_L |\psi\rangle = X_1X_2X_3X_4 |\psi\rangle$ (following the blue line in figure 1.3(a)). Likewise, we can do $Z_L |\psi\rangle = Z_1Z_2Z_3Z_4 |\psi\rangle$ (red line). The new quiescent state $|\psi_X\rangle$ remains unchanged through the surface code cycles with the same measurement outcomes as $|\psi\rangle$ (see appendix B). Note however, that $|\psi_X\rangle \neq |\psi\rangle$, since data qubits were flipped by X operations. Therefore, the resulting quiescent state $|\psi_X\rangle = X_L |\psi\rangle$ is distinct from the original quiescent state $|\psi\rangle$, and the operator X_L manipulates the two degrees of freedom for this logical manifold. The same can be easily abstracted for Z_L operations. Note that "non-straight" series of operations (magenta line $X_1X_2X_5X_6X_7X_4 |\psi\rangle$ in figure 1.3(a)) also commute with the syndrome qubits and do not change the measurement outcome—as long as the chain of operations connect the boundaries, the resulting operation successfully manipulates the quiescent state degrees of freedom. Further degrees of freedom can be created by simply removing stabilizer qubits, with logical operators to manipulate those additional degrees of freedom defined by chains of single qubit operations between and around the newly formed boundaries.

A full and thorough understanding of surface codes requires a much greater depth of literature. This manuscript only focuses on introducing the above to illustrate the most basic idea comprising the surface code: defining a logical state in the collective state of many physical qubits, and the corresponding way in which those logical states are operated on. This will serve as a relevant comparison to the very small logical qubit in section 2.4. Lastly, it is important to mention that the surface code cycle summarized in this manuscript addresses single qubit errors. However, there are several other error syndromes that the surface code is not designed to address (such as leakage), and many other challenges towards experimentally realizing a surface code. Notably, the surface code itself is not capable of universal quantum computation, and additional ancilla state distillation is needed, which can increase the number of physical qubits needed by a factor of ten. Furthermore, two-qubit gate errors remain significantly higher than single-qubit gate errors for superconducting architectures, presenting a challenge for the repeated surface code cycles consisting of multiple two-qubit CNOT gates. Thus, even though surface codes are highly touted as a promising pathway toward fault-tolerance, it's worth noting that there is a lot of progress yet to be made for a fault-tolerant logical qubit, much less a quantum computer consisting of many logical qubits.

1.3 Autonomous quantum error correction

Chapter 2 covers some very good examples utilizing autonomous QEC on three separate systems of increasing complexity. More thorough discussions on some of those examples are saved for that chapter, though the Very Small Logical Qubit (VSLQ) [4] is introduced here more in-depth. Although engineered dissipation can be used for a plethora of applications, the focus of this chapter is on engineered dissipation for state stabilization, with the ultimate goal of autonomous QEC (AQEC). A thorough review of using dissipation as a source for quantum information, including our focus on AQEC, is provided in [5].

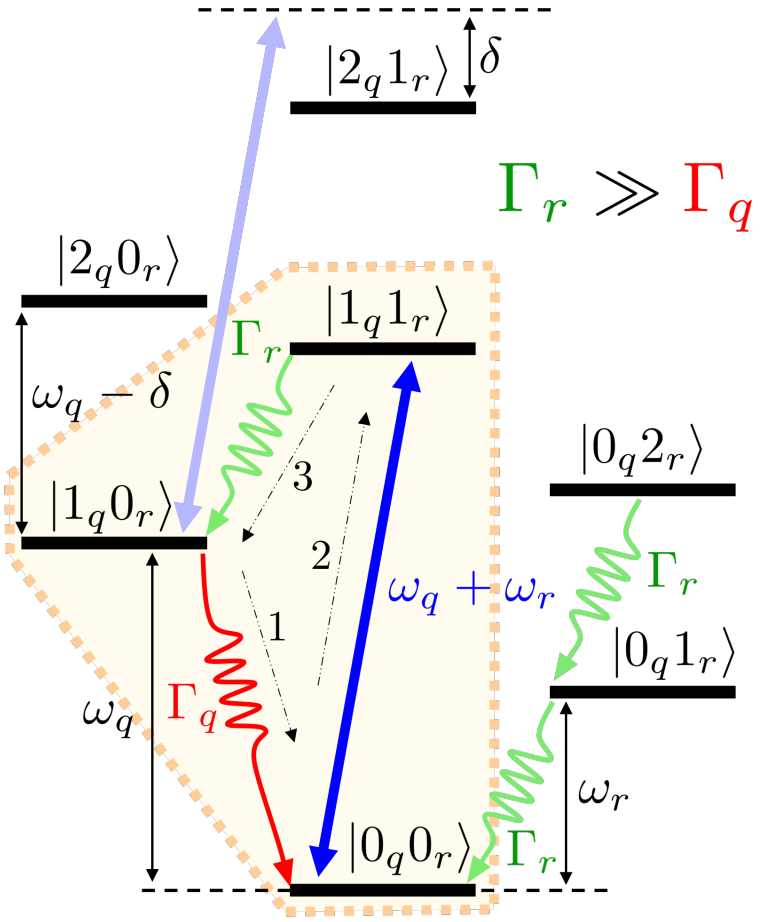

Figure 1.4: A simplified example of a high-coherence qubit device (loss rate Γ_q) and a lossy linear resonator (Γ_r), demonstrating the always-on, off-resonant drive mechanism that autonomously increases the occupation probability of the first-excited state of the qubit device. By driving the transition $|0_q 0_r\rangle \rightarrow |1_q 1_r\rangle$ (blue line), the nonlinearity δ ensures that it is off-resonant with $|1_q 0_r\rangle \rightarrow |2_q 1_r\rangle$ (opaque blue), leaving the target state $|1_q 0_r\rangle$ unchanged. The procedure follows the steps in the opaque orange region—1. The qubit device experiences a photon loss at a rate Γ_q (red), which is ideally low relative to Γ_r. 2. The always-on drive is resonant with $|0_q 0_r\rangle \rightarrow |1_q 1_r\rangle$, and induces transitions between the two states. 3. The lossy resonator undergoes photon losses at a fast rate Γ_r (green, $\Gamma_r \gg \Gamma_q$), inducing $|1_q 1_r\rangle \rightarrow |1_q 0_r\rangle$ with high likelihood. This returns the system to the original state. Spurious occupations of higher-energy states in the resonator can safely be ignored due to the high decay rate. And finally, note that this mechanism can be applied to "correct" transitions into other unwanted states—for example, constantly driving a photon exchange resonant with the transition $|2_q 0_r\rangle \rightarrow |1_q 1_r\rangle$ would correct leakage.

This section introduces the idea of AQEC (also called passive QEC in some literature) using cat codes and the VSLQ, as well as some of the advantages that it provides over the measurement-based surface code introduced above. The hallmark feature that distinguishes AQEC from digital codes is the absence of any sort of measurement in the process of correcting an error. As explained in section 1.2.1, correcting an error is a multi-step process, where after stabilizer operations have determined if an error has occurred, the error then needs to be identified and digitally corrected post-processing, a process that very quickly becomes very complex with a large number of physical qubits. Indeed, implementing the surface code at the scale necessary to perform certain quantum algorithms (i.e. Shor's algorithm) would require massive amounts of classical computing resources. As the name implies, AQEC corrects errors autonomously without the need to detect them and post-process the correction.

We first consider the case of simple state stabilization of a single qubit device—here we consider a transmon energy level structure, but this can be generalized to other devices. This is done by selective coupling to an engineered bath, where the coupling between the target system to be protected and an engineered bath is continuously driven off-resonantly so as to not disturb the computational states, as shown in figure 1.4, where we consider a high-coherence transmon coupled to a lossy resonator with the goal of protecting the first excited state in the transmon. Here, there is a continuous drive for the operation $\Omega(a_q^\dagger a_r^\dagger + a_q a_r)$, which is off-resonant when in the target state $|1_q 0_r\rangle$ due to the transmon nonlinearity. This drive, however, is in resonance with a transition from an error state to an intermediate state that then decays into the target state using the lossy bath. In the case of figure 1.4, this is the $|0_q 0_r\rangle \rightarrow |1_q 1_r\rangle$ transition. Thus at the occurrence of a photon loss in the transmon, the continuous drive resonantly couples with the engineered bath, while doing nothing in the absence of an error. Note that when the constant coupling is in resonance with the desired transition—error state to intermediate state, it will drive Rabi flopping between the two states. However, due to the lossiness of the coupled bath, the intermediate state quickly decays into the target state ($|1_q 1_r\rangle \rightarrow |1_q 0_r\rangle$ in figure 1.4) with

high likelihood. Thus, the average occupation probability of the system favors the target state. At no point throughout this process is the state measured or is a determination made on whether the system-bath coupling needs to be turned on to induce any transition. The system is simply driven continuously with carefully tailored flux drives in favor of desired transitions with the aid of a dissipative bath, making this process completely autonomous.

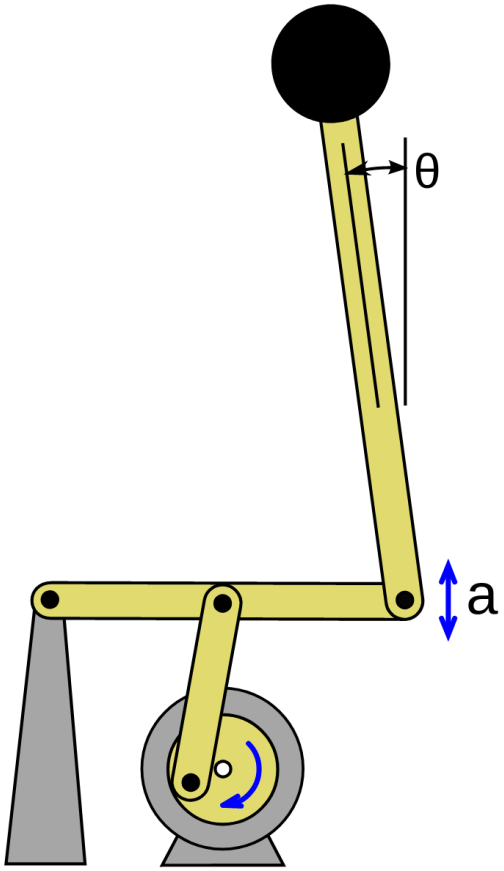

Figure 1.5: As a classical analogy, quantum state stabilization by a continuous drive with a non-Markovian reservoir [1] is much like Kapitza's pendulum. Here, we take a rigid pendulum, which has two equilibrium states—a stable equilibrium point when pointing straight down, and an unstable equilibrium point when pointing straight up. By driving fast, constant oscillations so that the pendulum bounces up and down, the straight up, unstable equilibrium point is stabilized.

This continuous drive targeting certain transitions for state stabilization is very similar to Kapitza's pendulum from classical mechanics [18]. shown in figure 1.5. This is a rigid inverted pendulum—a typical rigid pendulum's unstable equilibrium state. For a regular

rigid pendulum, small perturbations will bring the system from the upright, unstable equilibrium state to it's stable equilibrium (pointing straight down). By adding a driving force, in this case a rapidly rotating crank vibrating the rigid pendulum up and down, deviations from the unstable equilibrium can be corrected and the upright position maintained as a steady state. This is a very abstract and simplified explanation using engineered driven dissipation for state stabilization, as well as a very loose analogy to the classical Kapitza's pendulum. This chapter only attempts to introduce these ideas, barely scratching the surface of more in-depth applications. The examples in chapter 2 provide a glimpse into more complex and interesting applications using driven dissipation beyond the example in figure 1.4, where the extension to error correction from simple state stabilization is very natural. [5] lays out a set of conditions for which AQEC for a primary system coupled to an engineered dissipative bath can be achieved:

- Rotating frame ground states for the primary system must form a logical manifold
- Dissipation-induced correction rate is much faster than the primary loss rate
- The steady state of the system is given by an incoherent mixture of states in the logical manifold
- The process of a photon loss and its correction produces no relative phase or energy differences between states in the logical manifold.

Note that these conditions mention photon losses, while not addressing dephasing at all. Indeed, the main purpose of AQEC using engineered dissipation is to correct the photon loss error channel. However, it also suppresses phase noise, something that is not at all obvious. To offer a simple explanation, achieving QEC requires an engineered primary system Hamiltonian with two degenerate ground states in the rotating frame that can be used to define logical states. These ground states are separated from higher excited states by some finite energy Δ, where the only way for these two ground states to mix is through interactions with the higher energy states at an energy cost $\geq \Delta$. Thus, the total process of a photon loss error, and its subsequent correction happens in an energetically favorable process such that there is no arbitrary phase introduced between the two ground

states, due to the nature of phase noise being dominated at the low-frequency range and is weak at this transition frequency. As such, while the goal of AQEC using dissipative engineering laid out in this manuscript is to correct photon losses, dephasing is suppressed as well. A caveat of AQEC methods is that these likely will not be able to correct arbitrarily large sequences of errors, but rather provide a possible benefit for near-term applications as well as improving the error threshold for fault-tolerant codes. I now briefly introduce cat codes and the VSLQ, the former of which is the first demonstration of error correction for any qubit architecture, and the latter—influenced by cat codes—of which is a bigger focus in this thesis.

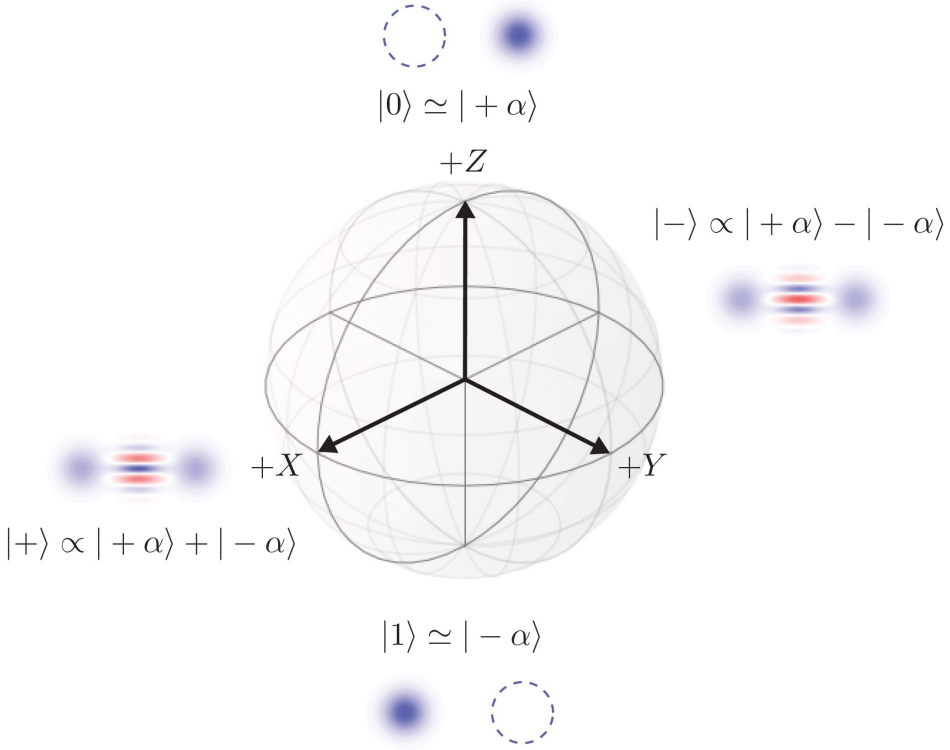

Figure 1.6: Bloch sphere representation of cat code logical states, reproduced with permission from [2]. The states $|\pm\alpha\rangle$ are represented as Wigner functions for $\alpha = 2$. The logical space is defined as $\{|0_L\rangle, |1_L\rangle\} \rightarrow \{|+\rangle, |-\rangle\}$.

1.3.1 Cat codes

Cat codes themselves are an incredibly big and complex field of research, and it would be a big deviation from the content of this manuscript to delve too deep into the subject.

A very thorough review of using cat codes to implement fault-tolerant quantum computers is given by [2]. This section is just a quick introduction to the concepts underpinning AQEC in cat codes. An example of codewords for cat codes are illustrated in figure 1.6, where the z-basis states $\{|0\rangle, |1\rangle\}$ are encoded using the quasi-orthogonal bosonic cavity states $\{|+\alpha\rangle, |-\alpha\rangle\}$. These states $|\alpha\rangle$ are coherent states for a single bosonic degree of freedom, with $\alpha \in \mathbb{C}$. These are implemented using a high-coherence resonator and a lossy resonator, with a transmon to manipulate the bosonic states of the coherent resonator. The coherent states can be used to futher define orthogonal states using superpositions of these coherent states to define

$$|\pm\rangle = \frac{|\alpha\rangle \pm |-\alpha\rangle}{\sqrt{2(1 \pm e^{-2|\alpha|^2})}}, \tag{1.14}$$

which correspond to the x-basis states in the Bloch sphere picture. These are the ones to define the logical qubits $\{|0_L\rangle, |1_L\rangle\} \to \{|+\rangle, |-\rangle\}$, also called odd- and even-parity cat states as they are eigenstates of the parity operator $P = e^{i\pi a^\dagger a}$. Considering energy relaxation and dephasing error channels, the system dynamics are described by the master equation

$$\partial_t \rho = \sum_{i=1}^{3} \Gamma_i \left(L_i \rho L_i - \frac{1}{2}\{L_i^\dagger L_i, \rho\} \right), \tag{1.15}$$

where $\Gamma_{1,2}$ are the usual photon loss and dephasing rates $\Gamma_{1,\phi}$, and Γ_3 is a two-photon loss rate. These correspond ot the Lindblad operators $L_1 = a$, $L_2 = a^\dagger a$, and $L_3 = a^2 - \alpha^2$. Remarkably, the two-photon loss operator stabilizes the $|\pm\alpha\rangle$ states, as it is straightforward to see by considering states for which $a^2 |\psi\rangle = \alpha^2 |\psi\rangle$ when $\Gamma_{1,\phi} = 0$. With these considerations, any arbitrary states exponentially decay into the codespace $|\pm\alpha\rangle$ at some confinement rate Γ_{conf}. For finite $\Gamma_{1,\phi}$, this is no longer the case, but as long as the confinement rate is greater than the error rate, $\Gamma_{\text{conf}} > \Gamma_{\text{err}}$, the states are still metastable, providing a rudimentary example of AQEC. However, using the codespace $|\pm\alpha\rangle$ is not able to address all error channels. A more complex scheme is required to do this, examples of which can be found in [2] and [5]. This introduction to cat codes only serves as a segue to

the more relevant subject in this thesis—the VSLQ, which as mentioned above, is directly influenced by cat codes.

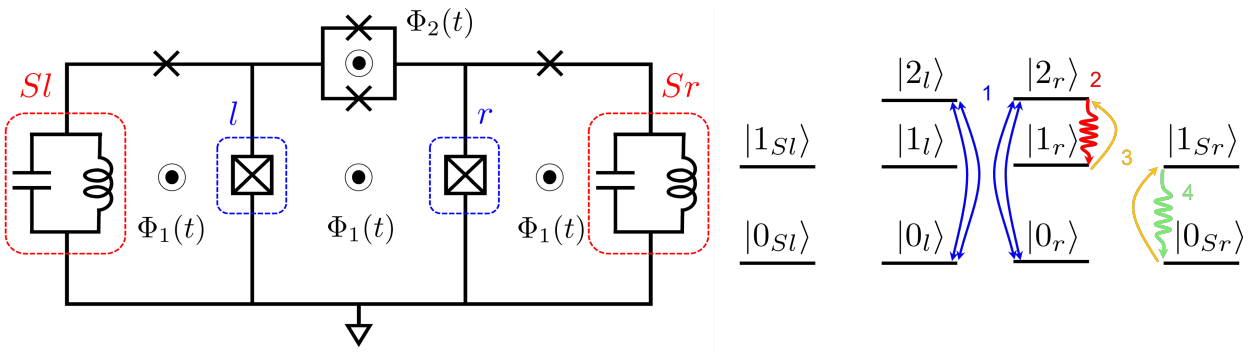

Figure 1.7: Circuit diagram for an implementation of the VSLQ, which consists of two high-coherence transmons (labeled l and r in blue) and two lossy resonators (Sl and Sr in red). The coupling mechanism between the transmons is a four-photon exchange, and a two-photon pump for the transmon-resonator coupling. The error correction steps are illustrated on the right: 1. (Blue) The state is initially stabilized in the logical manifold with the continuous 4-photon exchange term $\tilde{X}_l\tilde{X}_r$, $\tilde{X} \rightarrow a^\dagger a^\dagger + aa$. 2. (Red) Photon loss experienced from the right transmon at a rate $2\Gamma_P$, which is ideally low. 3. (Orange) Transmon-resonator drive $\Omega(a_r^\dagger a_{Sr}^\dagger + a_r a_{Sr})$ exites for the transmon and resonator. Like in figure 1.4, this operation is off-resonant except in the event of a photon loss in the primary transmon. 4. (Green) Photon loss in the resonator at rate Γ_S, which is ideally high. With high likelihood, the resonator decays back to its ground state before the driven transmon-resonator coupling returns to the error state.

1.3.2 Very Small Logical Qubit

I provide a brief introduction for the VSLQ, though a bit more in depth than that for cat codes. An illustration of the EC mechanisms for the device is shown in figure 1.7. As shown, the VSLQ is composed of two high-coherence qubit devices, and two lossy qubits or resonators. The example figure uses two transmons for the high-coherence devices (in blue boxes), and two resonators for the lossy devices (in red boxes). Assuming the Josephson energies E_J are equal, the transmon qubits coupling Hamiltonian is

$$H = -E_J \left[\cos(\phi + \Phi_1(t)) + \cos(\phi + \Phi_1(t) + \Phi_2(t))\right], \tag{1.16}$$

where $\Phi_1(t)$ is the flux drive through the inner loops, and $\Phi_2(t)$ is the flux drive in the SQUID (superconducting quantum interference device) loop, shown in figure 1.7. By choosing $\Phi_1(t) = -\pi/2 + f(t)$ and $\Phi_2(t) = \pi - 2f(t)$, where $f(t)$ is a rapidly oscillating signal, this Hamiltonian simplifies to

$$H = -2E_J \cos\phi \sin f(t). \tag{1.17}$$

Here, $f(t)$ is chosen so that, combined with the expansion of the phase operators $\cos\phi$ and $\sin\phi$, we get the desired four-photon exchange terms. $f(t)$ is thus chosen so that any undesired signals are fast-oscillating and can be dropped in the rotating frame after the rotating wave transformation

$$|\psi\rangle \rightarrow e^{i[(\omega_l - \delta/2)n_l + (\omega_r - \delta/2)n_r]t} |\psi\rangle \tag{1.18}$$

where $\omega_{l,r}$ are the transmon frequencies separated by about a GHz, and $n_i = a_i^\dagger a_i$ are the number operators. Defining $\tilde{X}_i = 1/2\left(a_i^\dagger a_i^\dagger + a_i a_i\right)$, we can write the effective rotating frame Hamiltonian

$$H_P = -W\tilde{X}_l\tilde{X}_r + \frac{\delta}{2}\left(P_l^1 + P_r^1\right), \tag{1.19}$$

with $P_i^1 = |1_i\rangle\langle 1_i|$ being the projection operator onto the transmon 1 states and δ the nonlinearity. Extending equation 1.16 to the transmon-resonator couplings, with the flux drives through the corresponding loops $\Phi_S(t) = -\pi/2 + g(t)$, we can choose $g(t) \propto \cos\left[(\omega + \omega_S - W - \delta)t\right]$, allowing a similar rotating wave transformation to equation 1.18 to get the rotating frame Hamiltonian

$$H_S + H_{PS} = \left(W + \frac{\delta}{2}\right)(n_{Sr} + n_{Sl}) + \Omega\left(a_r^\dagger a_{Sr}^\dagger + a_l^\dagger a_{Sl}^\dagger + a_r a_{Sr} + a_l a_{Sl}\right), \tag{1.20}$$

giving us the full system Hamiltonian $H = H_P + H_S + H_{PS}$, where H_P denotes the "primary qubits" (transmons), H_S denotes the "shadow qubits" (resonators), and H_{PS} is the interaction term. The terminology "primary" and "shadow" are from the original proposal of the device [4], and are used here for consistency.

Diagonalizing the primary qubit Hamiltonian is trivial looking at the matrix representation for the $\tilde{X}$ operators

$$\tilde{X} = \frac{1}{2}\begin{pmatrix} 0 & 0 & 1 \\ 0 & 0 & 0 \\ 1 & 0 & 0 \end{pmatrix} \tag{1.21}$$

where it is clear that the ket states $(|2\rangle \pm |0\rangle)/\sqrt{2}$ are eigenstates with eigenvalues $\pm 1/2$. Extending this two the two-qubit primary system, we can see that that states $(|2_l\rangle \pm |0_l\rangle)/\sqrt{2} \otimes (|2_l\rangle \pm |0_l\rangle)/\sqrt{2}$ are degenerate, and are used to define the codewords for the logical states:

$$\begin{aligned} |0_L\rangle &= \frac{1}{\sqrt{2}}(|2_l\rangle + |0_l\rangle) \otimes \frac{1}{\sqrt{2}}(|2_r\rangle + |0_r\rangle) \otimes |0_{Sl}0_{Sr}\rangle \\ |1_L\rangle &= \frac{1}{\sqrt{2}}(|2_l\rangle - |0_l\rangle) \otimes \frac{1}{\sqrt{2}}(|2_r\rangle - |0_r\rangle) \otimes |0_{Sl}0_{Sr}\rangle\,, \end{aligned} \tag{1.22}$$

where we also use the simple fact that the resonator ground states are $|0_{Sl}0_{Sr}\rangle$. Logical operators on these states are defined as $X_L = \tilde{X}_l$ or $\tilde{X}_r$, $Z_L = \tilde{Z}_l\tilde{Z}_r$, where $\tilde{Z} = |2\rangle\langle 2| - |0\rangle\langle 0|$, and $Y_L = X_L Z_L$. Using these definitions, the states in equation 1.22 are eigenstates of the X_L operator, and are referred to as such in section 2.4.2, where we also explore eigenstates of the Y_L operator.

To see how the primary-shadow coupling autonomously corrects errors, consider the illustration shown in figure 1.7. Initially, the system is in one of the logical states in equation 1.22, and the operations in the primary Hamiltonian $\tilde{X}_l\tilde{X}_r$ maintain the system there. But consider a photon loss in the right qubit, sending the system to the error state

$$|\mathrm{Err}_r\rangle = \frac{1}{\sqrt{2}}(|2_l\rangle \pm |0_l\rangle) \otimes |1_r\rangle \otimes |0_{Sl}0_{Sr}\rangle\,. \tag{1.23}$$

This state is now in resonance with the operation $\Omega a_r^\dagger a_{Sr}^\dagger$ and refills the lost photon in the primary qubit, as well as adds one to the resonator, going to the state

$$|\mathrm{Err}_r'\rangle = \frac{1}{\sqrt{2}}(|2_l\rangle \pm |0_l\rangle) \otimes |2_r\rangle \otimes |0_{Sl}1_{Sr}\rangle\,. \tag{1.24}$$

The primary qubit state is now back in resonance with the primary qubits operation $-W\tilde{X}_l\tilde{X}_r$, bringing the primary qubit r back to the superposition state it started in. Due to the lossiness of the resonator, it will decay back to its ground state with high probability, and thus the system has been autonomously corrected back to its ground state with high probability. Note that there is nothing in $\tilde{X}$ explicitly determining whether a state $|2\rangle$ should go to $|0\rangle + |2\rangle$ or $|2\rangle - |0\rangle$. Moreover, because the states in equation 1.22 are degenerate, we might naively assume that the correction mechanism would choose either state with equal probability. However, note that primary qubits states with opposite sign would return a $+W$ from the primary qubits Hamiltonian, which is far from the ground state. So in the correction example above, the state

$$|\mathrm{Err}_r''\rangle = \frac{1}{\sqrt{2}}\left(|2_l\rangle \pm |0_l\rangle\right) \otimes \left(|2_r\rangle \mp |0_r\rangle\right) \otimes |0_{Sl}1_{Sr}\rangle \tag{1.25}$$

is not energetically preferred, and is thus suppressed. Therefore, while the mechanism does not explicitly correct dephasing, of which equation 1.25 is an example, it is energetically suppressed.

While it is clear that the intrinsic autonomy of a system that is passively protected against errors is advantageous over a digitally corrected system by reducing the overhead complexity involved in the detection and active correction of errors, as is seen in sections 2.3 and 2.4, these methods also have the advantage that they have a significantly smaller footprint than the very promising surface code—the VSLQ consists of only four qubits to define a logical manifold, while the smallest number of qubits required for a surface code is seventeen. Nevertheless, meeting the requirements above in an experimental setup can be a challenge. Indeed, given the relative novelty of using dissipation for QEC, there is a lot of work to be done on the experimental front for realizing such a setup.

The work in chapter 2 focuses on techniques for addressing some challenges with using a dissipative bath to stabilize a primary system. Namely, it explores how we can minimize the intrinsic error induced by using dissipation itself as an error correction mechanism.

Understanding the shortcomings of AQEC is very important in making the method more attractive to experimental realizations. Given that well-established digital codes are highly prized for their high error-threshold and are generally regarded as a path towards fault-tolerant quantum computing, one of the goals of this thesis to try to explore ways in which driven dissipative techniques can be improved in highly coherent logical manifolds in AQEC circuits, as well as techniques to minimize intrinsic error incurred by the correction mechanism itself. Chapter 3 looks at such a problem, where we expand a more in-depth description of behavior similar to that observed in section 2.2.2, in which using a counter-oscillating waveform minimizes leakage for a two-qubit operation. Chapter 4 looks at work in progress for experimental realizations of the VSLQ, and chapter 5 introduces work in progress for implementations of driven dissipative engineering for NISQ (noisy intermediate-scale quantum) algorithms.

CHAPTER 2

IMPROVED AUTONOMOUS ERROR CORRECTION USING VARIABLE DISSIPATION IN SMALL LOGICAL QUBIT ARCHITECTURES

Reproduced with permission from [19]. Quantum Science and Technology

 David Rodríguez Pérez [*] [12], Eliot Kapit[1,2]

DOI: 10.1088/2058-9565/abc3cb

Abstract

Coherence times for superconducting qubits have greatly improved over time. Moreover, small logical qubit architectures using engineered dissipation have shown great promise for further improvements in the coherence of a logical qubit manifold comprised of few physical qubits. Nevertheless, optimal working parameters for small logical qubits are generally not well understood. This work presents several approaches to finding preferential parameter configurations by looking at three different cases of increasing complexity. We begin by looking at state stabilization of a single qubit using dissipation via coupling to a lossy object. We look at the limiting factors in this approach to error correction, and how we address those by numerically optimizing the parametric coupling strength with the lossy object having an effective time-varying dissipation rate—we call this a pulse-reset cycle. We then translate this approach to more efficient state stabilization to an abstracted three-qubit flip code, and end by looking at the Very Small Logical Qubit (VSLQ). By using these techniques, we can further increase logical state lifetimes for different architectures. We show significant advantages in using a pulse-reset cycle over numerically optimized, fixed parameter spaces.

---

[*]Primary and corresponding author, drodriguezperez@mines.edu.

[1]Department of Physics, Colorado School of Mines, Golden, Colorado 80401, USA.

[2]Department of Physics and Engineering Physics, Tulane University, New Orleans, Louisiana 70118, USA

2.1 Introduction

Error correction via the encoding of logical qubits using multiple physical qubits is a very promising route towards fault-tolerant quantum computation [6]. While topological stabilizer codes like the surface code propose a blueprint to implement quantum error correction, they also require many physical qubits to encode a single logical qubit. For a distance-3 surface code, one logical qubit is encoded using 17 physical qubits [6]. Concurrently, research using engineered dissipation for stabilizing quantum states has been growing [5, 20–22]. Some prominent examples are cat codes [23–34], having already exceeded break-even [28], and the Very Small Logical Qubit (VSLQ) [4] where a logical qubit is encoded using only four physical qubits, coupling two high-coherence qubits each with two lossy qubits or resonators.

By modulating the coupling between two quantum devices, red-sideband photon exchange interactions $(a_1 a_2^\dagger + a_1^\dagger a_2)$ [35–37] and blue-sideband photon squeezing $(a_1 a_2 + a_1^\dagger a_2^\dagger)$ [37–40] can be achieved for autonomous state stabilization [41, 42]. The goal of this paper is to better characterize and understand the limiting error channels using the blue-sideband two photon creation and annihilation coupling used in our autonomous error correction schemes, and eliminate them with a pulse-reset technique. This is done with a numerically optimized, time-parameterized coupling strength with a time-varying lossy object. In the next section, we talk about how the use of quantum noise as engineered dissipation aids in the stabilization of a quantum state, which is the fundamental mechanism by which these small logical devices achieve autonomous error correction. We then discuss the limiting error syndrome induced by the error correction mechanism itself, whereby the coupling strength between the high-coherence and the lossy qubits may induce off-resonant transitions into unwanted leakage states. To minimize this effect, we introduce techniques borrowed from gate optimization by numerically optimizing a parametric, time-varying coupling strength, and qubit reset protocols that allow the lossy qubit enough time to reset as shown in Fig. 2.1 [3, 43–45].

We begin by looking at the simplest, idealized scenario of a single high-coherence, three-level qubit device with an unwanted leakage state, coupled to a single lossy qubit or oscillator to understand the stabilization mechanism and the limiting error. The numerical optimization of the time-parameterized coupling and the qubit reset protocols show a very clear advantage over a standard, fixed-coupling parameter space for single-qubit device state stabilization. This is done without assuming any specific architecture, the only criteria being having the ability to couple two qubit devices with strong coupling manipulation, and efficiently inducing qubit reset. To show the practicality of these techniques, we generalize its use on a three-qubit flip code, in which we look at how to optimize autonomous correction of a qubit-flip error syndrome. Having shown the improvement from using these techniques, we proceed to the more complex VSLQ, where applying these methods gives us a better performance over numerically optimizing the individual parameters in the system Hamiltonian.

2.2 Single-qubit stabilization

2.2.1 System

For a more thorough explanation on using engineered dissipation, we direct the reader to a full review on the subject [5]. We look at a very simple, idealized example similar to [41] as a warm-up show case for the more interesting and complex applications of error correction in the next sections. Consider a single high-coherence qubit device coupled to a single lossy qubit or resonator. Here, we consider the high-coherence qubit device to be a three-level system with a nonlinearity δ, and the lossy resonator to be a two-level system, as shown in Fig. 2.2(a). The lossy nature allows us to truncate the resonator to its first two energy states, since occupation of any higher states are extremely unlikely and do not contribute any meaningful dynamics. This also has the added benefit of faster simulations due to the smaller Hilbert space. For this example, our only focus is to stabilize a single, excited state for the high-coherence qubit device in the computational basis. However, engineered dissipation can be used to stabilize an arbitrary state along any axis on the

Bloch sphere, as described in [42].

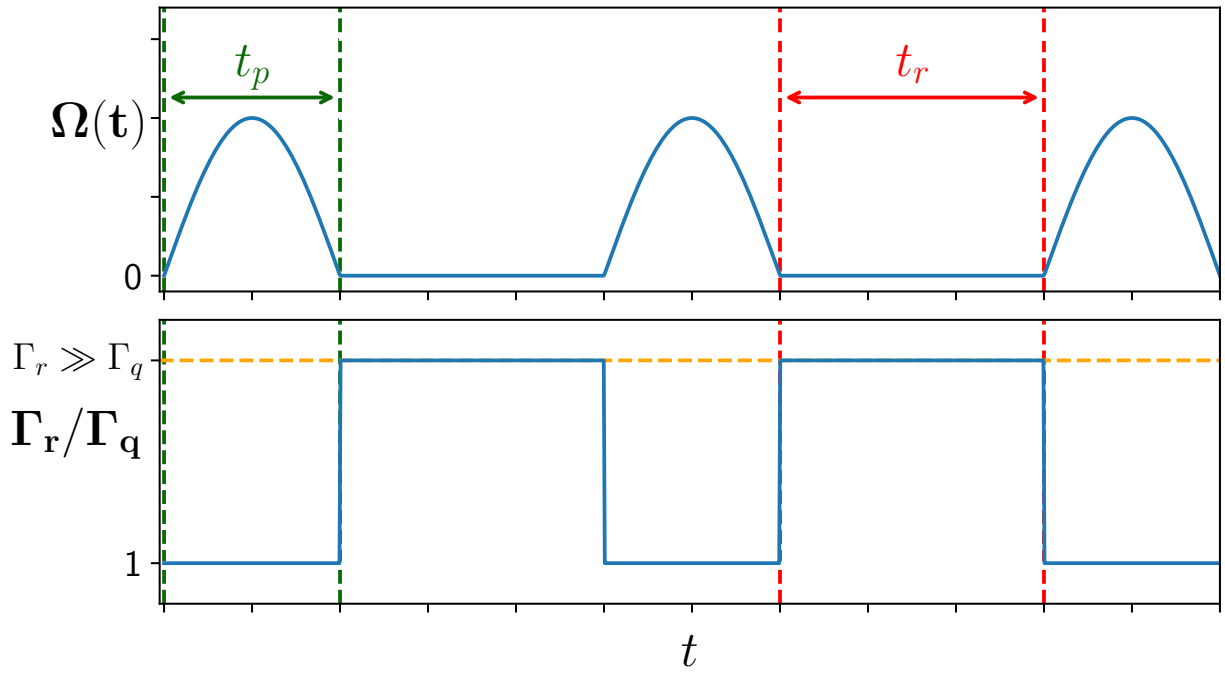

Figure 2.1: Scheme for the pulse-reset cycles. We denote the coupling duration as t_p (green), in which the qubit device and resonator are coupled using an optimized pulse shape. The reset cycle, t_r (red), is determined using a simple scan over different values to determine what gives the lowest residual error rate for each different T_1. We denote the loss rates as Γ_r for the resonator (or lossy qubit) and Γ_q for the qubit (or high-coherence qubit device), and the coupling strength as Ω. During t_p we set $\Gamma_r = \Gamma_q$ and $\Omega = \Omega_{opt}(t)$, while during t_r we have $\Gamma_r \gg \Gamma_q$ and $\Omega = 0$. It is assumed that qubit reset protocols, such as the one described in [3], can be performed efficiently, giving us an effective $\Gamma_r \gg \Gamma_q$.

We will refer to the high-coherence qubit device as simply the primary qubit, and the ancilla as just a resonator, using the subscripts q and r to denote them, respectively. The system is described by the Hamiltonian

$$H = \frac{\omega_q}{2}\sigma_q^z - \delta P_q^2 + \omega_r a_r^\dagger a_r + 2\Omega \cos 2\omega_0 t \left(a_q + a_q^\dagger\right)\left(a_r + a_r^\dagger\right), \tag{2.1}$$

where $P_q^2 = |2_q\rangle\langle 2_q|$ is the projection operator onto the primary qubit leakage state, and Ω is the strength of the blue-sideband coupling between the qubit and resonator. Moving to the rotating frame under the unitary transformation $U(t) = e^{-i(\omega_r n_r + \frac{1}{2}\omega_q \sigma_q^z)t}$, and discarding counter rotating terms as well as choosing an appropriate modulation of the coupling strength, we can write the rotating wave Hamiltonian of this system as

$$H = -\delta P_q^2 + \Omega \left(a_q a_r + a_q^\dagger a_r^\dagger \right). \tag{2.2}$$

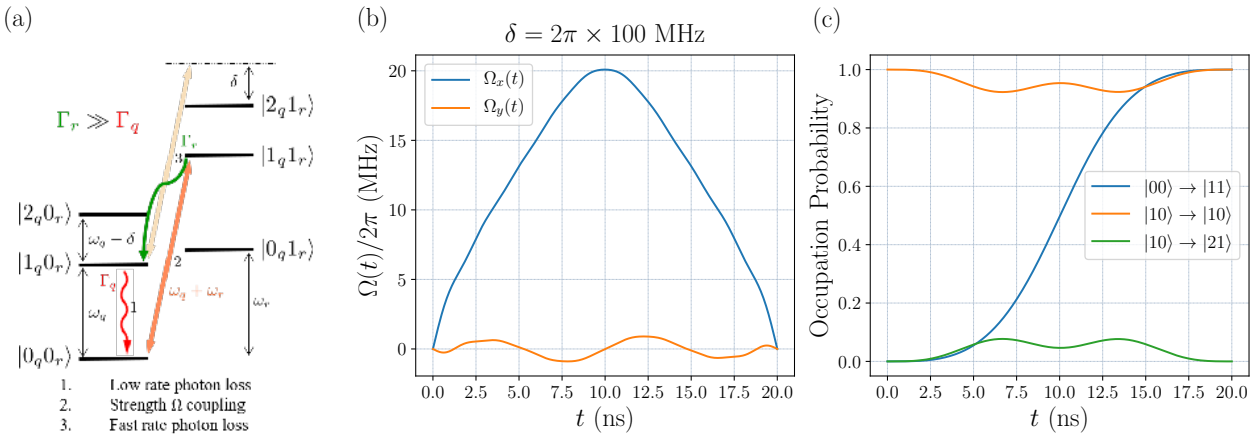

Figure 2.2: A high-coherence qubit device coupled to a lossy qubit or resonator with a coupling strength Ω. (a) An energy level diagram of the system. We only consider the ground state and first excited state of the resonator due to its lossy nature, making occupations of any higher states extremely unlikely. The protocol follows a photon loss in the primary qubit device (1), followed by the coupled excitation of both qubit device and resonator at strength Ω (2), and finally the relaxation of the resonator (3). (b) Optimized pulse shape for the operation $|0_q 0_r\rangle \to |1_q 1_r\rangle$ from a gradient ascent optimization. We let $N = 20$ in Eq. (2.3), and initialize $c_1^x = 2\pi \times 20$ MHz, $c_{n\neq 1}^x = 0$, and all $c_n^y = 0$, letting them vary by ϵ until we achieve a target state fidelity of 0.9989. All photon loss is turned off in this optimization, with the goal of trying to minimize errors induced by this mechanism itself. (c) We track the occupation probabilities of the transitions $|0_q 0_r\rangle \to |1_q 1_r\rangle$ (blue), $|1_q 0_r\rangle \to |1_q 0_r\rangle$ (orange), and $|1_q 0_r\rangle \to |2_q 1_r\rangle$ (green) from the qubit-resonator coupling (for compactness, the legend labels forego the subscripts: $|n_q m_r\rangle \equiv |nm\rangle$). The goal is to excite both qubit device and resonator in the event of a photon loss, leaving the target state unchanged while minimizing off-resonant transitions into the leakage state.

The dynamics of the autonomous error correction protocol for this example is as follows. In the event of a photon loss in the qubit, $|1_q 0_r\rangle \to |0_q 0_r\rangle$, the coupled drive will excite both the qubit and resonator into their first excited states, $|0_q 0_r\rangle \to |1_q 1_r\rangle$, after which the lossy resonator will bring the system back to the initial desired state, $|1_q 1_r\rangle \to |1_q 0_r\rangle$. The important conditions here are: 1. $\Gamma_q \ll \Gamma_r$, meaning the lossy resonator can quickly decay back to its ground state, bringing the entire system back to the initial state $|1_q 0_r\rangle$, and 2. $\delta \gg \Omega$, this reduces unwanted off-resonant transitions into the primary qubit leakage state induced by the coupling with the resonator. While this

scheme proves very efficient in achieving autonomous state stabilization, off-resonant transitions induced by the error correction mechanism itself present a limiting factor [46].

To that end, we use techniques in pulse engineering [47–52] to eliminate leakage during the qubit-resonator coupling, as well as a reset cycle which allows the resonator time to reset back to its ground state. After the pulsed operation $|0_q 0_r\rangle \rightarrow |1_q 1_r\rangle$, there is a non-zero probability that the primary qubit may undergo another photon loss before the resonator has decayed back to its ground state, $|1_q 1_r\rangle \rightarrow |0_q 1_r\rangle$. In this event, the coupling terms perform the transition $|0_q 1_r\rangle \rightarrow |1_q 2_r\rangle$, which is far off-resonant and less likely to accomplish the goal of taking the primary qubit to its first excited state. Thus the reset cycle ensures the resonator will be usable for correcting the qubit to $|1_q\rangle$. These two steps, laid out in in Fig. 2.1 are imperative to our approach of eliminating the limiting error channels of the standard, continuous coupling schemes.

2.2.2 Results

We borrow gate optimization techniques from [48] by pulse shaping an analogous two quadrature coupling strength, letting $\Omega \rightarrow \Omega_x(t), \Omega_y(t)$ [Fig. 2.2(b)], where

$$\Omega_{x,y}(t) = \sum_{n=1}^{N} c_n^{x,y} \sin\left(n\pi t/t_p\right), \tag{2.3}$$

with $\Omega_x(t)$ corresponding to the coupling term in Eq. (2.2), and another pulse component $\Omega_y(t)$ to eliminate leakage influenced by the DRAG protocol, giving us the effective Hamiltonian

$$H_{\text{eff}} = -\delta P_q^2 + \Omega_x(t)\left(a_q a_r + a_q^\dagger a_r^\dagger\right) + \Omega_y(t) i\left(a_q^\dagger a_r^\dagger - a_q a_r\right). \tag{2.4}$$

Using Eq. (2.3) allows us to set the conditions $\Omega_{x,y}(0) = \Omega_{x,y}(t_p) = 0$, while allowing us to use a gradient ascent numerical optimization over the $c_n^{x,y}$ coefficients for pulse shaping the $\Omega_{x,y}(t)$ terms. By letting c_1^x be some initial amplitude, and all other $c_{n\neq 1}^x, c_n^y = 0$, we find the optimized fidelity of the operation $|00\rangle \rightarrow |11\rangle$ so as to maximize the target state transition, while minimizing off-resonant transitions into the leakage state induced by the

coupling itself. This is evident in Fig. 2.2(c), where we can see the dips in the fidelity tracking for $|10\rangle \rightarrow |10\rangle$ and $|10\rangle \rightarrow |21\rangle$ (orange and green, respectively).

In addition to optimizing the pulse shape of the coupling strength, we use alternating pulse-reset cycles in which the blue-sideband coupling strength is determined by the optimized pulse shapes during the coupling cycles. During the reset cycles, the coupling strength is completely turned off while increasing the resonator decay rate so as to allow the resonator to reset back to its ground state. This effective, induced resonator reset can be achieved with techniques described in [3]. For simplicity of simulation, we assume that this reset protocol can be achieved with high fidelity and treat the decay rate as time-varying, which is high during the reset cycle and low during a coupling cycle (Fig. 2.1). We simulate these dynamics, as well as the following, more complex examples, with a continuous time evolution of Schrödinger equations for the pulse optimizations, and Lindblad master equations for the full pulse-reset cycle evolutions. For this single qubit stabilization example, we use the Hamiltonian Eq. (2.4) over a (3×2)-dimensional Hilbert space [Fig. 2.2(a)], and collapse operators $a_{q,r}$ with rates $\Gamma_{q,r}$.

We report a target state fidelity of 0.9989 [Fig. 2.2(c)] for the operation $|00\rangle \rightarrow |11\rangle$, using the resulting pulse shape in Fig. 2.2(b). However, it is important to note that experimental results in [41] achieve stabilization of the qubit excited and ground states with $> 90\%$ and $> 99\%$ purity, respectively. Meanwhile, stabilization of an arbitrary state along the Bloch sphere achieves a worst case average fidelity exceeding 80%. This apparent discrepancy is because the results presented in Fig. 2.2(b) and Fig. 2.2(c) are obtained without accounting for decoherence. This was done because the point is to reduce the limiting error induced from off-resonant transitions during the qubit-resonator coupling [[46]], and so the $\Omega_{x,y}(t)$ optimization is done without considering photon losses. The results of the residual error rate scaling using constant coupling strength versus optimized time-varying coupling strength and reset cycles are summarized in Fig. 2.3. While here we do consider photon loss for the full pulse-reset evolution, we still do not consider phase noise in an effort to keep this a simplified example of the use of this

technique. Further considerations for a more complete picture of single qubit stabilization, as well as a discussion on the broad range of factors to improve on experimental results, would introduce increasing complexity and would be a deviation from the main purpose of this paper.

For our comparisons, we let the fidelity $F \to F(T_1, \Omega, \Gamma_r)$, where for each different T_1, F is gradient-ascent optimized to find the best choice of Ω and Γ_r. While we do see a much improved scaling $\propto T_1^{-0.81}$, it is still short of the theoretical optimal $\propto T_1^{-1}$ [46]. However, given experimental limitations, this improvement is highly desirable over the asymptotically fixed coupling strength error scaling $\propto T_1^{-1/2}$, which is especially evident for short T_1. We note that the scaling for the data using fixed coupling strength (orange curve in Fig. 2.3) does not agree with the expected results from [46], which may be a result of the theoretical scaling being asymptotic, and not visible in the range of T_1 values explored. Likewise, while we expect the pulse-reset data scaling to approach unity (blue curve in Fig. 2.3), the presence of a 0.002 offset may suggest the technique itself is a limiting factor, or just another problem with the range of explored T_1 values. Nevertheless, we can still very clearly see a noticeable advantage in using pulse-resets over fixed coupling for short coherence times T_1, providing a meaningful showcase for the use of this technique.

We draw attention to the shape of the $\Omega_y(t)$ pulse as a result of the gradient ascent search. From Fig. 2.4, we see that the oscillatory behavior changes for different nonlinearity δ. Indeed, from Fig. 2.2(a) it is clear that having a larger nonlinearity reduces the probability for off-resonant transitions into the leakage state induced by the coupling strength. For $\delta = 2\pi \times \{100, 200, 350\}$ MHz, we see that the frequency of this $\Omega_y(t)$ counterterm strength is about 100, 200 and 350 MHz, respectively. This opens up the possibility of a more general use of oscillatory counterterms in driven fields for state stabilization, and further research will be required to understand this phenomenon.

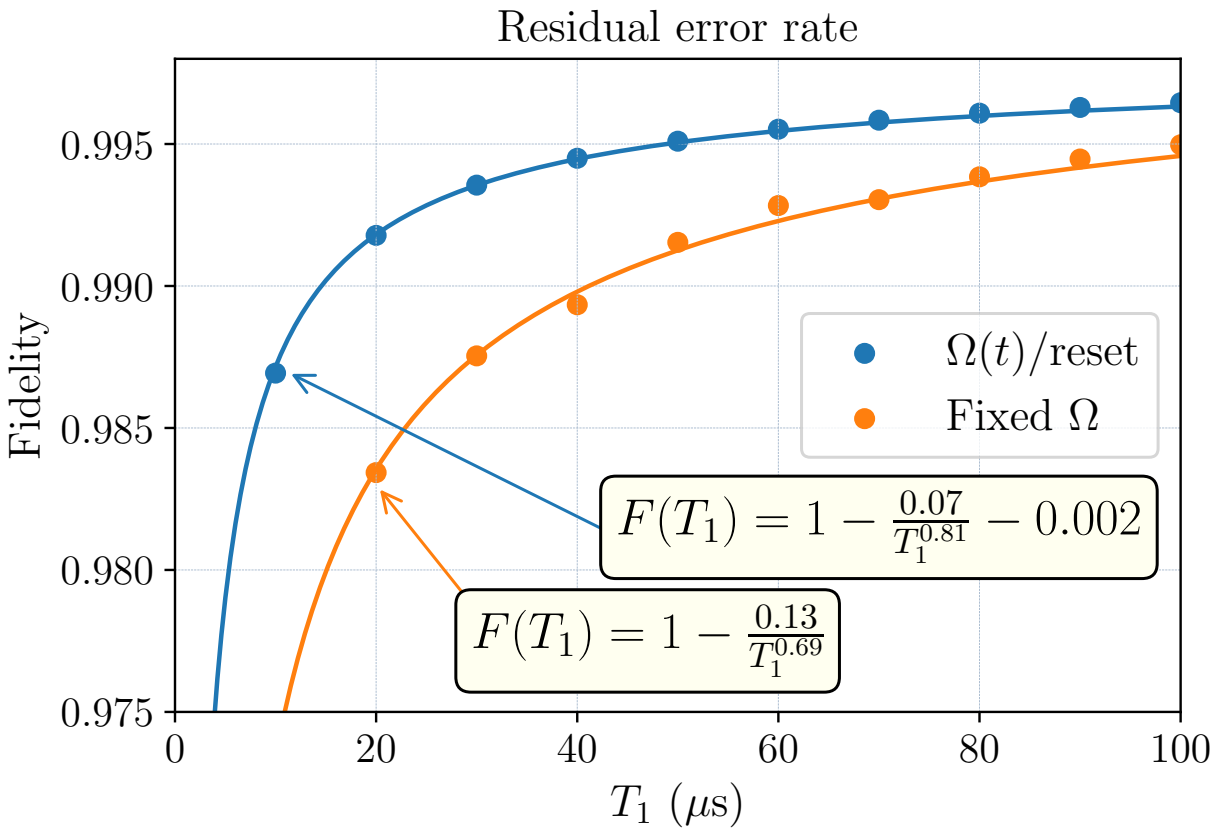

Figure 2.3: Residual error rate scaling with the fidelity calculated at the end of one pulse-reset cycle.

2.3 Three-qubit flip code

2.3.1 System

The single-qubit case we just discussed is a very simple demonstration of the potential in using this time-parameterized coupling technique for state stabilization. We now present the use of this technique in a more complex, yet still abstracted, system—the three-qubit flip code [13]. We consider a case proposed in [14] and [15] where we have 6 total qubits, three high-coherence qubits each coupled to three lossy qubits, with the primary qubits coupled to each other, and the lossy resonators decoupled from each other but coupled to a primary qubit each. Following the bit-flip code laid out in [15], by appropriately tuning flux-biased Josephson junction couplings between the primary qubits, and coupling the lossy qubits with a weak capacitive interaction with their respective primary qubits, we can achieve a rotating-frame Hamiltonian of the Jaynes-Cummings

form separating the system Hamiltonian into three parts for the high-coherence qubits (denoted as the primary qubits Hamiltonian H_P as in [5]), the lossy resonators H_R, and the interaction Hamiltonian for the coupling between the lossy and high-coherence qubits H_{PR}.

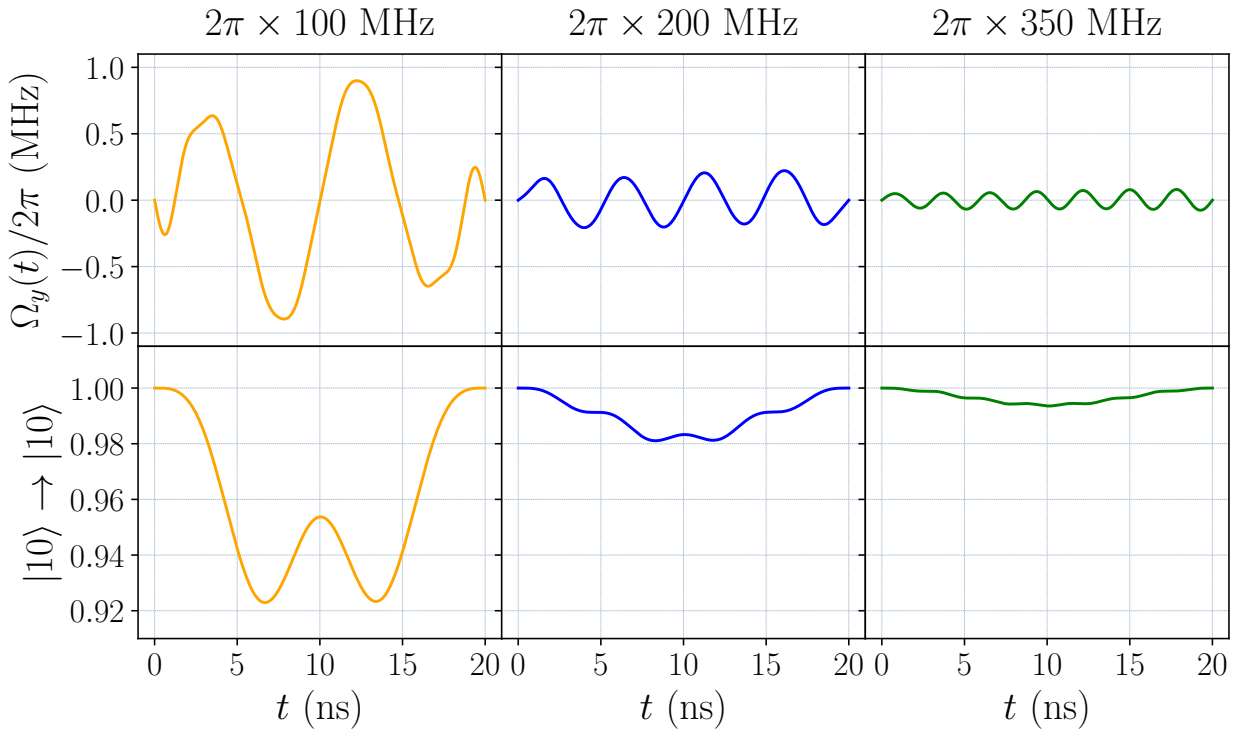

Figure 2.4: The effects of the $\Omega_y(t)$ terms on off-resonant, blue-sideband transitions for $\delta = 2\pi \times \{100, 200, 350\}$ MHz. There is a clear correlation between the effective oscillating counterterm and the size of δ. This is shown by tracking the occupation of the target state $|1_q 0_r\rangle$ (bottom plots), as well as the leakage state $|2_q 1_r\rangle$ in Fig. 2.2(c), having initialized in the target state $|1_q 0_r\rangle$.

We have

$$\begin{aligned} H &= H_P + H_R + H_{PR}, \\ H_P &= -J\left(\sigma_{1P}^z \sigma_{2P}^z + \sigma_{2P}^z \sigma_{3P}^z + \sigma_{1P}^z \sigma_{3P}^z\right), \\ H_R &= -2J \sum_{i=1}^{3} \sigma_{iR}^z, \;\; H_{PR} = \Omega \sum_{i=1}^{3} \sigma_{iP}^x \left(\sigma_{iR}^x + \sigma_{iR}^y\right), \end{aligned} \tag{2.5}$$

with J being the energy scale. While the idea is exactly the same as the single-qubit stabilization, there are some things to keep in mind that change the outcome of our goal. For this system, we are not trying to stabilize a single state but rather a logical manifold.

Namely, we are protecting either logical state $|0_L\rangle$ or $|1_L\rangle$, which are defined by the majority vote of the three primary qubits,

$$\begin{aligned} &|000\rangle, |100\rangle, |010\rangle, |001\rangle \rightarrow |0_L\rangle \\ &|111\rangle, |011\rangle, |101\rangle, |110\rangle \rightarrow |1_L\rangle . \end{aligned} \tag{2.6}$$

For either logical state, two flip errors on physical qubits is a logical flip error.

Again, just like we got to Eq. (2.4), we look at replacing Ω in Eq. (2.5) with a two quadrature parametric coupling $\Omega(t)$ from Eq. (2.3), and optimizing it with a gradient ascent. This system is significantly different, however, in that it is more abstracted. Rather than trying to correct photon losses in the primary qubits, we are addressing bit-flip errors. With this error syndrome, we let the Lindblad operators and error rates for the system be $\sigma^x,\ \Gamma_P$ for the primary qubits and $\sigma^-,\ \Gamma_R$ for the lossy qubits. Additionally, because we constrain the system to bit-flip operations instead of ladder operators as collapse operators for the primary qubits, and to maintain a smaller Hilbert space, we only consider the computational space and ignore higher energy leakage states ($|2\rangle, |3\rangle ...$) for all 6 qubits. Whereas for the single-qubit system we make use of optimized coupling strength pulse shapes to perform a target operation with high fidelity while eliminating off-resonant transitions into these higher energy leakage states, here we are trying to eliminate off-resonant qubit flips induced by the coupling mechanism itself, for example, $|000\rangle_P \otimes |000\rangle_R \rightarrow |100\rangle_P \otimes |100\rangle_R$ in attempting to protect $|0_L\rangle$. And so, this is a very useful example in demonstrating autonomous, high fidelity, time-parameterized coupling strength for error correction while eliminating unwanted off-resonant operations.

The goal of applying this lossy coupling technique is, therefore, to protect the logical states by autonomously correcting flip errors corresponding to the appropriate parent logical state. So we can't simply just flip any $|0\rangle$ states to $|1\rangle$ like we did for the single-qubit stabilization, since our target operation will depend on which logical state we are trying to protect. The target operations for $\Omega_x(t)$ and $\Omega_y(t)$ would be such that the

majority is respected. For example,

$$\begin{aligned} |100\rangle_P \otimes |000\rangle_R &\rightarrow |000\rangle_P \otimes |100\rangle_R \\ |101\rangle_P \otimes |000\rangle_R &\rightarrow |111\rangle_P \otimes |010\rangle_R , \end{aligned} \tag{2.7}$$

where our time-dependent interaction Hamiltonian would be

$$H_{PR} = \sum_{i=1}^{3} \sigma_{iP}^{x} \left(\Omega_x(t) \sigma_{iR}^{x} + \Omega_y(t) \sigma_{iR}^{y} \right) . \tag{2.8}$$

Note from Eq. (2.7) that these operations are achieved by the red- and blue-sideband couplings described in [42, 7].

We emphasize that like the single-qubit stabilization example, this system is still idealized and abstracted. A more thorough characterization that includes leakage states would be needed for a more realistic demonstration of using a pulse-reset evolution with a qubit-flip error syndrome. However, as we saw for the single-qubit case, it is safe to assume that with a large enough nonlinearity, and with the oscillating $\Omega_y(t)$ counterterm having numerically optimized a time-parameterized coupling strength, we can reasonably exclude leakage transitions from our simulations.

2.3.2 Results

We summarize the results for this system in Fig. 2.5. The $\Omega_y(t)$ pulse shape in Fig. 2.5(a) does not have the same oscillatory behavior as we saw for the single-qubit case, which is consistent with our exclusion of a leakage state and thus no nonlinearity to correlate to. Instead, we see a pulse shape that more so resembles the time derivative of the $\Omega_x(t)$ term, with the exception of the condition $\Omega_y(0) = \Omega_y(t_p) = 0$. This shows us another example of the benefit of a second pulse quadrature in the coupling strength in an effort to eliminate unwanted, off-resonant flip operations. While we still see a very small probability of unwanted transitions out of the target logical state $|000\rangle$ during the pulse evolution, seen in Fig. 2.5(b), we report a very good target operation Eq. (2.7) fidelity of $1 - F < 10^{-6}$.

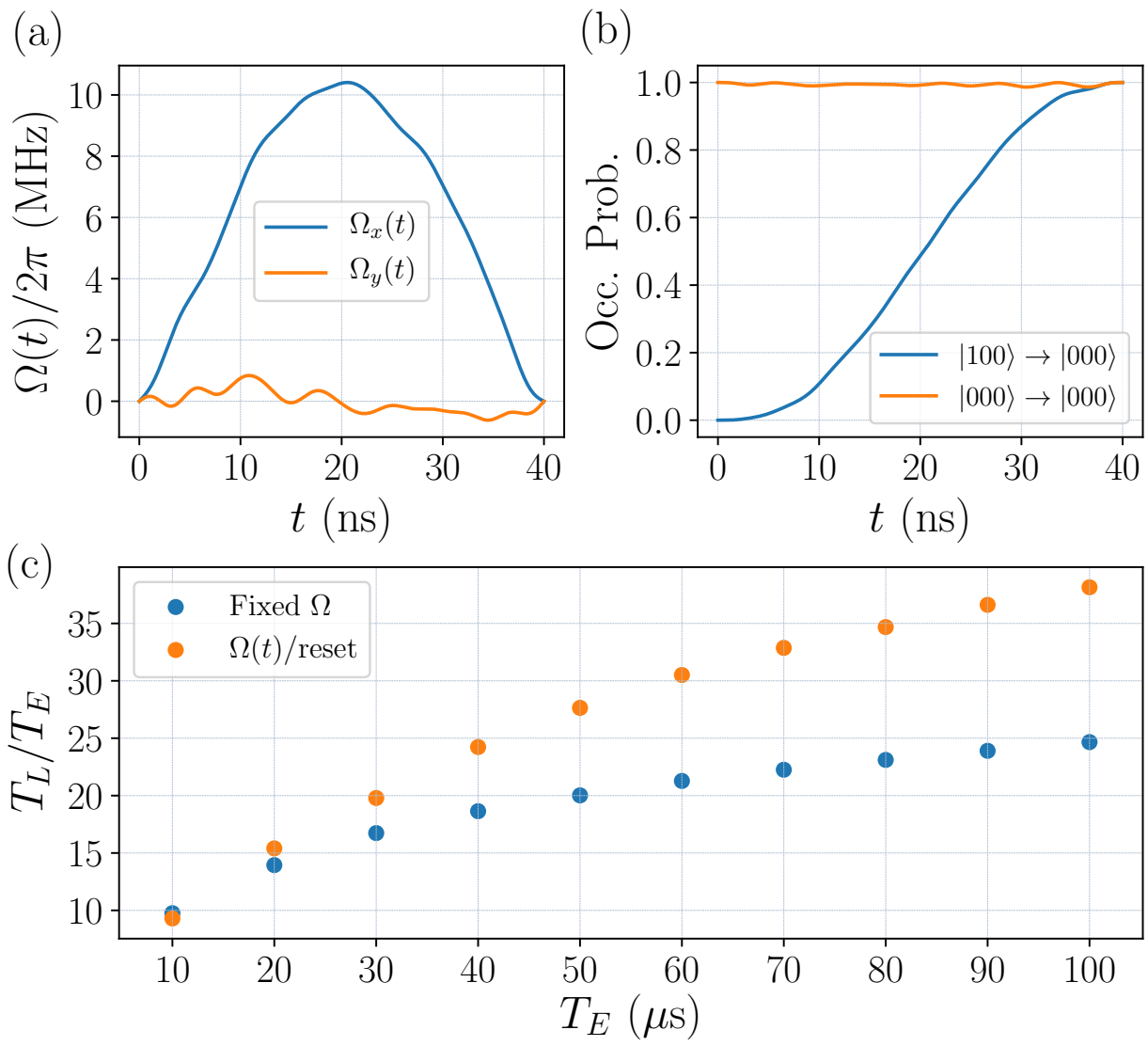

Figure 2.5: Results for the three qubit code using $J = 2\pi \times 20$ MHz and $\Gamma_R = 30\ \mu s^{-1}$. (a) The optimized pulse shape for the target operations in Eq. (2.7), as well as (b) tracking the occupation probability for $|000\rangle_P$, where a final operation fidelity of 0.99999635 is achieved. Note that the states in the legend are only the primary qubits subspace and that the operation evolution is without decoherence. (c) Improvement factor T_L/T_E for the states $|000\rangle_P$ and $|111\rangle_P$, with increasing error times T_E. The state evolutions for these last results do include decoherence. Results in (a) and (b) were obtained with no bit-flip errors, while results in (c) do include bit=flip errors.

We compare the logical lifetimes T_L to single qubit error times T_E, as opposed to T_1, where $T_E = 1/\Gamma_P$ is the single qubit lifetime under a qubit-flip error syndrome instead of photon losses. The lifetime improvement for the states $|000\rangle_P$ and $|111\rangle_P$ has a much better scaling for increasing error times T_E, seen in Fig. 2.5(c). This is still not a linear

scaling, indicative that there are other residual error rates that become dominant for larger T_E, but the improvement is very significant over using individually optimized fixed coupling strengths.

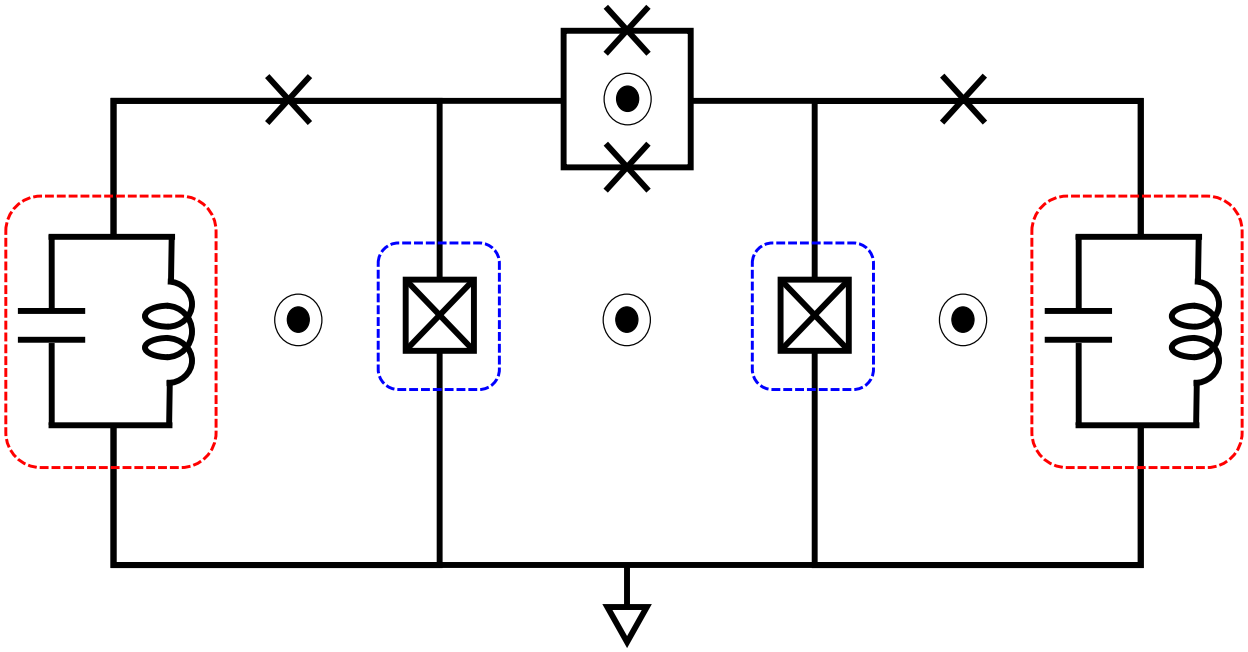

Figure 2.6: A possible implementation of the logical qubit, similar to [4]. The high-coherence primary qubits are in blue boxes, and the lossy resonators (or qubits) are in red boxes. The approximated rotating wave Hamiltonian [Eq. (2.9)] is achieved by modulating the flux drives in the diagram. We refer to the elements of this circuit as shadow left and shadow right (Sl and Sr respectively) for the lossy resonators (red boxes), and simply left and right (l and r) for the primary qubits (blue boxes).

2.4 VSLQ

A simple yet effective architecture, the VSLQ shows great promise in protecting a logical state against single-photon loss errors while suppressing phase errors, all while depending on fully available technology. Having shown the applicability of this pulse-reset technique on a more complicated system, we now apply it to a more realistic implementation, the VSLQ [4, 5].

2.4.1 System

This circuit consists of two coupled high-coherence qubits each coupled to a lossy qubit or resonator, as shown in Fig. 2.6. Following the derivation of the approximated rotating

wave Hamiltonian from [4], and using the same notation—where we denote the primary system Hamiltonian by H_P, the lossy (shadow) system Hamiltonian by H_S, and the coupling Hamiltonian by H_{PS}, we have $H = H_P + H_S + H_{PS}$, with

$$\begin{aligned} H_P &= -W\tilde{X}_l\tilde{X}_r + \frac{\delta}{2}\left(P_l^1 + P_r^1\right) \\ H_S &= \left(W + \frac{\delta}{2}\right)\left(a_{Sl}^\dagger a_{Sl} + a_{Sr}^\dagger a_{Sr}\right) \\ H_{PS} &= \Omega\left(a_l^\dagger a_{Sl}^\dagger + a_r^\dagger a_{Sr}^\dagger + \text{H.c.}\right), \end{aligned} \tag{2.9}$$

where δ is a nonlinearity, $\tilde{X}_k = \left(a_k^\dagger a_k^\dagger + a_k a_k\right)/\sqrt{2}$, $P_k^n = |n_k\rangle\langle n_k|$, $k = \{l, r\}$, and we require that for the error correction mechanism to work,

$$\delta \gg W \gg \Omega. \tag{2.10}$$

Here H_P denotes the Hamiltonian for the primary qubits (blue boxes in Fig. 2.6), where we only consider the first three levels as the operating space and ignore higher energy states ($|3\rangle, |4\rangle, ...$) so as to reduce the size of the Hilbert space and ease numerical simulations. H_S is the Hamiltonian for the "shadow" resonators (red boxes in Fig. 2.6), with H_{PS} the interaction Hamiltonian.

Using the eigenstates for Eq. (2.9), we can define a logical manifold:

$$\begin{aligned} |0_L\rangle &= \frac{1}{\sqrt{2}}\left(|0_l\rangle + |2_l\rangle\right) \otimes \frac{1}{\sqrt{2}}\left(|0_r\rangle + |2_r\rangle\right) \otimes |0_{Sl}0_{Sr}\rangle \\ |1_L\rangle &= \frac{1}{\sqrt{2}}\left(|0_l\rangle - |2_l\rangle\right) \otimes \frac{1}{\sqrt{2}}\left(|0_r\rangle - |2_r\rangle\right) \otimes |0_{Sl}0_{Sr}\rangle. \end{aligned} \tag{2.11}$$

These states are autonomously protected against single-photon losses by the blue-sideband coupling in H_{PS}, which is only energetically preferred in the event of a photon loss in one of the primary qubits, leading to long lifetimes of the logical states. This is very similar to the blue-sideband coupling for the single-qubit case shown in Fig. 2.2(a). A major difference here is that instead of trying to stabilize a single excited state, the goal is to stabilize these superposition states. So while a single photon loss can take the system out of the logical manifold into an error state

$$|\text{Err}_l\rangle = |1_l\rangle \otimes \frac{1}{\sqrt{2}}\left(|0_r\rangle \pm |2_r\rangle\right) \otimes |0_{Sl}0_{Sr}\rangle, \tag{2.12}$$

transitions into this state can be induced by H_{PS} for the primary qubits, with the shadows going to $|1_{Sl}0_{Sr}\rangle$. In addition to attempting to minimize these unwanted transitions by $\Omega(t)$, we could also consider transitions into higher energy states. Although highly unlikely, the $\tilde{X}$ operators could induce transitions into $|4\rangle$, which could then stabilize a superposition of $|2\rangle + |4\rangle$, a leakage state. Moreover, accounting for higher excited states would mean consideration of the possibility of the $\tilde{X}$ terms taking an error state $|1\rangle$ into a superposition of $|1\rangle + |3\rangle$. However, given the condition Eq. (2.10), such off-resonant transitions are extremely unlikely due to increasing nonlinearities with increasing energy. Thus for these simulations we limit the primary qubits to three-level systems, and try to address the much more likely transition $|0\rangle + |2\rangle \to |1\rangle$. The Lindblad operators are $\{a_{Sl}, a_l, a_r, a_{Sr}\}$, and we compare the logical state lifetimes T_L against the single qubit lifetime $T_1 = 1/\Gamma_P$, with Γ_P being the photon loss rate for the primary qubits (Γ_S for the shadow). We assume that it is significantly more likely this error state will be corrected as opposed to finding a higher energy state.

The optimized pulse shape will correspond to the interaction Hamiltonian

$$H_{PS} = \Omega_x(t)\left(a_l^\dagger a_{Sl}^\dagger + a_r^\dagger a_{Sr}^\dagger + \text{H.c.}\right) + \Omega_y(t)i\left(a_l^\dagger a_{Sl}^\dagger + a_r^\dagger a_{Sr}^\dagger - \text{H.c.}\right), \tag{2.13}$$

just like we did for the single- and three-qubit cases, with the same goal of having this pulse shape reduce changes to our target logical states defined in Eq. (2.11) and achieving the target operation

$$|1_l\rangle \otimes \frac{1}{\sqrt{2}}\left(|0_r\rangle \pm |2_r\rangle\right) \otimes |0_{Sl}0_{Sr}\rangle \to \frac{1}{\sqrt{2}}\left(|0_l\rangle + |2_l\rangle\right) \otimes \frac{1}{\sqrt{2}}\left(|0_r\rangle + |2_r\rangle\right) \otimes |1_{Sl}0_{Sr}\rangle \tag{2.14}$$

with high fidelity. During the reset cycle, where $\Gamma_S \gg \Gamma_P$, the lossy qubit returns to its ground state $|1_{Sl}0_{Sr}\rangle \to |0_{Sl}0_{Sr}\rangle$, returning the state to the logical manifold defined in Eq. (2.11).

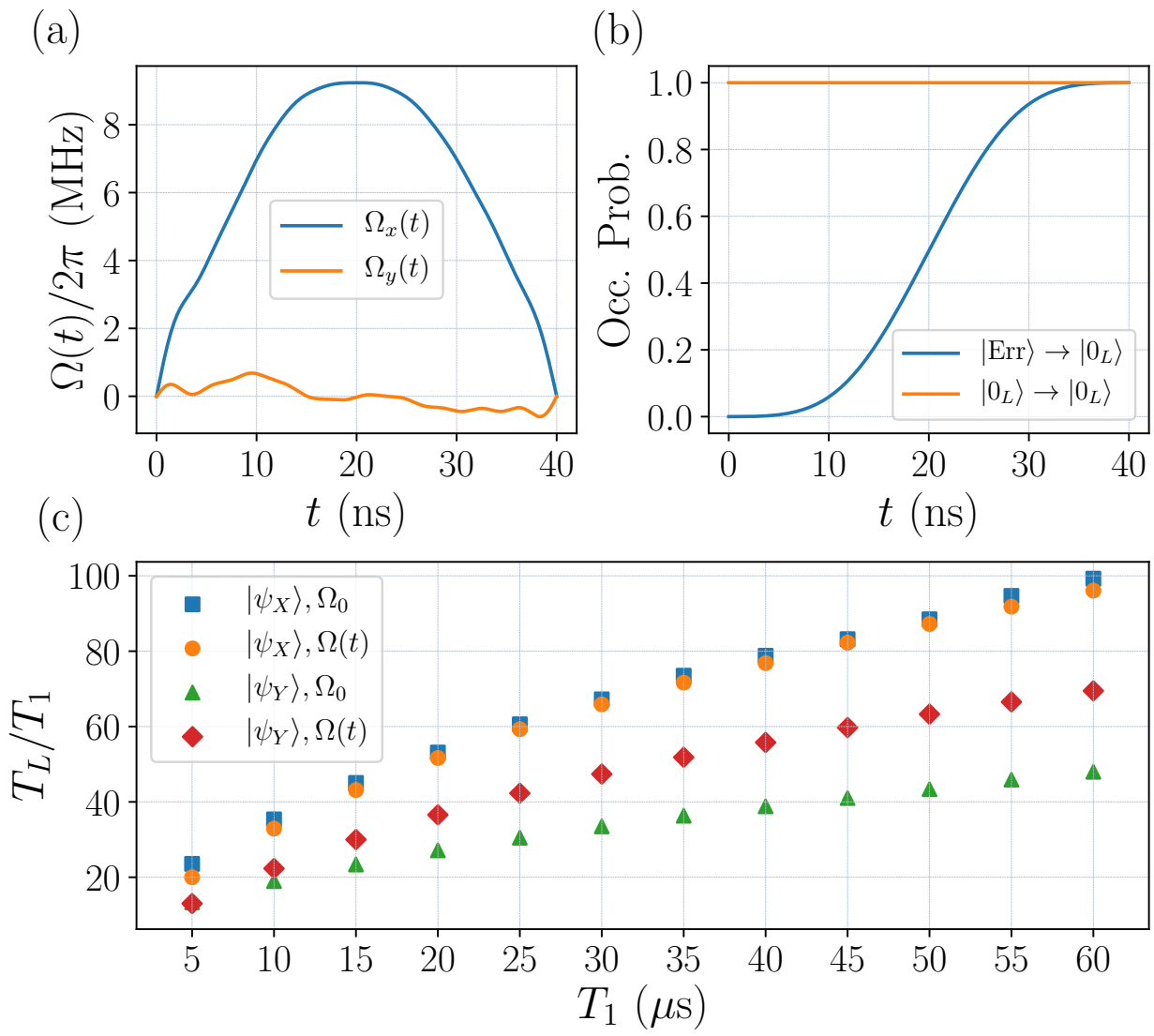

Figure 2.7: Results for the VSLQ. (a) Optimized $\Omega_x(t)$ and $\Omega_y(t)$ pulse shapes. (b) High-fidelity target operation of 0.99991 while leaving the target states unchanged. (c) We see the effects of lifetimes for X_L eigenstates and Y_L eigenstates, using definitions from [4]. Blue and green are the improvement factors using fixed operating parameters (Table 2.1) for the X_L and Y_L eigenstates, respectively, while orange and red are the improvement factors using pulse-reset cycles. Again, (a) and (b) do not include decoherence, while (c) does.

2.4.2 Results

These results using pulse-reset cycles are summarized in Fig. 2.7. We compare these to results from running a gradient ascent over the fixed parameter space $\{\Omega, \omega_S, \Gamma_S\}$, summarized in Table 2.1. These fixed parameter results are our benchmark in looking for

an improvement from our pulse-reset protocol.

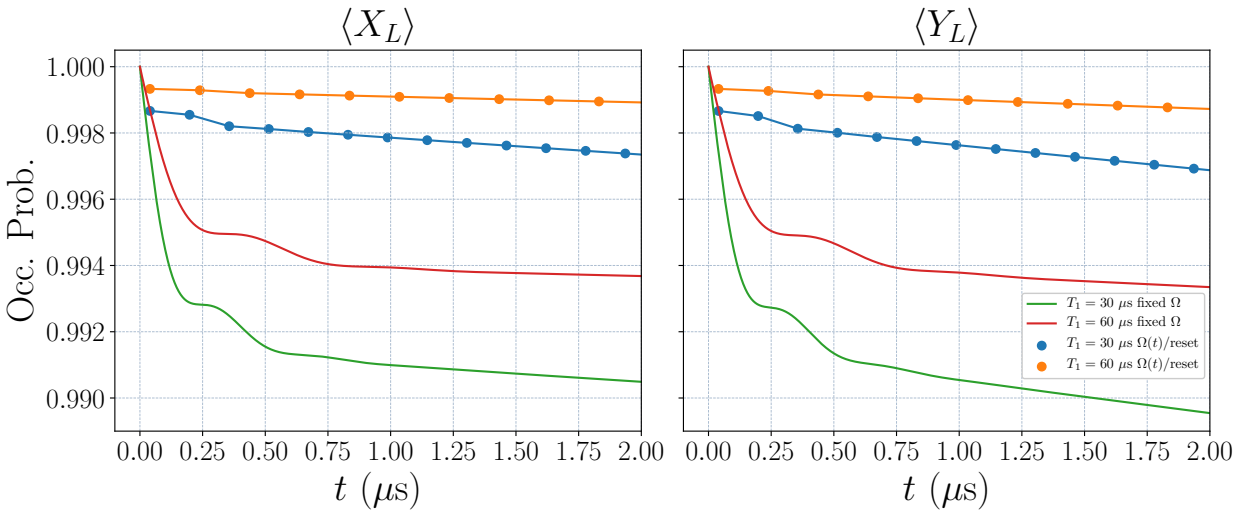

Figure 2.8: Short-time evolution for the VSLQ X_L eigenstates (left) and Y_L eigenstates (right). We compare using fixed parameters from Table 2.1 versus using pulse-reset (flushed) cycles for $T_1 = 30, 60$ μs.

Using the optimized pulse shapes for $\Omega_x(t)$ and $\Omega_y(t)$ from Fig. 2.7(a), we achieve an operation fidelity of $1 - F < 10^{-4}$, without any noticeable transitions out of the target state $|0_L\rangle$ [Fig. 2.7(b)]. We can see that this technique does not show an improvement for the long-time X_L eigenstate lifetimes over using individually, optimized fixed parameters [Fig. 2.7(c)]. However, the improvement in the lifetimes for the Y_L eigenstates is very evident. Moreover, the pulse-reset evolution shows a significant improvement over fixed parameters for short-time evolutions, as shown in Fig. 2.8. Here, we see that for both X_L and Y_L eigenstates, there is a very noticeable advantage, which will prove significantly important for gate operations on the device. In using $\Omega(t)$, we also scan over different reset times for each T_1, since each will have a different probability of having a photon in the lossy qubit after the pulse duration $t_p = 40$ ns.

The loss rate for this lossy qubit is $\Gamma_S = 35$ μs^{-1} for all different T_1 *during* the reset cycle, and again, $\Gamma_S = \Gamma_P$ during the pulse cycles. While there is a general lack of improvement for the X_L eigenstate lifetimes, this is not the case for the Y_L eigenstates, where we use the definitions from [4] to define $Y_L = iX_LZ_L$, with $X_L = \tilde{X}_l$ or $\tilde{X}_r$, and

$Z_L = \tilde{Z}_l \tilde{Z}_r$ with $\tilde{Z}_k = P_k^2 - P_k^0$. We see in Fig. 2.7(c) that there is a clear advantage in the Y_L lifetimes using pulse-reset cycles over fixed operating parameters. While we still expected to see an advantage for the X_L eigenstates as well, we may be seeing these results because of the Y_L eigenstates' sensitivity to more error channels than the X_L eigenstates.

Table 2.1: Gradient ascent results for the lifetimes of logical X-eigenstates and Y-eigenstates—denoted T_X and T_Y, respectively, over the fixed parameter space of the VSLQ with $W = 2\pi \times 35$ MHz, and $\delta = 2\pi \times 350$ MHz. Note the lossy qubit energy approaches the energy from Eq. (2.9), $\omega_S = W + \delta/2 = 2\pi \times 210$ MHz.

T_1 (μs)	$\Omega/2\pi$ (MHz)	Γ_S (μs^{-1})	$\omega_S/2\pi$ (MHz)	T_X (μs)	T_Y (μs)
5	2.94	24.66	209.75	117	66
10	2.15	18.40	209.83	353	189
15	1.81	15.32	209.90	675	350
20	1.59	13.26	209.92	1061	542
25	1.43	12.09	209.94	1514	762
30	1.31	11.09	209.95	2016	1005
35	1.22	10.30	209.96	2571	1271
40	1.14	9.67	209.96	3151	1553
45	1.08	9.15	209.96	3743	1846
50	1.02	8.73	209.97	4422	2168
55	0.98	8.38	209.97	5207	2524
60	0.93	8.04	209.97	5955	2879

To see this more clearly, consider the X_L eigenstate $|0_L\rangle$ from Eq. (2.11) undergoing a photon loss in the left qubit, taking the system to the error state in Eq. (2.12). Photon loss errors in the device are left-right symmetric. For this example we consider an error in the left qubit first only for simplicity, but the same conclusion would be reached starting with a photon loss in the right qubit. As previously explained, this state can then either be corrected back to the logical manifold, or undergo a second photon loss with lower probability on either qubit. In the event of a second photon loss occurring in the right qubit, then the system will be taken to the $|1_l 1_r 0_{Sl} 0_{Sr}\rangle$ state, which is uncorrectable with autonomous error correction having lost all information from the original state. This is considered a logical leakage state for the VSLQ. However, if the second photon loss occurs

in the left qubit, then this can take the system to either state:

$$
\begin{aligned}
|\psi_1\rangle &= \frac{1}{\sqrt{2}}\left(|0_l\rangle - |2_l\rangle\right) \otimes \frac{1}{\sqrt{2}}\left(|0_r\rangle + |2_r\rangle\right) \otimes |0_{Sl}0_{Sr}\rangle\,, \text{ or} \\
|\psi_2\rangle &= \frac{1}{\sqrt{2}}\left(|0_l\rangle + |2_l\rangle\right) \otimes \frac{1}{\sqrt{2}}\left(|0_r\rangle + |2_r\rangle\right) \otimes |0_{Sl}0_{Sr}\rangle\,.
\end{aligned}
\tag{2.15}
$$

Having started in $|0_L\rangle$, the first possible outcome from a second loss in the left qubit is an error for any state, while the second is just $|0_L\rangle$, and is therefore not seen as an X_L eigenstate error. However, this last photon loss channel is an error channel for a Y_L eigenstate. And so, this may be why using an optimized target operation for this autonomous mechanism shows a significant improvement in the Y_L lifetimes, but not for the X_L lifetimes.

Regardless of the difference in the long-time performance for the X_L and Y_L eigenstates, we note that the short-time performance of the pulse-reset evolution still outperforms a fixed parameter evolution for either eigenbasis, as seen in Fig. 2.8. This suggests a very practical use case for short-time applications. Implementing dissipative engineering in digital error correction codes is a very attractive prospect. For example, in the case of the surface code, each error-correction cycle consists of repeated measurement and resetting in short-time periods. Using the advantage in the short-time behavior of the pulse-reset cycle, and a proposed scheme for gates in small logical qubits [53], would provide a very relevant improvement in gate fidelity and error detection by incorporating small logical qubits within digital codes. This suggests a much more dramatic improvement in long-term error correction than is suggested in Fig. 2.7. Exploring this further will be the focus of future work.

2.5 Conclusion

We have demonstrated the use of time-parameterized coupling strength and variable loss rates in engineered dissipation for higher-fidelity state stabilization. We accomplished this by using alternating pulse cycles and reset times as shown in Fig. 2.1. This showed very noticeable advantages for an idealized single-qubit stabilization scheme and for a more complex bit-flip error-correction code. However, for the VSLQ we saw a mixture of

results, where the pulse-reset evolutions showed a very clear advantage for the VSLQ eigenstates over short-time evolutions, while giving comparable results as fixed coupling for the long-time evolutions of the VSLQ's X_L eigenstates. Moreover, we did see a clear advantage in prolonging the logical lifetimes of Y_L eigenstates, all of which is a great showcase for the use of this technique for a promising architecture, especially with gate implementations.

Nevertheless, while using autonomous error correction achieves significantly longer lifetimes over their component qubits for superconducting architectures, it comes at the cost of increased complexity. This is something that will need to be carefully characterized for further implementations of small logical qubits in larger quantum computing systems, since physically implementing 2-qubit gates for small logical qubits will in itself be a complex task. However, we have shown that using numerical pulse-shaping can help us achieve highly optimized target operations. For the VSLQ, this could be used to convert leakage errors into logical errors, which are then correctable with dissipative engineering. A leakage state $|1_l 1_r 0_{Sl} 0_{Sr}\rangle$ is both induced, and uncorrectable, by autonomous error correction using fixed operating parameters. However, using a pulse-reset technique with time-varying coupling optimized to perform a target operation taking either qubit from $|1\rangle$ to $|0\rangle + |2\rangle$ has the potential to be used for correcting $|1_l 1_r 0_{Sl} 0_{Sr}\rangle$. This ability to induce transitions from a leakage error state to an ordinary logical error state for the VSLQ would be a key function if ever incorporating small logical qubits into digital error-correction codes.

Further research will be needed to fully understand other prevalent error channels for small logical qubit architectures—especially those involving higher energy states in primary high-coherence qubit devices—as well as limitations of this pulse-reset technique. We would also like to explore whether this technique would provide any sort of advantage in gates for small logical qubits [53], an important characterization for further implementation of these qubits towards fault-tolerance.

2.6 Acknowledgements

We would like to thank Nick Materise and Zhijie Tang for the many conversations that helped advance this project. This work was supported by the NSF grant (PHY-1653820) and ARO grant No. W911NF-18-1-0125. It was made possible by the high performance computing resources from the Tulane University Cypress platform, and the Colorado School of Mines Wendian platform.

CHAPTER 3

ERROR-DIVISIBLE TWO-QUBIT GATES

David Rodríguez Pérez [*] [1], Ziqian Li[2], Tanay Roy[2], Eliot Kapit[1], David Schuster[2]

Abstract

We introduce a simple, widely applicable formalism for designing “error-divisible" two qubit gates: a quantum gate set where fractional rotations have proportionally reduced error compared to the full entangling gate. In current noisy intermediate-scale quantum (NISQ) algorithms, performance is largely constrained by error proliferation at high circuit depths, of which two-qubit gate error is generally the dominant contribution. Further, in many hardware implementations, arbitrary two qubit rotations must be composed from multiple two-qubit stock gates, further increasing error. This work introduces a set of criteria, and example waveforms and protocols to satisfy them, using superconducting qubits with tunable couplers for constructing continuous gate sets with significantly reduced error for small-angle rotations. If implemented at scale, NISQ algorithm performance would be significantly improved by our error-divisible gate protocols.

3.1 Introduction

Many advances in quantum hardware have focused on working towards fault-tolerant, universal quantum computation [54–56]. However, the challenge of engineering a fully, error-correcting logical qubit is a formidable one, and advances in state coherence and gate errors need significant improvement before quantum computation reaches fault-tolerance. Nevertheless, current qubit implementations have reached coherence and control levels such that they can perform NISQ algorithms [57], and may even be able to run tasks which surpass classical computers [58]. NISQ variational algorithms, such as VQE and QAOA [59–62], have proven particularly useful in approximating the ground state energy of difficult Hamiltonians. However, the performance of these algorithms depends on the

[*]Primary and corresponding author, drodriguezperez@mines.edu.
[1]Department of Physics, Colorado School of Mines, Golden, Colorado 80401, USA.
[2]James Franck Institute, University of Chicago, Chicago, Illinois 60637, USA.

circuit depth that can be achieved, which in turn depends on qubit coherence and gate error.

The inaccuracy of modern quantum algorithm implementations is dominated by two-qubit gate errors, as single-qubit gate errors are typically an order of magnitude smaller [63–68]. This is compounded by the traditional approach of implementing arbitrary two-qubit gates using a stock gate set, in which the large numbers of two-qubit rotations that may be required by a variational algorithm could be decomposed into at most three CZ gates and additional single-qubit gates [69]. While this gate decomposition is crucial for digital error correcting codes [54], it proliferates gate error for NISQ algorithms needing a more diverse two-qubit gate set. To address this, research in implementing continuous sets of gates that perform arbitrary two-qubit rotations [70, 71] has shown up to a 30% reduction in gate depth [72].

This work presents error-divisible gates, which realizes smaller angle, two-qubit rotations that are prevalent in variational algorithms. The realization of smaller-angle rotations is done so at a corresponding smaller gate time—e.g. for full θ rotations at gate time t_q, $\theta/2$ rotations are done at $t_g/2$ time. This can provide an opportunity to execute even deeper circuits with a larger number of two-qubit operations, given the further reduction in energy loss by virtue of having shorter gates.

3.1.1 Error divisibility

The basic idea for error divisibility is to implement a small two-qubit gate rotation without using multiple larger-rotation gates by instead proposing waveforms that are pulse-shaped to perform fractional rotations at a corresponding fractional gate time. This is illustrated in figure 3.1(a), where a full two-qubit rotation θ_0 is achieved a gate time t_g, and fractional rotations θ_0/n are run with corresponding gate times t_g/n. The full gate time t_g is chosen as small as possible so that the rotation θ_0 is executed at a chosen, acceptable intrinsic error rate (not considering qubit decoherence). The fractional two-qubit gates implemented with the proposed protocol do not increase intrinsic qubit

error significantly.

To address the difficulty in pulse-shaping gates of variable length for different target rotations, this work borrows ideas from [73] and [19], in which off-resonant energetics are used to suppress dispersive shift effects. We propose simple waveforms that are superimposed Gaussian-like wave envelopes with fast-oscillating counterterms, as shown in figure 3.1(b). These waveforms do not require a high level of fine-tuning, and significant errors are not introduced from small variations in the final waveform. The fast-oscillating counterterm serves to suppress intrinsic gate error throughout the duration of the gate. Namely, the ones this work focuses on are leakage into higher-energy excited states, and dynamic stray ZZ interactions that can create an effective partial CPHASE. These processes are the result of off-resonant mixing throughout the gate, which can be mitigated by additional off-resonant processes—realized as the fast-oscillating counterterms. This is illustrated in figure 3.1(c), where suppression of the gate error through the duration of the gate can be seen as a result of the oscillating waveform. The dashed red line indicates the maximum gate error, which can be reduced through minimal fine tuning of the waveform's small parameter space.

While the work presented here completely ignores random qubit error like amplitude dampening and dephasing, these are automatically addressed by the fact that this protocol shortens the gate time for each smaller rotation angle, allowing less time for decoherence. This provides an even bigger reduction in the error per gate than other continuous gate implementations [70, 71], allowing for a greater circuit depth for NISQ algorithms without a significant increase in gate complexity.

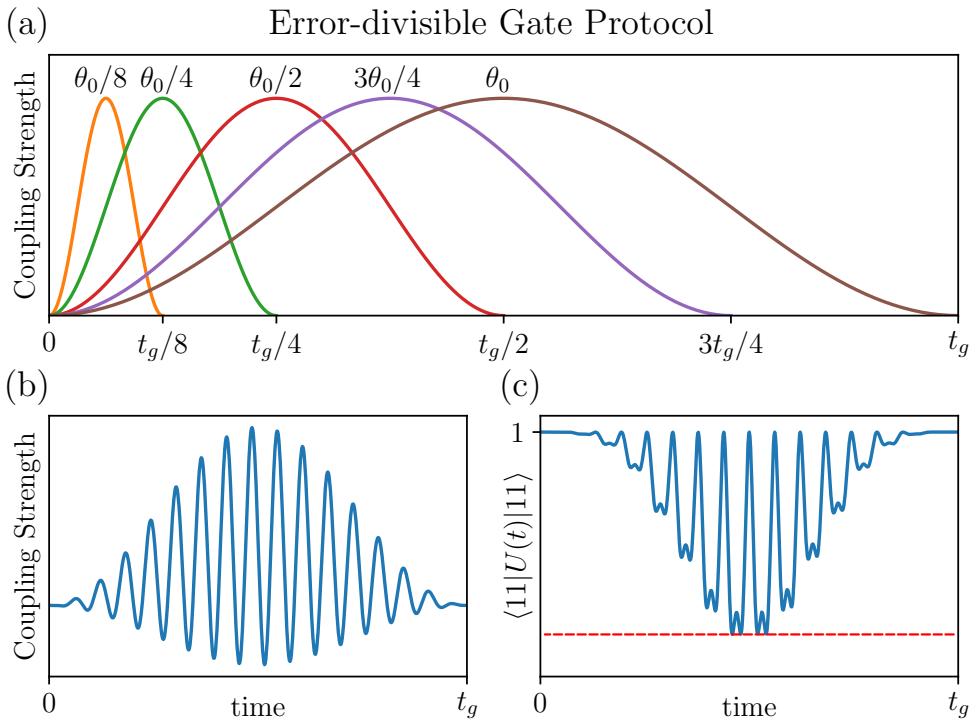

Figure 3.1: Illustration of our proposed error divisibility protocol. (a) Two-qubit rotation θ_0 at gate time t_g, along with fractional rotations θ_0/n at corresponding gate times t_g/n. Note that these waveforms are only meant to demonstrate the idea of error-divisible fractional rotations at fractional gate times, and do not represent actual waveforms (amplitudes and frequencies—shown in (b)—can be different for each partial gate). (b) Example gate strength waveform for achieving error divisibility using a Gaussian gate envelope superimposed with a fast-oscillating counterterm. (c) Corresponding probability of gate $U(t)$ inducing transitions outside of $|11\rangle$ throughout the gate evolution in (b), where $U(t) = T\exp\left(-2\pi i \int_0^{t_g} \Omega(t)\left(|01\rangle\langle 10| + |10\rangle\langle 01|\right) dt\right)$ with coupling strength $\Omega(t)$ like in (b). An ideal exchange operation would preserve unity throughout the gate, but accounting for nonlinear leakage states, we see off-resonant transitions outside of $|11\rangle$, creating these dips in (c), the maximum indicated by the red-dashed. In typical operating regimes, the coupling strength in (b) is on the order of tens of MHz, $t_g \approx 30$ ns, and the maximum dip from unity—which varies by the target rotation—can be $< 10^{-2}$ for appropriate parameter choices.

3.2 Principles of implementation

Consider two transmons with energies ω_1 and ω_2 with nonlinearity $-\delta$, coupled by the term $g(t)\left(a_1 + a_1^\dagger\right)\left(a_2 + a_2^\dagger\right)$. With appropriate choices of $g(t)$, we can resonantly drive a photon exchange between the two qubits. Choosing $g(t) = g_0\Omega(t)\cos[2\pi(\omega_1 - \omega_2)]$ gives us the rotating frame Hamiltonian (Appendix D.1)

$$\begin{aligned} H =& \frac{\delta}{2}\left(a_1^\dagger a_1^\dagger a_1 a_1 + a_2^\dagger a_2^\dagger a_2 a_2\right) \\ & - \Omega(t) g_0\left(a_1^\dagger a_2 + a_1 a_2^\dagger\right). \end{aligned} \tag{3.1}$$

By going to second order in perturbation theory and eliminating the second excited energy state of the transmons, the qubit Hamiltonian becomes

$$\begin{aligned} H \simeq & -\Omega(t) g_0\left(\sigma_1^+\sigma_2^- + \sigma_1^-\sigma_2^+\right) \\ & + \frac{\Omega(t)^2 g_0^2}{\delta}(1+\sigma_1^z)(1+\sigma_2^z), \end{aligned} \tag{3.2}$$

where we can see an effective dispersive shift term that applies a $\sigma_1^z\sigma_2^z$ term concurrently with the exchange Hamiltonian, $H = H_{\text{ex}} + H_{ZZ}$. To eliminate this dispersive shift, we let $\Omega(t)$ take on a shape like that of figure 3.1(b),

$$\Omega(t) = \Omega_0(t)\left[1 + \alpha\sin(2\pi f t)\right], \tag{3.3}$$

where $\Omega_0(t)$ is a slow-evolving gate envelope, and the fast-oscillating counterterm is determined by a frequency f, and α determines whether the waveform is positive valued—a condition required by some hardware implementations [74]. Supposing that the slow-evolving envelope in equation 3.3 is red-detuned from the off-resonant transition causing phase accumulation, the fast-oscillating term adds a corresponding dispersive shift blue-detuned term with opposite sign, and can cancel it out. Examples of engineering these dispersive shifts from off-resonant processes is given in [75]. This is a similar approach to what was discovered in [19], where an oscillatory offset proportional to the nonlinearity was found to suppress population of the leakage states.

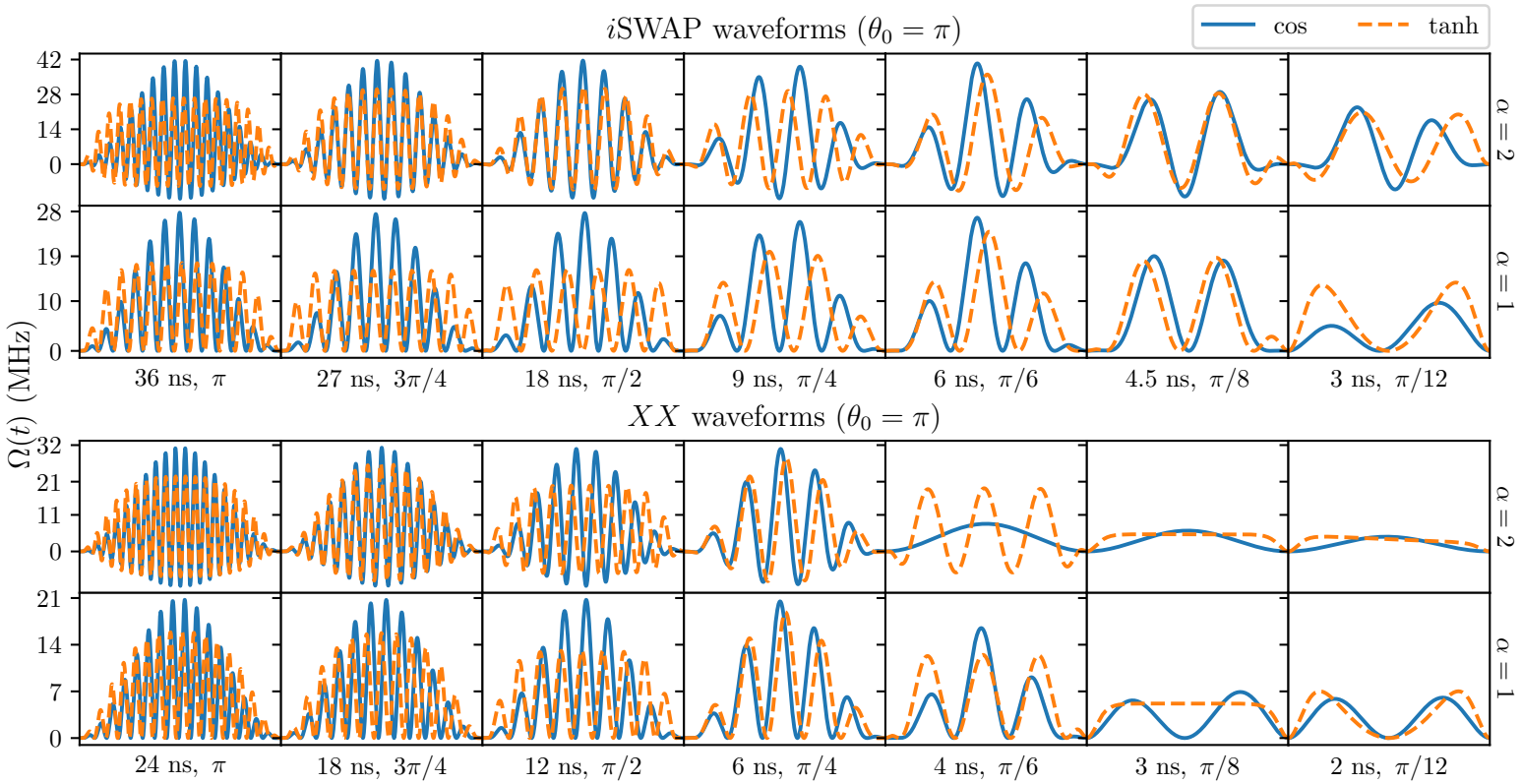

Figure 3.2: Waveforms given by equation 3.4 for different rotations of iSWAP (top) and XX (bottom) gates. Waveforms for equation 3.4a and equation 3.4b are labelled simply as "cos" and "tanh", respectively, in the legend. The first row of both iSWAP and XX waveforms use $\alpha = 2$ in equation 3.3, while the bottom rows use $\alpha = 1$ to restrict the waveforms' positivity. The full rotation waveforms are on the far left, subsequent plots reduce the target rotation and corresponding gate time by the fractional series $\{3/4,\ 1/2,\ 1/4,\ 1/6,\ 1/8,\ 1/12\}$.

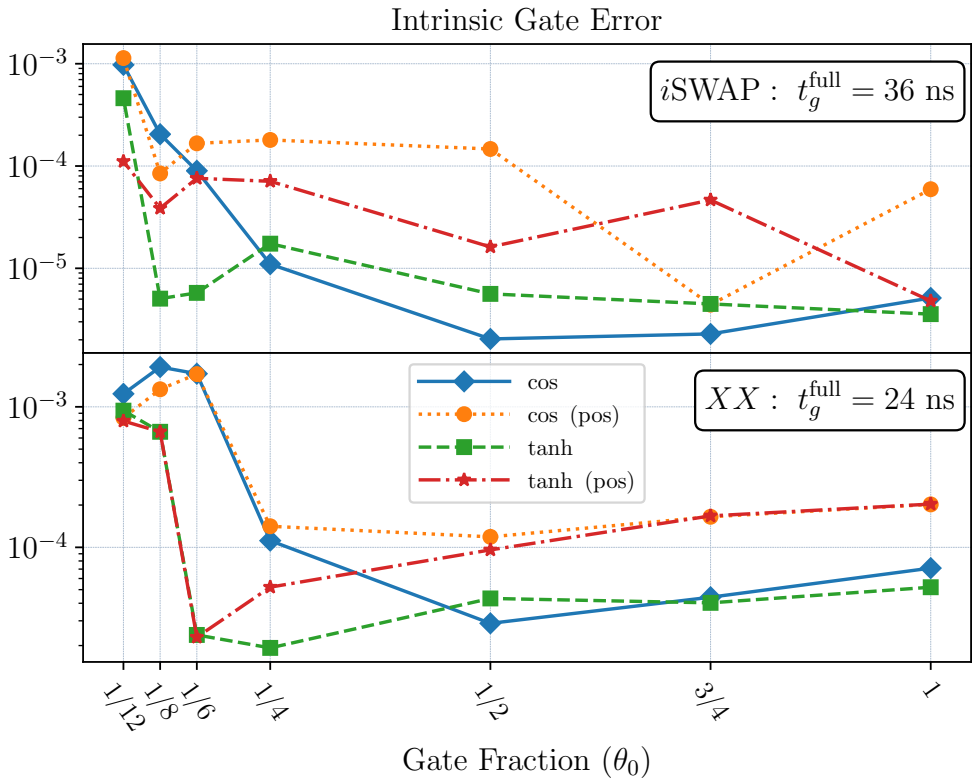

Figure 3.3: Intrinsic gate error results for fractional gate rotations for iSWAP (top, 36 ns gate for full π rotation) and XX (bottom, 24 ns for full π rotation) gates using both positive-definite (pos) and freely oscillating gate envelopes equation 3.4a (cos) and equation 3.4b (tanh). For fractional iSWAP gates, we achieve a gate error $< 10^{-4}$ down to $1/8^{\text{th}}$ of a gate using tanh envelopes and $1/6^{\text{th}}$ for XX gates.

The examples presented here focus on exploring different wave envelopes $\Omega_0(t)$ for two different, candidate gate systems—iSWAP$(\theta) = \exp\left[i\theta/2\left(\sigma_1^+\sigma_2^- + \sigma_1^-\sigma_2^+\right)\right]$ and $XCX(\theta) = \exp[i\theta/4\,(1+\sigma_1^x)\,(1+\sigma_2^x)]$, where a full gate rotation θ_0 (like the illustration from figure 3.1) would be $\theta_0 = \pi$. The $XCX(\theta)$ gate set—the x-basis version of CPHASE(θ)—is chosen as it is easier to engineer than CPHASE. Also note that XCX reduces to single-qubit operations and one two-qubit XX operation, which along with iSWAP, becomes the focus of the following example waveforms.

3.2.1 Example Waveforms

We propose some example waveforms with the characteristic fast-oscillating counterterm, as shown in figure 3.1(b). We focus on two different options for the

slow-evolving envelope $\Omega_0(t)$ in equation 3.3:

$$\Omega_0(t) = \frac{A}{2}\left[1 - \cos\left(2\pi\frac{t}{t_g}\right)\right], \text{ and} \tag{3.4a}$$

$$\begin{aligned}\Omega_0(t) =& A\Bigg[\tanh\left(\gamma\frac{t}{t_g}\right) \\ &- \tanh\left(\gamma\left[\frac{t}{t_g} - 1\right]\right) - \tanh\gamma\Bigg]^2.\end{aligned} \tag{3.4b}$$

For both equation 3.4a and equation 3.4b, the fast-oscillating part takes the form from equation 3.3, where we numerically tune the frequency f for different target rotations, and choose $\alpha = 1$ for a positive-definite waveform, and $\alpha = 2$ for waveforms without such restrictions. A and γ are also numerically tuned for each target rotation, leaving only 2 parameters to tune for equation 3.4a waveforms, and three for equation 3.4b. These are shown in figure 3.2 for iSWAP and XX gates, using nonlinearity $\delta = 300$ MHz. Per the protocol laid out in figure 3.1, we first find a waveform for a full two-qubit rotation with a minimum gate time t_g while maintaining an acceptably low intrinsic error rate. We can then find waveforms for fractional rotations with corresponding fractional gate times, tuning the parameters A, γ, and f to maintain a low gate error. The results presented here do not consider decoherence and only account for leakage.

Error rate results for these fractional gates are shown in figure 3.3. Each fraction in the horizontal axis corresponds to the fraction of the gate operation at a fractional gate time. So for example, a full iSWAP gate corresponds to a full two-qubit π rotation and is done at a gate time $t_g^{\text{full}} = 36$ ns. A fractional 3/4 iSWAP gate would perform a two-qubit $3\pi/4$ rotation at a corresponding gate time $t_g^{3/4} = 27$ ns. The results in figure 3.3 demonstrate the error rates for different fractional gates using the different types of waveforms shown in figure 3.2. We can see that error-divisibility is achieved for both iSWAP and XX gates down to 1/8th and 1/6th, respectively, using the profile equation 3.4b—this profile gives the best results. Considering that the target angle for a full XCX operation is half on an iSWAP, we expect this error-divisible scheme to break down faster for fractional XX operations, where small t_g starts to approach $1/\delta \approx 3$ ns. The limits of this scheme are

evidenced by the noticeable increases in gate error down to 1/12 of a rotation, shown in figure 3.3, where we also point out a general higher gate error using positive-definite waveforms. We also note that intrinsic gate error can be further reduced using higher resolution in pulse-shaping with a fourier series waveform to arbitrary precision. However, this would require an arbitrary number of parameters to calibrate, making this option less-desirable. The waveforms in equation 3.4 provide a simple parameter space to calibrate that matches experimental hardware. The complete set of criteria we have proposed pave a way towards greater depth circuits. Results and waveforms shown in figure 3.2 and figure 3.3 were obtained using unitary dynamics (ignoring energy loss and dephasing), and parameters were found using differential evolution methods [76].

3.3 Hardware implementations

In the current state of superconducting hardware, advances in optimal control methods have mostly eliminated single-qubit gate errors [77–80]. However, multiple-qubit gate errors are still an order of magnitude greater than single-qubit gates [63–68], suffering from a combination of random qubit error during the gate, crosstalk [81–83], and calibration drift over time in systems using tunable architectures [84–86]. This error-divisible scheme intrinsically addresses random qubit error by reducing the duration of the gates in NISQ algorithms requiring smaller two-qubit rotations. This can be reliably done with our proposed scheme provided there are not error-limiting steps. This means gate protocols using tunable qubit energies [87, 88], where coupling is done by bringing them into resonance with each other, cannot be considered for this protocol due to the fixed amount of time necessary for tuning the qubit energies. The presence of fixed amounts of time also eliminates cross-resonance gates [89–92], where there is a minimum duration needed to suppress leakage in the process of driving qubits into higher excited energy states.

This leaves us with qubit architectures with fixed qubit energies [93, 94], in which coupling is achieved by driving a coupler at the appropriate frequencies. These allow the

implementation of the waveforms presented in figure 3.2, creating a path towards error-divisibility. The ability to realize this protocol with any system using a tunable coupler circuit allows for an easy generalization to qubits with large and small nonlinearities. Thus, while the analysis and simulations done in this work assumes a transmon architecture, it is easily realizable for flux qubits [95–97] and fluxoniums [98, 99].

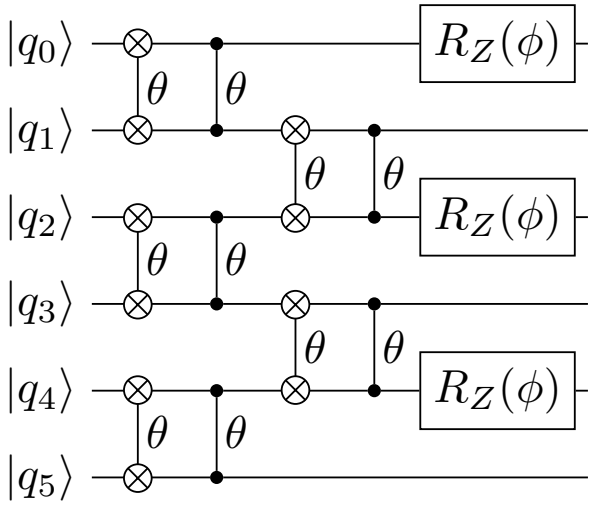

Figure 3.4: Circuit diagram for a single layer of VQE implementing the Hamiltonian equation 3.9 using six qubits. The "θ" labels next to the iSWAP and CPHASE gates denote their partial rotations by angle θ.

3.4 VQE example

To further motivate the use of the error-divisible protocol proposed in this work, we demonstrate the utility of running a variational algorithm with access to error-divisible gates. The goal of the variational quantum eigensolver is to determine the ground state of a problem Hamiltonian. For difficult problem Hamiltonians, determining the ground state can be a big challenge, but we are able to express a state $|\psi\rangle$ as the superposition of the Hamiltonian eigenstates $|E_n\rangle$,

$$|\psi\rangle = \sum_n c_n |E_n\rangle , \tag{3.5}$$

and so we are guaranteed that measuring the expectation value of the energy will give us

$$\langle\psi| H |\psi\rangle = \sum_n |c_n|^2 E_n \geq E_0, \tag{3.6}$$

where E_0 is the exact ground-state energy.

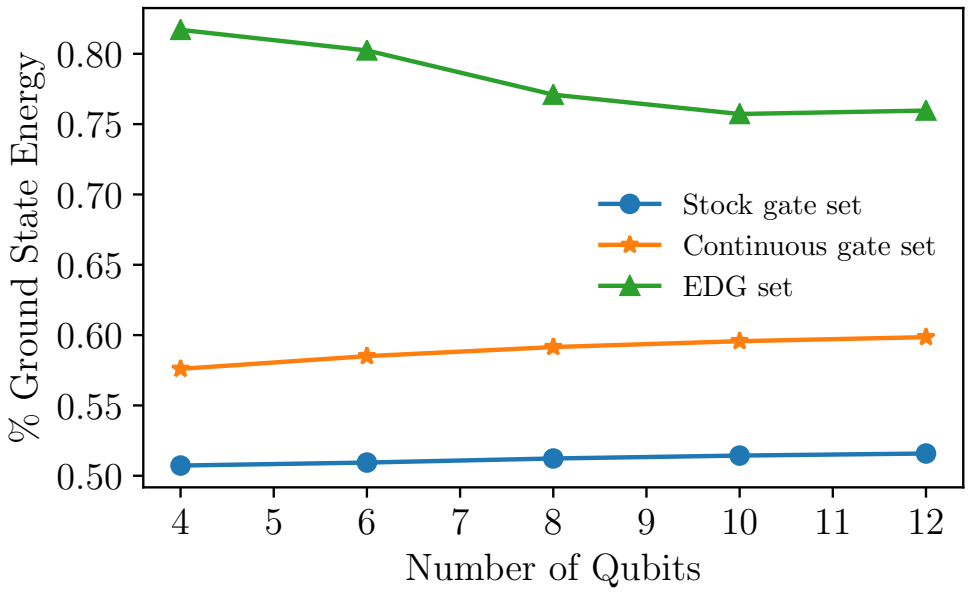

Figure 3.5: Comparisons for VQE percent of ground state results using a stock gate set (blue square), continuous gates (orange star), and the proposed error-divisible gate scheme (green triangle).

Thus by varying parameters for an initial state $|\psi\rangle$, we can continue measuring the expectation value of the energy and try to approach the Hamiltonian ground state. This can become very computationally demanding, and is therefore one of the most commonly studied applications for quantum computers, which could perform the evolution of the state $|\psi\rangle$ much faster than a classical simulation. These variational quantum algorithms are limited by the coherence of the quantum processors, and their performance is measured by how close to the true ground state they are able to get before the system undergoes decoherence. We thus compare the performance of results here and in chapter 5 by the percentage of the ground state that the algorithm is able to achieve.

The example problem we consider is an adiabatic evolution

$$H(t) = \left(1 - \frac{t}{T}\right) H_{\text{pin}} + \frac{t}{T} H_{\text{prob}}, \tag{3.7}$$

where T is the total runtime, H_{pin} is a pinning Hamiltonian with an easily solvable solution, and H_{prob} is a harder problem Hamiltonian whose ground state we are trying to

determine by starting in the ground state of H_{pin} and adiabatically evolving $H(t)$. Approximating with a Trotter decomposition [100]

$$e^{-i\,dt(A+B)} = e^{-i\,dtA}e^{-i\,dtB} + O(dt^2), \tag{3.8}$$

we are able to implement the Hamiltonian as a collection of one- and two-qubit gates on hardware. Letting N be the number of Trotter layers, we set $dt = T/N$.

We choose to find the ground state of an Antiferromagnetic Heisenberg Model (AFM), letting the pinning and problem Hamiltonians in equation 3.7 be

$$H_{\text{pin}} = V \sum_{j \text{ even}} \sigma_j^z \tag{3.9a}$$

$$H_{\text{prob}} = J \sum_{j=0}^{n_q-2} \left(\sigma_j^x \sigma_{j+1}^x + \sigma_j^y \sigma_{j+1}^y + \sigma_j^z \sigma_{j+1}^z\right), \tag{3.9b}$$

where n_q is the number of qubits, and V and J are energy scales, which we set $V = J = 1$ here. The circuit for equation 3.9 is shown in figure 3.4, where the Z rotations correspond to the pinning Hamiltonian equation 3.9a, and the iSWAP(θ) CPHASE(θ) sequence performs the problem Hamiltonian equation 3.9b by the approximation equation 3.8. T and N are optimized after every layer in figure 3.4 using a nonlinear optimization routine [101, 102].

The primary error model considered here is a 1% depolarizing noise error rate for two-qubit gates and 0.1% for single-qubit gates. We compare the performance of this simulated variational algorithm using error-divisible gates, continuous gates [71, 70], and a stock gate set. Results are shown in figure 3.5 with, $\theta = 2J(t/N)\,dt$ and $\phi = 2V(1 - t/T)\,dt$. An implementation of figure 3.4 using a stock gate set would require two two-qubit gates and at least 4 single-qubit gates (Appendix D.2), giving an error rate of at least 2.4% per two-qubit operation in the VQE layer. With access to continuous gates, there would be no need for such decompositions, and thus the two-qubit gate error rate is the 1% we define. Using error-divisible gates, implementing fractional gates with fractional gate times, results in a corresponding fractional error rate, and is thus determined by N. These clear

advantages are demonstrated in simulation as seen in figure 3.5, providing a clear example of the potential benefit in implementing error-divisible gates for near-term quantum computers.

3.5 Conclusions

We have provided a set of criteria for implementing error-divisible two-qubit gates using currently available technology. We introduced the notion of fractional gates for which error-divisibility provides a huge advantage for NISQ algorithms. At the heart of this criteria is the ability to generate a fast-oscillating waveform that can cancel dispersive shift effects. To that end, we explored two sets of wave envelopes superimposed with fast-oscillating terms on two family of gates—iSWAP(θ) and $XX(\theta)$, and found error-divisibility down to 1/6th and 1/8th of a full rotation, respectively. We then further motivated error-divisible gates by showcasing their potential advantage by simulating a variational algorithm for the adiabatic evolution of an antiferromagnetic Heisenberg model problem Hamiltonian.

3.6 Acknowledgements

We would like to thank Eric Jones and Zhijie Tang for useful discussions. This work was supported by the NSF grant (PHY-1653820) and ARO grant No. W911NF-18-1-0125. Simulations for results in section 3.4 were obtained using the QuEST quantum simulator [103]. Both sets of results in sections 3.2.1 and 3.4 were obtained using the Wendian high performance computer at Colorado School of Mines.

CHAPTER 4

SURVEYING THE DETUNINGS PARAMETER SPACE FOR THE VSLQ-STAR

Towards experimentally realizing the Very Small Logical Qubit

Recall from section 1.3.2 that in order to implement the logical manifold for the VSLQ capable of autonomously correcting errors, we need to use clever flux drives that give the effective two-photon pumps and four-photon exchange from the $\cos\phi$ term in the effective Hamiltonian

$$H = -2E_J \cos\phi \sin f(t). \tag{4.1}$$

In principle, with the appropriate choices of $f(t)$, we can isolate the desired terms from expanding the cosine term and getting the desired photon pumps from the $\phi_l\phi_r$ terms. While there is no limiting theory on the implementation of this system, experimental realizations have seen problems with frequency crowding in implementations for the four-photon process. Not only does this approach generate significant flux noise and suffers from an unwanted, always-on ZZ, it also requires a specialized coupler to achieve. These problems called for the need for a different approach that would not necessitate the complexities of a four-photon process. This new protocol is called the VSLQ-Star code, it can be done using a linear coupler and only requires two-photon processes, which are a lot more commonplace, easier to implement, and do not suffer from errors to the same extent as four-photon processes.

4.1 Defining a new codespace

The new protocol defines the codewords as

$$\begin{aligned} |0_L\rangle &= \frac{1}{\sqrt{2}}(|22\rangle - |00\rangle) \\ |1_L\rangle &= \frac{1}{\sqrt{2}}(|20\rangle - |02\rangle), \end{aligned} \tag{4.2}$$

where upon the action of $\tilde{X}_l\tilde{X}_r$ return -1, as opposed to the original codewords in equation1.22, which return $+1$. To get the Hamiltonian that stabilizes these states, we

consider the transmons coupling term $J(t)\phi_l\phi_r$, with

$$\begin{aligned} J(t) =& A\cos\left[(f_{1100}+\nu_0)t\right] + B\cos\left[(f_{1122}+\nu_0)t\right] \\ &+ C\cos\left[(f_{1102}+\nu_1)t\right] + D\cos\left[(f_{1120}+\nu_1)t\right] \end{aligned} \tag{4.3}$$

where f_{abcd} is the difference in energy between states,

$$\begin{aligned} f_{abcd} &= E_{ab} - E_{cd} \\ &= (E_{la} + E_{rb}) - (E_{lc} + E_{rd}), \end{aligned} \tag{4.4}$$

where $E_{l/r,i}$ denotes the energy of the left or right transmon in state i, and the ν_i terms in eqaution 4.3 are detunings. Looking at the subscript labels implies that these are all two-photon processes, which is exactly what we are looking for here, with the $|1_l1_r\rangle \leftrightarrow |0_l0_r\rangle$ and $|1_l1_r\rangle \leftrightarrow |2_l2_r\rangle$ being two-photon blue-sideband terms, and $|1_l1_r\rangle \leftrightarrow |0_l2_r\rangle$ and $|1_l1_r\rangle \leftrightarrow |2_l2_r\rangle$ being two-photon red-sideband terms. The Hamiltonian for this system is

$$H = \sum_{n,m} \left[(E_{ln} + E_{rm})P_{nm}\right] + H_{\text{int}} \tag{4.5}$$

letting $P_{nm} = |n_l m_r\rangle\langle n_l m_r|$, with H_{int} being the transmon-transmon interaction Hamiltonian which we are interested in finding so that it stabilizes the states in equation 4.2. Letting $n = a^\dagger a$, we use the same rotating frame transformation as before in equation 1.18,

$$\begin{aligned} |\psi\rangle &\to U_R(t)\,|\psi\rangle \\ &\to e^{i[(\omega_l - \delta_l/2)n_l + (\omega_r - \delta_r/2)n_r]t}\,|\psi\rangle\,, \end{aligned} \tag{4.6}$$

which gives us the rotating frame Hamiltonian

$$H = \frac{\delta_l}{2}\,|1_l\rangle\langle 1_l| + \frac{\delta_r}{2}\,|1_r\rangle\langle 1_r| + U_R(t)H_{\text{int}}U_R^\dagger(t), \tag{4.7}$$

where we have followed a procedure laid out in appendix D.1 in deriving rotating wave Hamiltonians. We can rewrite equation 4.7 to get

$$H = \frac{\delta_l}{2}(P_{10} + P_{12}) + \frac{\delta_r}{2}(P_{01} + P_{21}) + \frac{1}{2}(\delta_l + \delta_r)P_{11} + U_R(t)H_{\text{int}}U_R^\dagger(t). \tag{4.8}$$

This updated Hamiltonian gives us some intuition to use a second rotating wave transformation, which we define as

$$U_R'(t) = e^{i/2(\delta_l+\delta_r)P_{11}t}. \tag{4.9}$$

giving us

$$H = \frac{\delta_1}{2}(P_{10}+P_{12}) + \frac{\delta_r}{2}(P_{01}+P_{21}) + U_R(t)U_R'(t)H_{\text{int}}U_R'^{\dagger}(t)U_R^{\dagger}(t). \tag{4.10}$$

We let $U_R''(t) = U_R(t)U_R'(t)$, noting that $U_R(t)$ and $U_R'(t)$ commute. Having

$$U_R''(t) = e^{i[(\omega_l-\delta_l/2)n_l+(\omega_r-\delta_r/2)n_r+(\delta_l+\delta_r)/2P_{11}]t}, \tag{4.11}$$

we replace the interaction Hamiltonian in the bosonic number eigenbasis,

$$\begin{aligned} H_{\text{int}} &= J(t)\phi_l\phi_r \\ &\rightarrow J(t)\left(a_l + a_l^{\dagger}\right)\left(a_r + a_r^{\dagger}\right). \end{aligned} \tag{4.12}$$

Here, we have used the relationship

$$\phi = \left(\frac{2E_C}{E_L}\right)^{1/4}\left(a + a^{\dagger}\right), \tag{4.13}$$

with E_C the capacitor energy, and E_L the inductive energy of the transmon's Cooper pair island. These are determined by hardware specification and so we ignore them and set the whole prefactor to 1 since it is not relevant for this analysis. The crucial part is getting the Hamiltonian that stabilizes the states in equation 4.2, for which all we need is to solve for $J(t)U_R''(t)\left(a_l + a_l^{\dagger}\right)\left(a_r + a_r^{\dagger}\right)U_R''^{\dagger}(t)$. Assuming for now that the detunings $\nu_i = 0$ in $J(t)$, we get the effective, rotating wave Hamiltonian

$$\begin{aligned} H^R = W\,(&|11\rangle\langle 00| + |11\rangle\langle 22| + |11\rangle\langle 20| + |11\rangle\langle 02| + \text{H.c.}) \\ &+ \epsilon_1\left[\,|1_l\rangle\langle 1_l|\,(1 - |1_r\rangle\langle 1_r|) + |1_r\rangle\langle 1_r|\,(1 - |1_l\rangle\langle 1_l|)\,\right] \end{aligned} \tag{4.14}$$

where W is the effective energy scale of the primary transmons Hamiltonian that comes as a result of physical hardware parameters and driving frequencies that we forego in this analysis—suffice to say it is tuned with the flux-drives and is treated as a variable

parameter for the results later in this chapter. ϵ_1 is the energy for the single-photon states of the transmons, which in the rotating frame is effectively the same as the transmon nonlinearity δ. Looking at the most trivial eigensystem for the W term in equation 4.14, we see five eigenstates of interest, ignoring normalization:

$$-2W: \; -2\,|11\rangle + |00\rangle + |22\rangle + |02\rangle + |20\rangle \tag{4.15a}$$

$$0: \; |22\rangle - |00\rangle \tag{4.15b}$$

$$|02\rangle - |00\rangle \tag{4.15b}$$

$$|20\rangle - |00\rangle \tag{4.15b}$$

$$+2W: \; 2\,|11\rangle + |00\rangle + |22\rangle + |02\rangle + |20\rangle\,. \tag{4.15c}$$

Also note that any linear combination of zero-energy eigenstates will also be a zero-energy eigenstate. We already see one of the codewords from equation 4.2 at the top of equation 4.15(b), and the other codeword can be obtained from a linear combination of the two bottom states of equation 4.15(b), which gives us the two orthogonal codewords as eigenstates. To complete the a unique set of orthogonal eigenstates with the codewords, we form a third state using a linear combination of all states in equation 4.15, giving us the effective, three zero-energy states

$$|22\rangle - |00\rangle \tag{4.16a}$$

$$|20\rangle - |02\rangle \tag{4.16b}$$

$$|00\rangle + |22\rangle - |20\rangle - |02\rangle\,, \tag{4.16c}$$

where we can finally see that the codewords we defined are stabilized by the Hamiltonian in equation 4.14. However, having the third orthogonal degenerate state creates a problem for error correction. This is because when a photon loss occurs in either of the states $|0_L\rangle$ or $|1_L\rangle$, the error state cannot be uniquely reconstructed to its parent logical state if there is a third degenerate state in resonance with the error-correction mechanism.

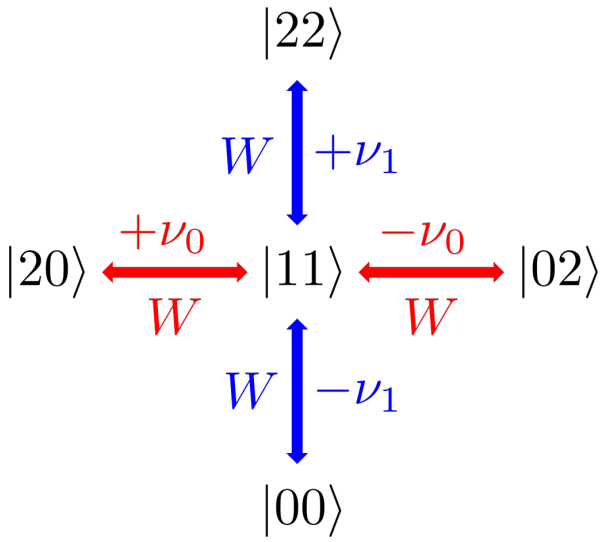

Figure 4.1: Four-point star illustration of the Hamiltonian in equation 4.18. The codewords for this protocol are all stabilized using two-photon processes with the $|11\rangle$ state as a sort of intermediary state to achieve an effective four-photon process. The $|20\rangle - |02\rangle$ codeword is stabilized using red-sideband transmon-transmon couplings detuned by ν_0, while the $|22\rangle - |00\rangle$ codeword is stabilized using blue-sideband transmon-transmon couplings, detuned by ν_1. This helps illustrate the fact that including the detunings for transitions with the $|11\rangle$ state does not actually change the energies of the codewords themselves. This visual mapping motivates the name for this new protocol—the VSLQ-star.

Selective energetics allow a distinction between the parent logical states if the only two degenerate states are $|0_L\rangle$ and $|1_L\rangle$. But otherwise, error correction fails. This is where the detunings in equation 4.3 come in. Letting the detunings $\nu_i \neq 0$ in $J(t)$, and with the appropriate rotating frame transformations

$$\begin{aligned} V_0(t) &= e^{i\nu_0(P_{00}+P_{22}+P_{21}+P_{12})t} \\ V_1(t) &= e^{i\nu_1(P_{02}+P_{20}+P_{01}+P_{10})t}, \end{aligned} \tag{4.17}$$

we can get our final primary transmons Hamiltonian

$$\begin{aligned} H^R_{\text{star}} = W\big(&|11\rangle\langle 00|\, e^{-i\nu_0 t} + |11\rangle\langle 22|\, e^{i\nu_0 t} \\ &+ |11\rangle\langle 20|\, e^{i\nu_1 t} + |11\rangle\langle 02|\, e^{-i\nu_1 t} + \text{H.c.}\big) \\ &+ \epsilon_1\big[\, |1_l\rangle\langle 1_l|\,(1 - |1_r\rangle\langle 1_r|) + |1_r\rangle\langle 1_r|\,(1 - |1_l\rangle\langle 1_l|)\,\big]. \end{aligned} \tag{4.18}$$

These detunings ν_i detune the physical driving terms $|02\rangle \leftrightarrow |11\rangle$ and $|02\rangle \leftrightarrow |11\rangle$ for ν_0, and $|00\rangle \leftrightarrow |11\rangle$ and $|22\rangle \leftrightarrow |11\rangle$ for ν_1, as shown in figure 4.1.

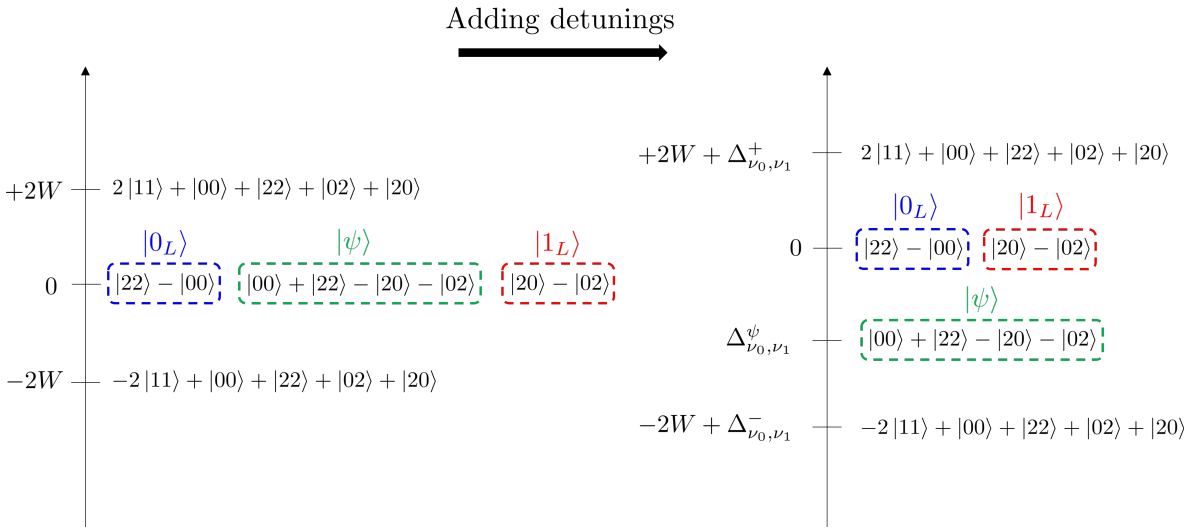

Figure 4.2: Energy illustration for eigenstates of interest for the VSLQ-star Hamiltonian. We see on the left that the codewords for $|0_L\rangle$ (blue box) and $|1_L\rangle$ (red box) are energetically separated from states containing $|11\rangle$ ($\pm 2W$ energies), and are degenerate with a third eigenstate $|\psi\rangle$ (green box). This third degenerate state spoils error correction, so we include detunings ν_0 and ν_1 to break the three-fold degeneracy and separate the $|\psi\rangle$ eigenstate from the codewords. Imperatively, the codewords $|0_L\rangle \equiv |22\rangle - |00\rangle$ and $|1_L\rangle \equiv |20\rangle - |02\rangle$ are still degenerate zero-energy eigenstates, now separated from the third states and still separated from the $|11\rangle$ eigenstates, allowing proper error correction to the appropriate parent logical states in the event of a photon loss. The energy shifts for the $\pm 2W$ eigenstates are simply denoted by $\Delta^{\pm}_{\nu_0,\nu_1}$ and $\Delta^{\psi}_{\nu_0,\nu_1}$ for the $|\psi\rangle$ eigenstate to indicate that they have been shifted by some amounts which are not linearly related to each other. This only illustrates the core idea that the third eigenstate $|\psi\rangle$ is now separated from the codewords, and that the detunings maintain an energy separation between the codewords and the $\pm 2W$ eigenstates.

Crucially, however; ν_0 and ν_1 do not alter the energies of the eigenstates $|0_L\rangle \equiv |22\rangle - |00\rangle$ and $|1_L\rangle \equiv |20\rangle - |02\rangle$ themselves, which remain degenerate, zero-energy eigenstates. The detunings do, however, separate the energy of the third state in equation 4.16, breaking the three-fold degeneracy as shown in figure 4.2. This isolates the other two degenerate codeword eigenstates, permitting the error correction process to correctly transition back to its parent logical state. This process is exactly the same as the original VSLQ protocol, in which an off-resonant blue-sideband drive between the transmon and a lossy resonator "refills" any lost photons in the transmon while exciting the resonator.

4.2 Exploring the detuning space

We require that the detunings are different so we separate the third degenerate eigenstate and have a well defined qubit space using the states in equation 4.2, illustrated in figure 4.2. However, understanding the complex parameter space introduced by including the detunings is no easy task. Likewise, gaining a physical intuition of how this process works is non-trivial after all the rotating frame transformations required to get our system Hamiltonian equation 4.18. We could take the time to design a nonlinear optimization algorithm to search for the best choice of detunings, as well as the best choice for parameters $W, \delta,$ and Ω. Indeed, this is what we have done in section 2.4.2, where we compare the results of using the pulsed-reset scheme (which is the focus of chapter 1) to those of using fixed coupling rate Ω and resonator loss rate Γ_R. However, the choice of parameters ultimately faces hardware limitations, and what gives best results in simulation might not ultimately be realizable. This is something that we saw with the error-divisible gate scheme from chapter 3, where implementing the waveforms for the really small gates became infeasible with the physical implementation of the coupling coefficients. Thus, for now the most prudent exploration that would provide immediately useful results is a scan of the two detunings ν_0 and ν_1, to find how we can best achieve improvements in the logical states' lifetimes, as well as gain insight into our understanding of the detuning mechanism. All of the results in this section assume a resonator loss rate $\Gamma_R = 5\ \mu s^{-1}$.

This first set of results assumes that the nonlinearity in the transmons are equal, and are the same as the resonator energies ($\delta_l = \delta_r = \omega_{Sl} = \omega_{Sr} = 100MHz$), where ω_{Si} denotes "shadow" left or right, using terminology from [4]. Thus, in the rotating frame, we are considering the energy of the first excited state in the transmons, and the energy of the resonators, to all be the same for this section. All sets of detunings scans assume a transmon lifetime $T_1 = 15\ \mu s$ for no reason other than it is a very realistic lifetime that is easily achievable with hardware in transmon architectures.

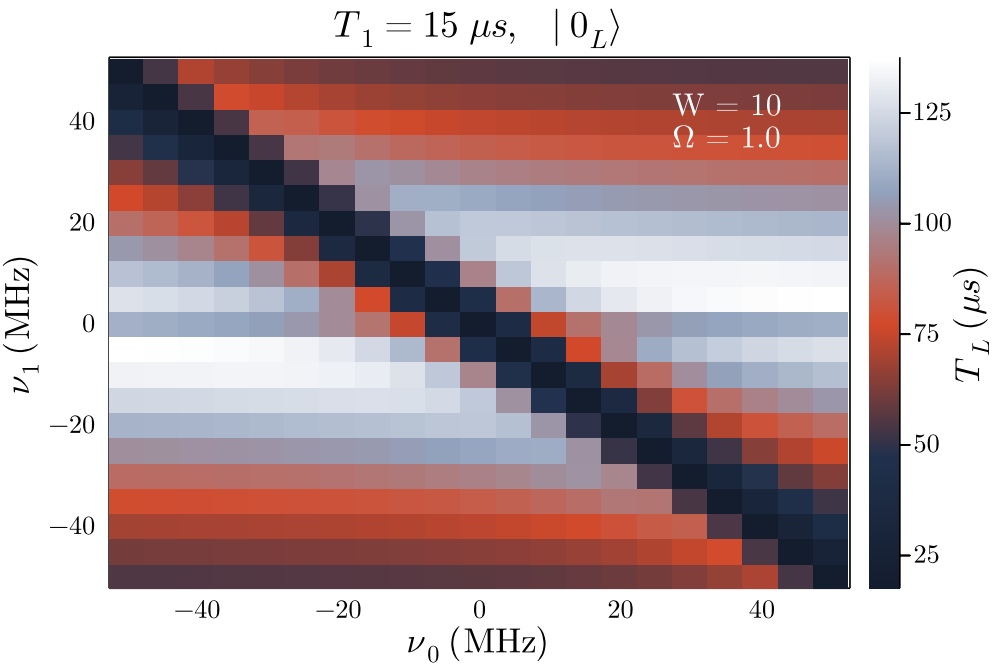

Figure 4.3: Detunings space for $|0_L\rangle$. Note the preference for $\nu_0 \neq -\nu_1$, as well as a strong preference for $\nu_1 \approx 0$ with arbitrary ν_0.

4.2.1 Same transmon and resonator energies

The results in this section look at the detunings space using different combinations of $W = 5, 10$ MHz, and $\Omega = 0.5, 1.0$ MHz. we begin by looking at what the detunings space for $|0_L\rangle$ and $|1_L\rangle$ look like, shown in figures 4.3 and 4.4. Recall from the description of the new VSLQ-star protocol in section 4.1, we specify the need for added detunings ν_0 and ν_1 to break the three-fold degeneracy of the transmons Hamiltonian (equation 4.18) eigenstates (equation 4.16). This is what allows us to separate the VSLQ-star codewords in equation 4.2 and use them as logical qubit states. Achieving this required that $\nu_0 \neq \nu_1 \neq 0$, and that is something we see very clearly in figures 4.5 through 4.8.

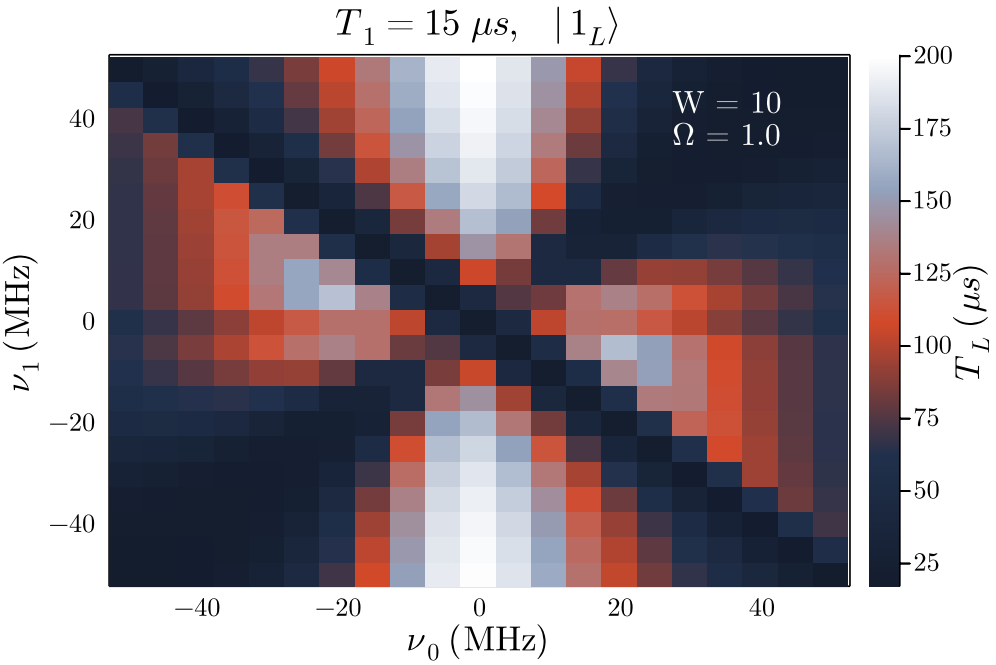

Figure 4.4: Detunings space for $|1_L\rangle$. While still seeing the preference $\nu_0 \neq -\nu_1$, we also now see $\nu_0 \neq \nu_1$. Contrary to what is observed in figure 4.3, there is an almost near opposite preference for $\nu_0 = 0$ and arbitrary ν_1. This is consistent to what is expected from the applications of ν_0 and ν_1 to the different two-photon processes.

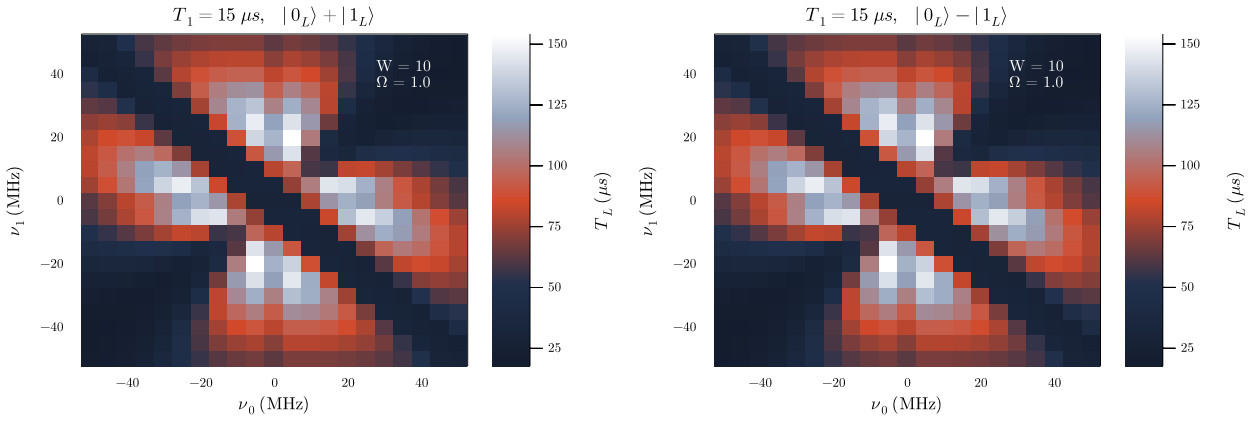

Figure 4.5: Detunings space for $|+_L\rangle = |0_l\rangle + |1_L\rangle$ (left), and $|-_L\rangle = |0_L\rangle - |1_L\rangle$ (right). Note that they are identical spaces (with the simulated resolution). The preference for $\nu_0 \neq \pm\nu_1$ is consistent with the analysis in section 4.1, and results are effectively the same as averaging the results from figures 4.3 and 4.4.

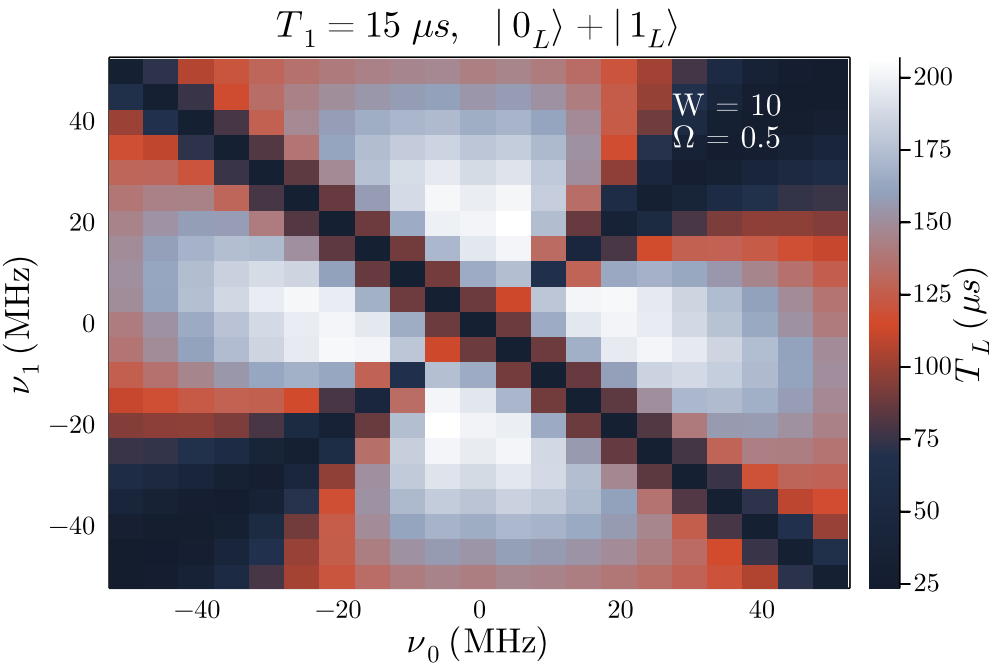

Figure 4.6: Looking at a different choice of coupling strength Ω, we see a more generous choice of detunings to achieve a big improvement in the logical lifetimes for $|+_L\rangle$.

But note, however, that in figure 4.3, we only see $\nu_0 \neq -\nu_1$, but generally $\nu_0 \neq \nu_1$ is not forbidden. Considering that, as shown in figure 4.1, the detunings are meant to shift the energies between the $|11\rangle$ state for either $|0_L\rangle$ *or* $|1_L\rangle$, it makes sense that when only looking at the detunings space for one of the codewords, we only see improvements along one general axis. The same can be seen in figure 4.4, where we look at the detunings space for $|1_L\rangle$. Given that these two give seemingly contradicting choices of detunings if we're wanting a choice that gives us the best improvement in logical state lifetimes, the obvious solution is to find the set of detunings that give the best *averaged* lifetime between $|0_L\rangle$ and $|1_L\rangle$. This is why for the rest of the results, we look at the detunings space for the lifetimes of the codewords in the logical x-basis. Figure 4.5(left) shows this for the state $|+_L\rangle = |0_L\rangle + |1_L\rangle$, and 4.5(right) shows this for the state $|-_L\rangle = |0_L\rangle - |1_L\rangle$, with the two being identical to the bare eye. Since this gives us the best idea of what choice of detunings gives us the best *overall* performance for the logical codewords, the results presented from this point forward only look at lifetimes for the state $|+_L\rangle$.

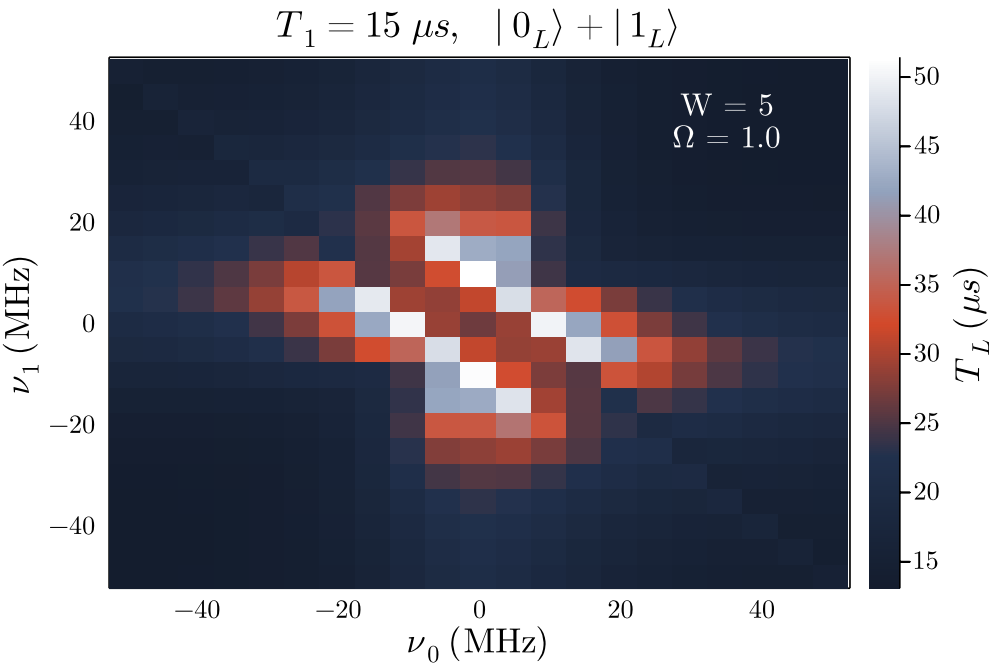

Figure 4.7: Using a smaller energy scale W, there is a very noticeable performance hit to the $|+_L\rangle$ logical lifetime.

Note that the results for this "aggregate" state show a very clear $\nu_0 \neq \pm\nu_1$ condition, while also supporting the analysis in section 4.1 that we only require either ν_0 or ν_1 to be non-zero, but not necessarily both. For these first two sets of results, $W = 10$ MHz and $\Omega = 1.0$ MHz are chosen semi-arbitrarily as easy parameters that could be physically realized, and could give an improvement. But as we shall see later in section 4.2.2, other physical constraints may dictate different choices for these parameters. As mentioned in the beginning of this section, ultimately we can ask a black box optimizer to give us the best set of parameters under certain constraints and call it a wrap. However, that would give us no intuition into the robustness and tolerance of different parameter choices. In other words, we are interested in finding out how changes in W and Ω affect the choices of detunings and if that introduces any further limitations. So continuing our assumption that, in the rotating frame, the transmons and resonators have the same energy for single-excited states, we look at lowering the coupling strength down to $\Omega = 0.5$ MHz in figure 4.6. We see that the best lifetimes here show a significant improvement over using $\Omega = 1$ MHz, shown in figure 4.5. Not only that, but there is a more generous insensitivity

to variations in both ν_0 and ν_1. This improvement using a weaker coupling strength Ω is encouraging since generally, stronger drives can create issues such as crosstalk and frequency crowding. This helps further motivate using smaller W.

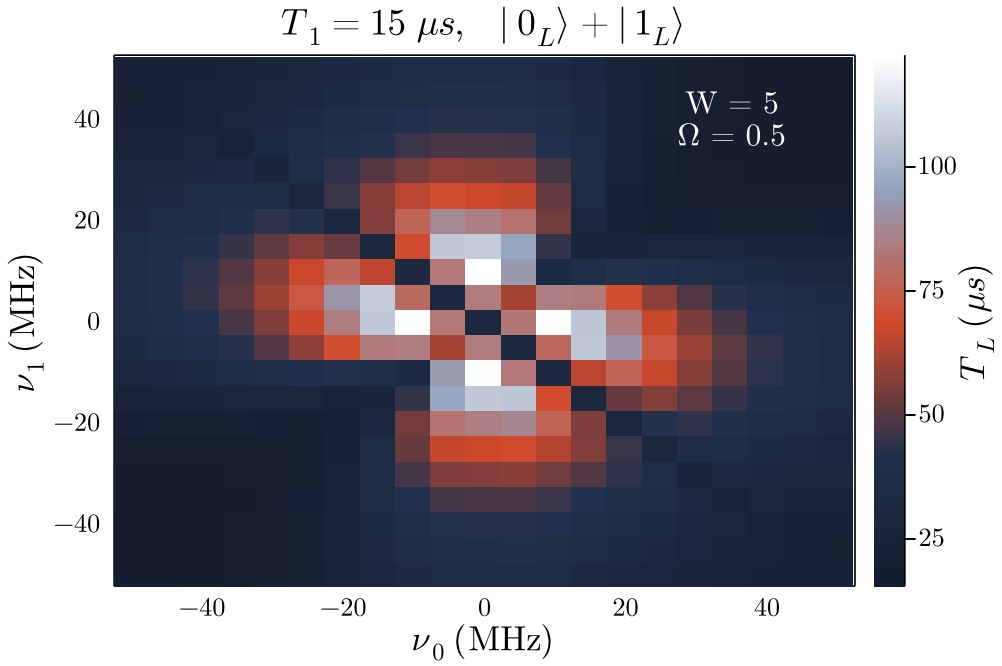

Figure 4.8: Using a smaller Ω for $W = 5$ MHz gives a very noticeable improvement. While these lifetimes are still shorter of the ones observed in figures 4.5 and 4.6, it is a very dramatic improvement over the results in figure 4.7 (drawing attention to the color scale).

Results using $W = 5$ MHz, and $\Omega = 1$ MHz are shown in figure 4.7, where we see a massive performance hit, with a logical lifetime capping out at $\approx 50\ \mu s$, compared to the $\approx 150\ \mu s$ using $w = 10$, while also not giving a lot of room in the choice of detunings. Lowering the coupling strength to $\Omega = 0.5$ MHz in figure 4.8, we see a generous improvement over the lifetimes in figure 4.7. Just like the results using $W = 10$ MHz, we again see an advantage using a weaker coupling strength Ω. While the lifetimes using $W = 5$ MHz and $\Omega = 0.5$ MHz are about half as good as the lifetimes using $W = 10$ MHz and $\Omega = 0.5$ MHz, this set of results presented in figure 4.8 are particularly exciting because they show a dramatic improvement over the base transmon lifetimes using weaker, and thus more experimentally feasible, drives. Lastly, we use an even smaller coupling strength $\Omega = 0.2$ MHz to see if this trend of using weaker signals gives us better logical

lifetimes, shown in figure 4.9. Ultimately, we see that this is not the case, and we see a lower performance in the logical lifetimes over using $\Omega = 1$ MHz in figure 4.7, though a more generous insensitivity to the choice of detunings. This preliminary analysis suggests that all these different sets of driving strengths can give a logical lifetime improvement, but using more intermediate strength transmon-resonator coupling gives the more generous improvement.

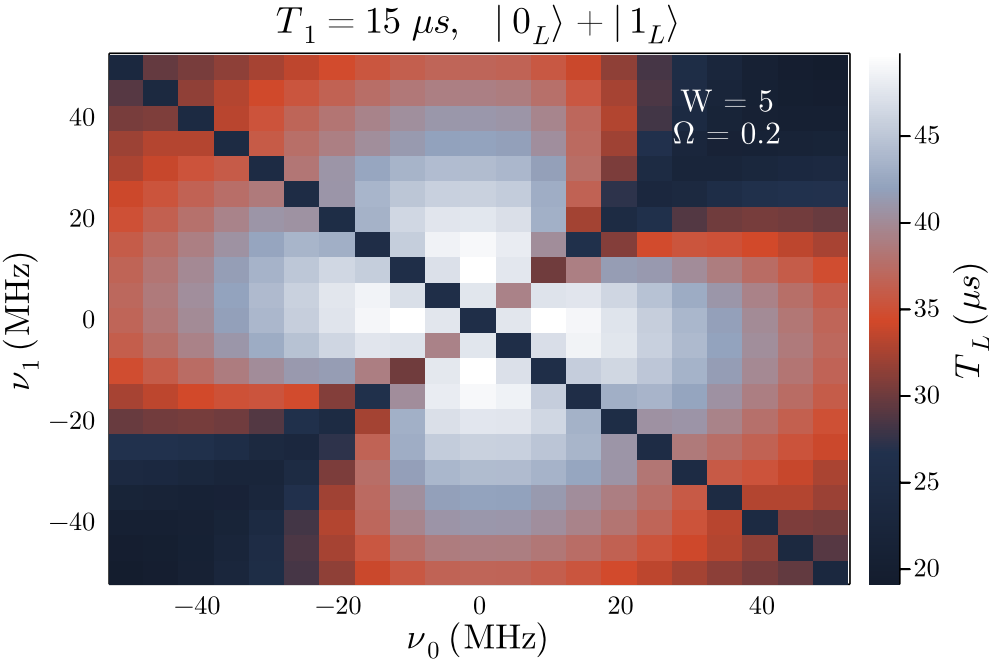

Figure 4.9: One last check using an even smaller drive for the coupling strength Ω while maintaining a primary transmons drive $W = 5$ MHz. This gains the benefit of less sensitivity to the detunings, but the logical lifetime improvement is not quite as it is in figure 4.7.

4.2.2 Different transmon and resonator energies

Having established some intuition as to how the choice of drives affects the preference for detunings, we now repeat this procedure using transmon nonlinearities from actual hardware that is being developed by collaborators to experimentally demonstrate stabilization of the logical manifold. Here we let $\delta_l = \omega_{Sl} = 170$ MHz, and $\delta_r = \omega_{Sr} = 265$ MHz, so that we have different energies between the left and right subsystems, but the resonator energies are the same as their corresponding transmons. Beginning with the

lowest drives that are explored here, we look at the detunings for $W = 2$ and $\Omega = 0.2$ MHz in figure 4.10. We still see the hallmarks of error correction, in which the lifetime of the logical manifold is extended beyond the lifetime of the constituent transmon lifetimes, but there is no observed dramatic improvement at this driving point. Looking at a stronger transmon-resonator coupling $\Omega = 0.5$ MHz in figure 4.11, there is no meaningful improvement over using $\Omega = 0.2$ MHz, and we do see a strong preference for $\nu_0 \neq \pm\nu_1$. The same lack of improvement is seen when using an even larger coupling strength $\Omega = 1.0$ MHz in figure 4.12. In fact, we see a pretty dramatic performance hit compared to figures 4.10 and 4.11. Moreover, we see that this detunings protocol becomes obsolete at this driving point, since figure 4.12 shows that the preferred detunings are $\nu_0 = \nu_1 = 0$, though still giving a marginal prolonging of the logical lifetime over the single transmon lifetime. We note that the rest of the detuning space in dark gives a logical lifetime that is simply the single transmon lifetime.

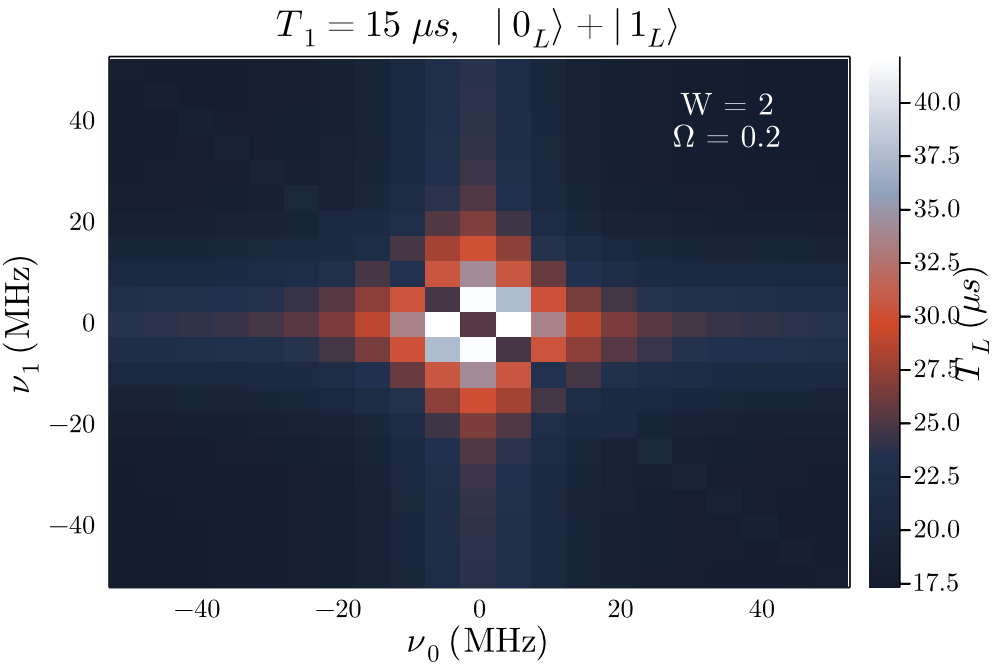

Figure 4.10: Looking at the detunings space using weak drives. Logical state lifetimes are longer than the constituent transmon lifetimes, and are somewhat consistent with the lifetimes observed using weak drives in section 4.2.1.

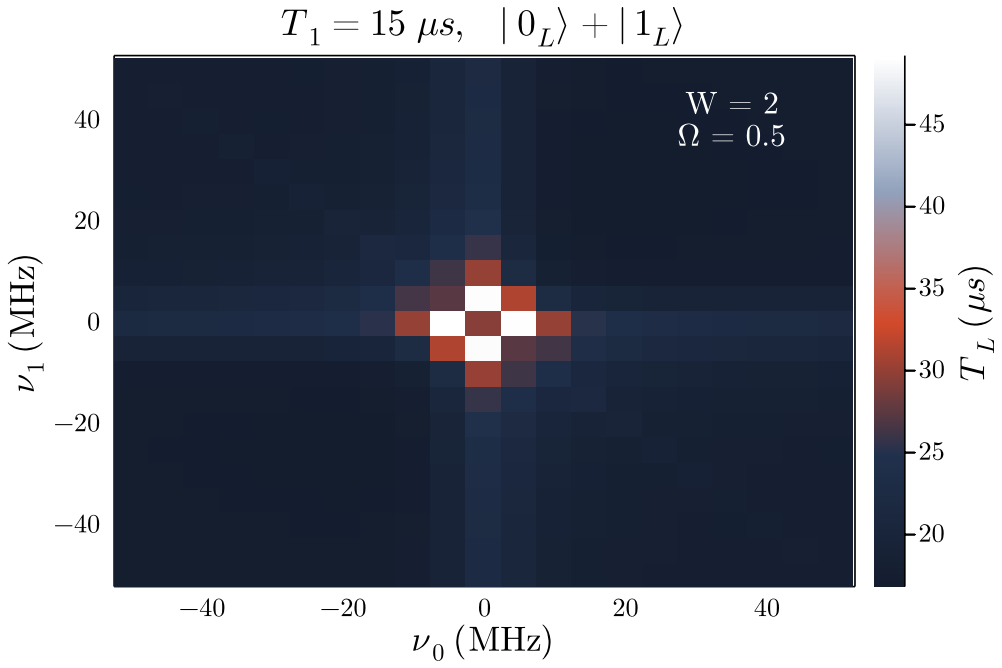

Figure 4.11: Increasing the transmon-resonator coupling strength to $\Omega = 0.5$ MHz. There isn't a significantly observed increase in logical lifetime performance compared to figure 4.10.

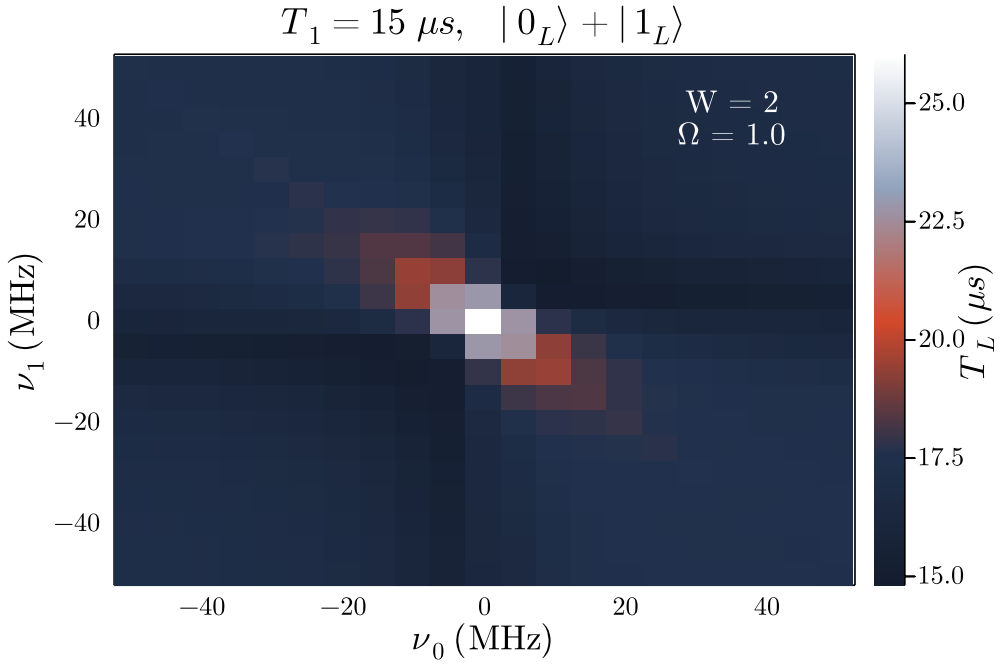

Figure 4.12: Increasing the transmon-resonator coupling further to $\Omega = 1.0$ MHz shows a very significant performance hit to the logical lifetimes compared to figures 4.10 and 4.11. Further, the preferred detunings here are $\nu_0 = \nu_1 = 0$, making this protocol basically insufficient at this choice of drives.

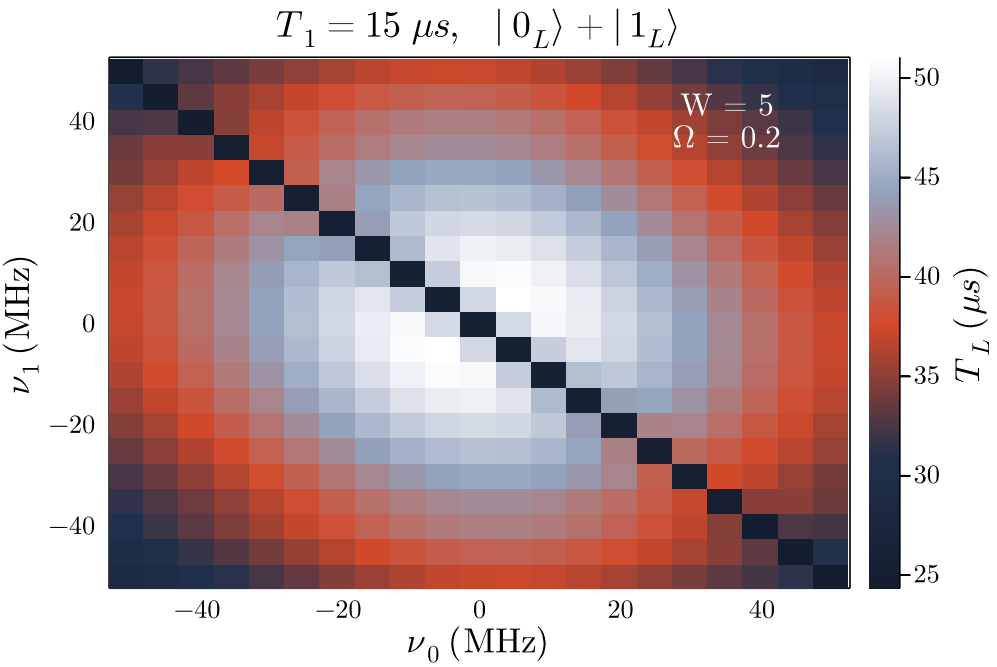

Figure 4.13: Detunings space using a stronger main drive W with weak coupling drive. Logical state lifetimes are consistent with the lifetimes observed using a weaker main drive $W = 2$ MHz.

The last set of detunings scans presented here are for $W = 5$ MHz. As seen in the previous section (4.2.1) when using the same energies, we generally saw the best logical lifetimes when using the larger $W = 10$ MHz. However, using hardware-specified transmon nonlinearities, we are interested here in finding detunings that show a significant advantage in logical lifetimes for easily realizable experimental parameters. As mentioned above, using stronger drives can induce a set of issues in hardware. Thus the remaining focus for results here are using the relatively weaker point $W = 5$ MHz. Figure 4.13 shows this with coupling strength $\Omega = 0.2$ MHz, where just like before we only see a modest improvement.

Ramping up to $\Omega = 0.5$ MHz, however, we see a very dramatic improvement similar to that of figure 4.8, to a logical lifetime $T_L > 150\mu s$. And lastly, looking at $\Omega = 1.0$ MHz in figure 4.15, we again see a good improvement, but not as generous as in figure 4.14. These are very encouraging results since it suggests that we can achieve impressive logical lifetime improvements using relatively weak drives, hopefully making an impressive

demonstration of AQEC more experimentally feasible.

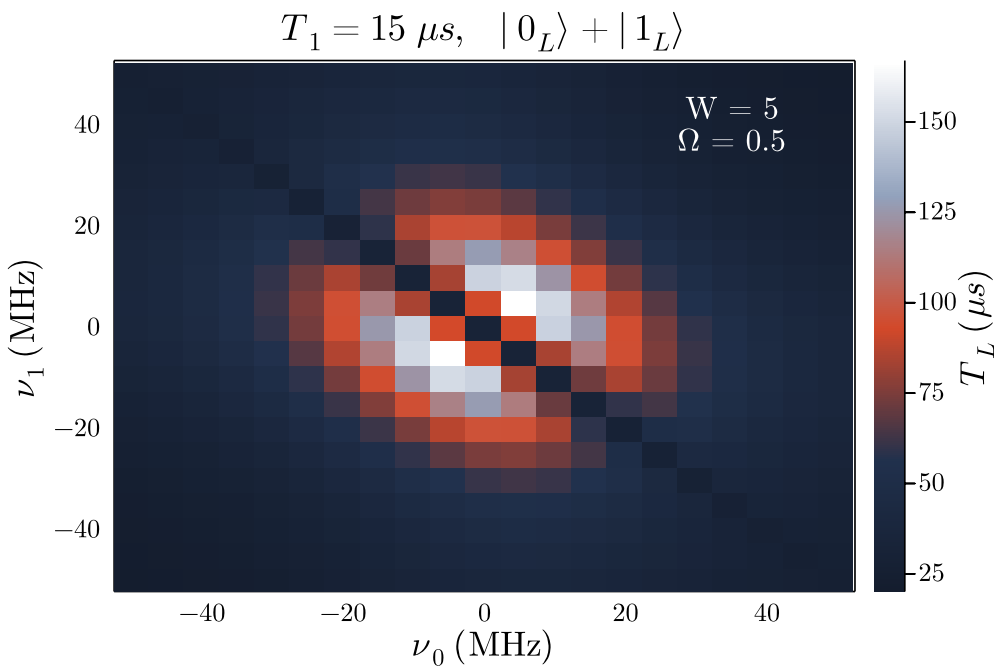

Figure 4.14: Increasing the transmon-resonator coupling strength to $\Omega = 0.5$ MHz. There is a much more generous improvement in the logical lifetime over the single transmon lifetime, as well as the logical lifetimes in figure 4.13.

A couple of things to note for this last set of results. The choice of driving terms that gives the most easily accessible logical lifetime improvements may not be the most insensitive set of detunings, such as those in figure 4.8. This is not necessarily a problem, and given that results that are more insensitive such as figure 4.9 do not how the same level of lifetime improvement, it is worthwhile to sacrifice detunings sensitivity. However, given variations in experimental driving terms, lifetime sensitivity to fluctuations in detunings is something to make note of. Fortunately, all the results presented in this chapter use a fairly low resolution in the detunings space, and we can be confident these results provide a promising path forward. Additionally, note that for the set of results in section 4.2.2 where the transmon nonlinearities are different, while we still see the characteristic preference for $\nu_0 \neq -\nu_1$, we no longer see $\nu_0 \neq +\nu_1$. Given that the only thing that changed is the fact that $\delta_l \neq \delta_r$, we can attribute this difference in nonlinearities contributing to the breaking of the eigenstate degeneracy discussed in

section 4.1, while keeping in mind that the detunings also shift the energies of the $|11\rangle$ eigenstates in unspecified ways. And so we can stipulate how $\nu_0 = -\nu_1$ may be contributing to the shifting of these different eigenstates. However, it suffices to present results showing how different choices of driving terms can give preference to choices in detunings that can provide the easiest path towards realizing passive error correction.

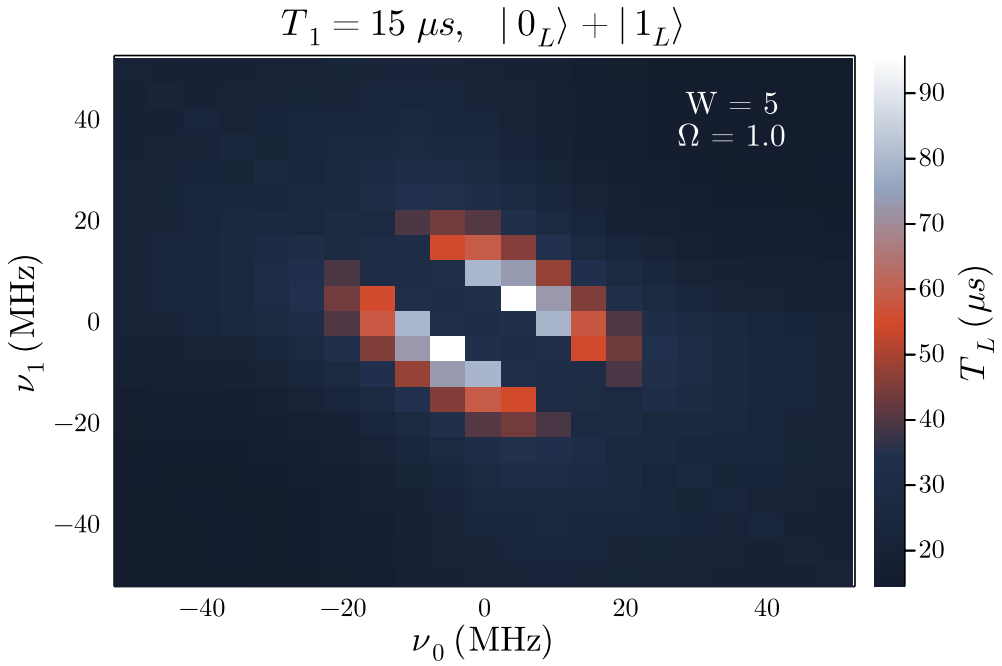

Figure 4.15: Increasing the transmon-resonator coupling further to $\Omega = 1.0$ MHz shows a slight performance hit to the logical lifetimes compared to figure 4.14, but a handsome improvement over lifetimes in figure 4.13.

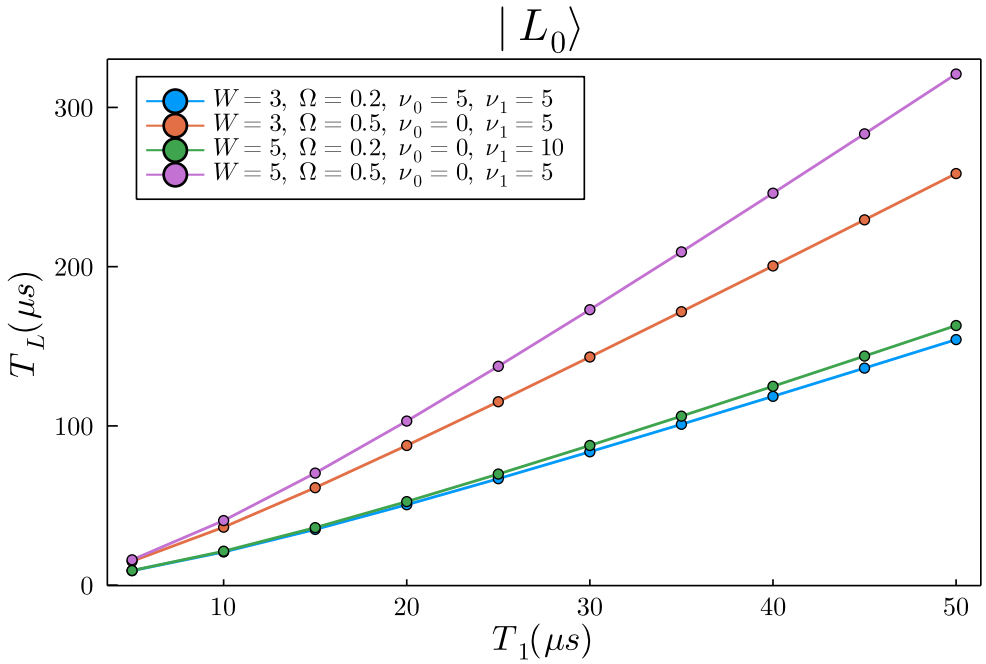

Figure 4.16: Logical lifetimes for $|0_L\rangle$ at different choices of drives and detunings. Detunings were chosen based on results in section 4.2.2.

4.3 Logical lifetime results

Using some of the results presented in section 4.2, we look at how these choices for detunings can provide the easiest way towards demonstrating stabilization of the logical codewords. In the same spirit as section 4.2.1, we focus on using relatively weaker drives. While stronger ones may provide a bigger advantage in logical state lifetimes, the immediate goal is to demonstrate *an* advantage, and doing so is generally easier using weaker drives. Results in figure 4.16 look at the logical lifetimes for $|0_l\rangle$ for different single qubit T_1, where we again use the different transmon energies from section 4.2.2. The key takeaway here is that while choosing $W = 5$ and $\Omega = 0.5$ gives the absolute best results among this set of drives, the more immediately dramatic improvement occurs simply by the choice of $\Omega = 0.5$, where we see a very handsome performance of logical lifetimes even for $W = 3$. This freedom in finding an AQEC advantage at lower drives is particularly useful for experimental realizations. These results are consistent for $|1_L\rangle$ in figure 4.17 and for $|+L\rangle$ in figure 4.18.

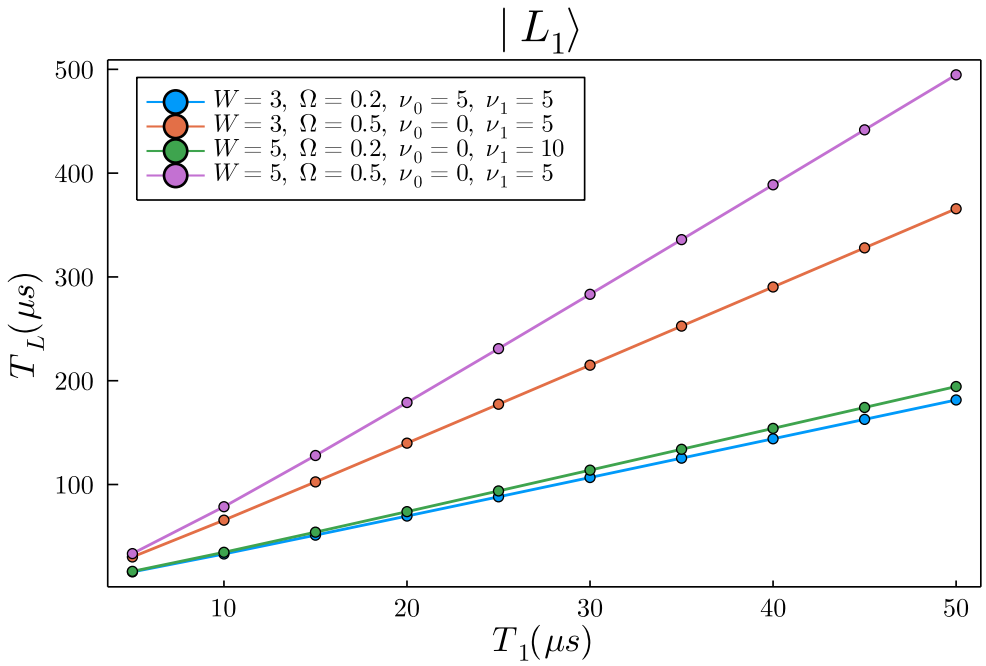

Figure 4.17: Logical lifetimes for $|1_L\rangle$, where we see the same level of improvement as in figure 4.16.

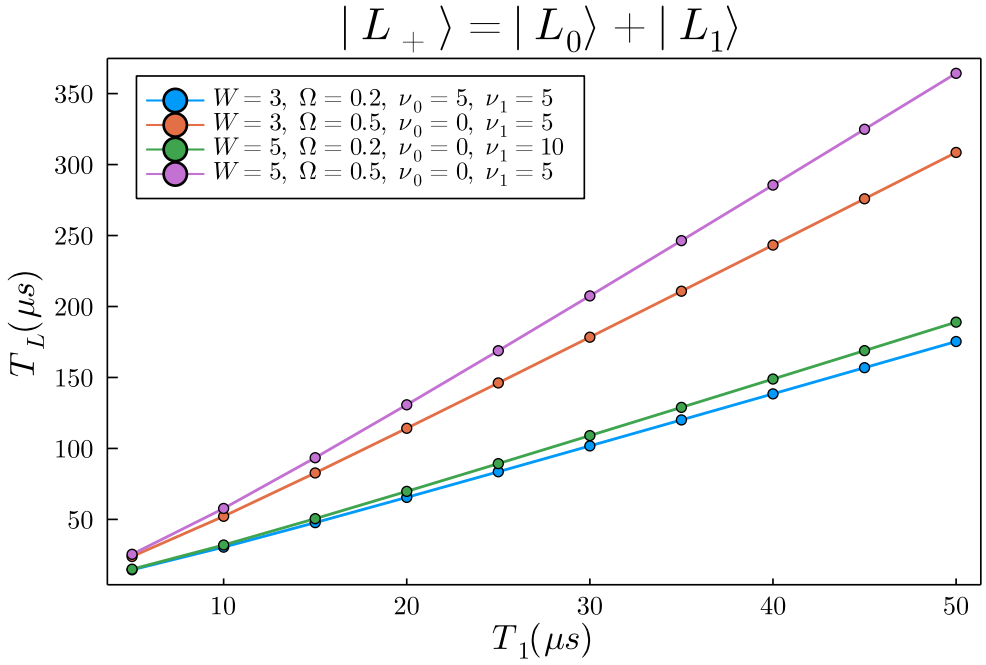

Figure 4.18: Logical lifetimes for $|+_L\rangle$. Response to the choice of drives and detunings is inline with what is observed in figures 4.16 and 4.17.

CHAPTER 5

DIGITIZING PULSE-SHAPED QUADRATURES IN THE RELAXATIONAL QUANTUM EIGENSOLVER

This chapter presents results on a project that is a work-in-progress with multiple members of our group involved. Following the theme of this thesis in general, the core idea of the relaxational quantum eigensolver (RQE) is to implement the variational quantum eigensolver (VQE) with driven-dissipative techniques. While a big focus in this thesis so far has been on using driven-dissipative techniques for autonomous quantum error correction, in chapter 3 we saw a slight detour from that main theme and looked at related approaches from chapter 2 to implement error-mitigation with pulse-shaping in the realization of two-qubit gates. This work follows that same thread, where the driven-dissipative implementations do not quite achieve error correction the same way the VSLQ does, but we do mitigate errors akin to state stabilization in section 1.3. The main defining aspect of this work is that the dissipative engineering here is digitized at the quantum-algorithm level and is hardware agnostic, unlike all of the previous work which assumed superconducting architectures. The driven-dissipative mechanism is ported to variational algorithms so that their performance in the approximation of a problem Hamiltonian ground state can be improved. Thus, we begin this chapter with a quick primer on VQE, later moving on to implementing techniques broadly discussed in section 1.3.

5.1 The Variational Quantum Eigensolver (VQE)

A brief introduction to VQE was given in section 3.4, but here we expand a bit on it to make the introduction of RQE more natural. The variational quantum eigensolver is a scheme that is used for finding the ground states of quantum Hamiltonians H_1 (called the problem Hamiltonian). The core of the idea is to start the quantum system with a simple Hamiltonian H_0 whose eigenstates are generally easy to determine, with the ground state easy to prepare.

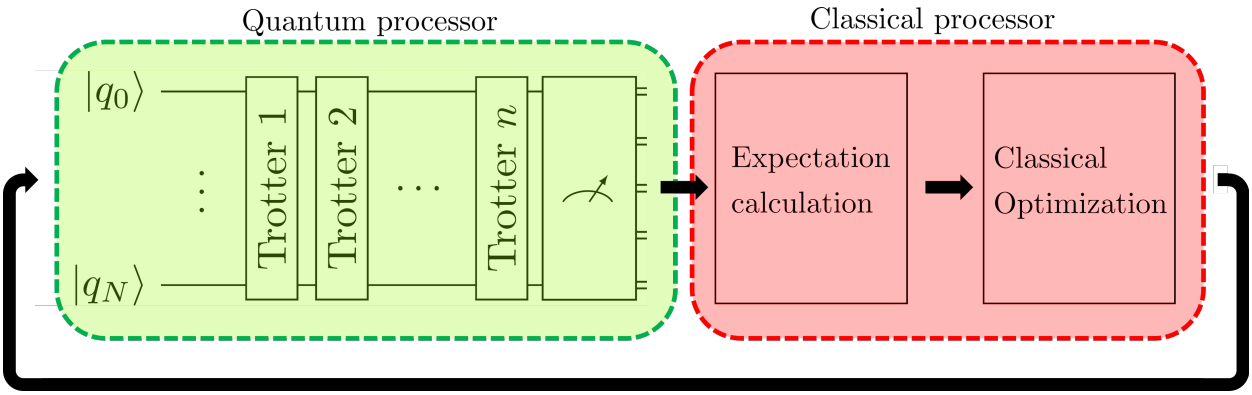

Figure 5.1: Schematic for the idea behind the variational quantum eigensolver using n Trotter steps. A quantum state is initialized and fed through the quantum circuit highlighted in green. Examples of what the Trotter steps can look like are in equation 5.8, and figure 5.2. At the end of the quantum circuit, the expectation value of use case operations are measured with the final state. Afterwards, using classical post-processing, highlighted in red, provides feedback for re-running the quantum circuit. This feedback can entail classical optimization over a parameter space characteristic of the quantum system to better approximate the problem Hamiltonian ground state.

Then by applying a Hamiltonian $H(t)$ that changes from H_0 to H_1, taking the from

$$H(t) = \left(1 - \frac{t}{t_f}\right) H_0 + \frac{t}{t_f} H_1, \tag{5.1}$$

where t evolves from 0 to t_f, and we measure the system at the end to determine if during the evolution from H_0 to H_1, we have evolved the H_0 ground state to the H_1 ground state (the stated goal). What makes this a hybrid quantum-classical algorithm is that after measuring the system at the end of a cycle, we can classically optimize over parameters used in the preparation of the initial quantum state, and repeat the procedure, with every iteration classically optimizing over some parameter space. In section 3.4, this classical optimization was done over parameters in equation 5.1 at every iteration, instead of the traditional optimization over state preparation parameters.

To implement the evolution of $H(t)$ in a gate model quantum computer, we take advantage of Trotterization. The Hamiltonian in equation 5.1 will evolve a quantum state by the unitary evolution $U(t) = e^{iH(t)dt}$, where if H_0 and H_1 commute, we can simply

express the action of this unitary on a quantum state $|\psi\rangle$ as

$$e^{iH(t)dt}|\psi\rangle = e^{i\left[\left(1-t/t_f\right)H_0+t/t_f H_1\right]dt}|\psi\rangle = e^{i\left(1-t/t_f\right)H_0 dt}e^{it/t_f H_1 dt}|\psi\rangle\,. \tag{5.2}$$

However, there is no requirement that H_0 and H_1 commute and in fact, they don't for any interesting problem that we would care to solve using this technique. Thus the expression in equation 5.2 is not generally valid. However, if dt is sufficiently small, we can approximate it as

$$e^{i\left[\left(1-t/t_f\right)H_0+t/t_f H_1\right]dt}|\psi\rangle \approx \left(e^{i\left(1-t/t_f\right)H_0 dt}e^{it/t_f H_1 dt}+O(dt^2)\right)|\psi\rangle\,. \tag{5.3}$$

This is called the Trotter decomposition, and is what allows us to implement a continuous time evolution Hamiltonian using a digitized, gate-based model. Back in section 3.4, we looked at the Antiferromagnetic Heisenberg Model (AFM), for which the trivial Hamiltonian was

$$H_0 = V\sum_n \sigma_n^z, \tag{5.4}$$

and a problem Hamiltonian

$$H_1 = J\sum_m \left(\sigma_m^x\sigma_{m+1}^x + \sigma_m^y\sigma_{m+1}^y + \sigma_m^z\sigma_{m+1}^z\right). \tag{5.5}$$

Following the same decomposition, we digitize equation 5.4 as

$$e^{if(t)H_0 dt} = e^{iVf(t)\sum_n \sigma_n^z dt} = \prod_n e^{iVf(t)\sigma_n^z dt}, \tag{5.6}$$

meanwhile doing the same procedure on the problem Hamiltonian in equation 5.5 gives us

$$\begin{aligned} e^{if(t)H_1 dt} &= e^{iJf(t)\sum_m\left(\sigma_m^x\sigma_{m+1}^x+\sigma_m^y\sigma_{m+1}^y+\sigma_m^z\sigma_{m+1}^z\right)dt} \\ &= \prod_m \left(e^{iJf(t)\sigma_m^x\sigma_{m+1}^x dt}\right)\left(e^{iJf(t)\sigma_m^y\sigma_{m+1}^y dt}\right)\left(e^{iJf(t)\sigma_m^z\sigma_{m+1}^z dt}\right). \end{aligned} \tag{5.7}$$

putting this all together by combining equations 5.6 and 5.7 with equation 5.3, and dropping the dt^2 order so that we have approximately equation 5.2, we get the final digitized form of the evolution for equation 5.1 using the AFM Heisenberg model,

$$e^{iH(t)dt} = \left(\prod_n e^{iV\left(1-t/t_f\right)\sigma_n^z dt}\right)\prod_m \left(e^{iJ\sigma_m^x\sigma_{m+1}^x t/t_f dt}\right)\left(e^{iJ\sigma_m^y\sigma_{m+1}^y t/t_f dt}\right)\left(e^{iJ\sigma_m^z\sigma_{m+1}^z t/t_f dt}\right). \tag{5.8}$$

Here we can now see that the quantum part of the algorithm simply boils down to applying the unitaries in equation 5.8 repeatedly for every iteration of dt from $t = 0$ to $t = t_f$. Once the final set of gates has been applied for $t = t_f$, we can measure the expectation value, and as stated above, use our preferred classical optimization routine over a parameter space in the trivial Hamiltonian in equation 5.4 or the system evolution in equation 5.8, and repeat the quantum evolution process.

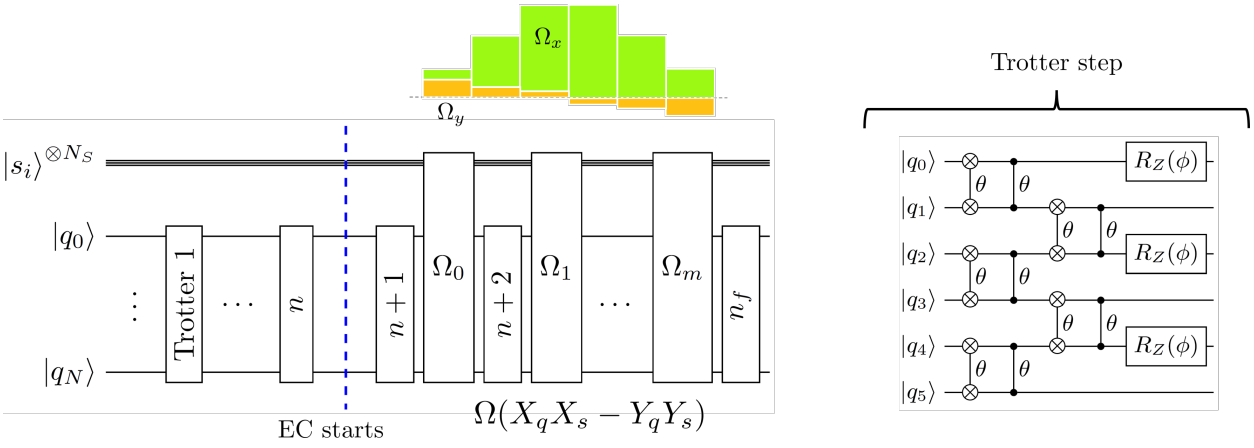

Figure 5.2: Illustration of modifications to a standard VQE setup as shown in figure 5.1. We have added a set of lossy shadow resonators to use for passive error correction. The protocol starts out the same as traditional VQE, but for a total number of Trotter steps n_f, we specify a Trotter step n after which we begin the driven-dissipative protocol between the primary qubits $|q_N\rangle$ and the lossy resonators $|s_{N_S}\rangle$ that has been a big focus of this thesis. The example Trotter step in this figure is the same as that from section 3.4, and is the problem Hamiltonian for results in this section. We also illustrate how the digitization of the DRAG-like qubit-resonator coupling is done, where the coupling strength Ω is turned into two quadratures Ω_x (green) and Ω_y (orange), which take on time-parameterized sinusoidal waveforms, similar to work done in chapter 2.

5.2 Adding driven dissipative engineering

Variational algorithms are generally seen as hopeful applications in the NISQ era of quantum computing. But the performance of VQE is limited by gate errors that proliferate in the circuit, and is the limiting factor in VQE finding the true ground state of a given problem. Using shallower circuits would help reduce the proliferation of errors, but using fewer gates in itself also limits the accuracy of a VQE run. Determining the best

performance for a given VQE algorithm is a careful balance between gate depth and acceptable accuracy. Developing high-performing VQE systems thus comes down to the choice of variational operator sequence. To help in this endeavor, RQE aims to provide an advantage for variational algorithms by reducing the proliferation of errors by using driven-dissipative stabilization. This is illustrated in figure 5.2, where we see the idea of VQE playing out for the system of primary qubits $|q_N\rangle$, using a number n_f of Trotter steps. This main part is no different than what would be done in the example in figure 5.1. However, here we specify a Trotter step n after which a driven coupling between the primary qubits $|q_N\rangle$ and the shadow resonators $|s_{N_S}\rangle$ is turned on. This coupling drive is also digitized and is applied in interlocking steps with the main problem Hamiltonian algorithm. This coupling Hamiltonian looks very similar to what has been presented in previous chapters,

$$H_{PS} = \Omega \sum_{i}^{N_P} \sigma_{iP}^{x,y,z} \sigma_{iS}^{x}, \tag{5.9}$$

where we have assumed that we have an equal number of shadow resonators as we do primary qubits, $N_P = N_S$, though this does not need to be the case. The only requirement is that the number of shadow resonators N_S should scale linearly with increasing number of primary qubits N_P. But for $N_S < N_P$, we can have multiple qubits coupled to the same resonator, since they are only acting as a bath for the driven correction mechanism. We can define interactions such as the blue-sideband coupling used in previous chapters for the error correction mechanisms using the digitized Pauli operators. Noting that

$$\begin{aligned} \sigma^x &= \sigma^+ + \sigma^- \\ \sigma^y &= i\left(\sigma^+ - \sigma^-\right), \end{aligned} \tag{5.10}$$

we can easily verify that

$$\begin{aligned} \sigma_1^x \sigma_2^x - \sigma_1^y \sigma_2^y &= 2\left(\sigma_1^+ \sigma_2^+ + \sigma_1^- \sigma_2^-\right) \\ \sigma_1^x \sigma_2^x + \sigma_1^y \sigma_2^y &= 2\left(\sigma_1^+ \sigma_2^- + \sigma_1^- \sigma_2^+\right), \end{aligned} \tag{5.11}$$

giving us both the blue- and red-sideband coupling terms prevalent in our driven correction schemes. If we were interested in having a blue-sideband qubit-resonator

coupling to achieve state stabilization akin to that demonstrated in section 1.3, H_{PS} would then become

$$H_{PS} = \frac{\Omega}{2} \sum_{i}^{N} \left(\sigma_{iP}^{x} \sigma_{iS}^{x} - \sigma_{iP}^{y} \sigma_{iS}^{y} \right), \tag{5.12}$$

which we can digitize like we have for equation 5.8 to help protect against photon losses. Here we have replaced the summation term to simply N instead of N_P to specify that the number of shadow resonators and primary qubits may be different, and the sum can iterate over only N_S, or N_P using multiple primary qubits per shadow resonator for the case $N_S < N_P$.

Adding this to the Heisenberg AFM model Hamiltonian in equation 5.5, and letting the shadow Hamiltonian be

$$H_S = \frac{\omega_S}{2} \sum_{j}^{N_S} \sigma_{jS}^{z}, \tag{5.13}$$

we can get a final form of the unitary operation that gets actually run on quantum hardware,

$$|\psi(t + dt)\rangle = U(t) \, |\psi(t)\rangle \, , \tag{5.14}$$

with $U(t) = e^{i(H_P + H_S + H_{PS})dt}$, giving us

$$\begin{aligned} U(t) \, |\psi\rangle &= e^{i(H_P + H_S + H_{PS})dt} \, |\psi\rangle \\ &= \prod_{p}^{N_P} \left(e^{iJ\sigma_p^x \sigma_{p+1}^x dt} \right) \left(e^{iJ\sigma_p^y \sigma_{p+1}^y dt} \right) \left(e^{iJ\sigma_p^z \sigma_{p+1}^z dt} \right) \left(\prod_{s}^{N_S} e^{\frac{i}{2}\omega_S \sigma_s^z dt} \right) \\ &\quad \times \left(\prod_{n}^{N} e^{\frac{i}{2}\Omega \sigma_{nP}^x \sigma_{nS}^x dt} e^{\frac{i}{2}\Omega \sigma_{nP}^y \sigma_{nS}^y dt} \right) \left[\bigotimes_{k}^{N_P + N_S} |q_k\rangle \right], \end{aligned} \tag{5.15}$$

where the $|q_k\rangle$ states represent all primary N_P and shadow N_S qubtis, explicitly showing us the sets of unitaries that are repeatedly applied in each Trotter step as long as the Trotter step size dt is small enough. Otherwise, we run into the problem in equation 5.3 where we have to account for the fact that the operators in the full Hamiltonian do not necessarily commute, which is the case for equation 5.15.

The results presented in the following section go a step further and introduce a time-parameterized qubit-resonator coupling inspired by DRAG (similar to [77], as shown

in figure 5.2. Here, we take the coupling term in equation 5.12 and add a second quadrature,

$$H_{PS} = \frac{\Omega_x(t)}{2} \sum_i^N \left(\sigma_{iP}^x \sigma_{iS}^x - \sigma_{iP}^y \sigma_{iS}^y\right) + \frac{\Omega_y(t)}{2} \sum_i^N \left(\sigma_{iP}^x \sigma_{iS}^y + \sigma_{iP}^y \sigma_{iS}^x\right), \tag{5.16}$$

where the $X_1Y_2 + Y_1X_2$ term in the Ω_y quadrature gives us the effective $i\left(\sigma_1^+\sigma_2^+ - \sigma_1^-\sigma_2^-\right)$ we want, just like we did back in chapter 2. Digitizing this is a straightforward repetition of equation 5.15 at this point, and so we now present results for RQE using this DRAG-like coupling.

5.3 Results using two-quadrature coupling

The simulation results presented here cover systems of 8, 10, 12, 14, 16, and 18 primary qubits, letting the number of shadow qubits $N_S = N_P/2$. Thus the 18-qubit case is actually a simulation of a 27-qubit wavefunction. Following the same idea from [77], we let

$$\begin{aligned} \Omega_x(t) &= \Omega_0^x \sin(\pi t/t_f) \\ \Omega_y(t) &= \Omega_0^y \cos(\pi t/t_f), \end{aligned} \tag{5.17}$$

as illustrated in figure 5.2. $\Omega_0^{x,y}$ are the overall amplitudes for the entire waveform, and we explore scans over these two parameters. This is a much more simplistic approach compared to the gradient-ascent optimization done in [77], where having the pixelated pulse shape allows for individually changing the strength Ω for each pixel. That method was the motivation for the smooth pulse-shaping that was implemented in chapter 2, and is a method that would work very well for RQE since the pixelation of the pulse shapes is exactly the same as the digitization of the pulses shown in figure 5.2. However, the purpose of the work presented here is only a preliminary exploration to see if there would be a benefit at all to implementing the primary-shadow interaction this way. So we compare results using the two-quadrature implementation to simply using a fixed coupling strength for a single quadrature.

Parameter scans for the fixed coupling implementation are shown in figure 5.3. As a variational algorithm, the full parameter space that we would need to optimize to get the

best ground state energy estimation is significantly more complex, and ultimately this project aims for using nonlinear optimization methods over the more complete parameter space. However, in setting out to explore the viability of the two-quadrature method, we are really only interested in exploring parameters that are directly related to the error correction mechanism itself. From equation 5.15, those are the coupling strength Ω, and the shadow qubit energies ω_S. We note that in equation 5.9 and equation 5.13, we assume the same the same values for Ω and ω_S in each individual qubit-resonator pair, and each individual resonator, respectively. This does not necessarily have to be the case, and each may be different. But it is an assumption that we carry into the work presented here for computational feasibility. the only error channel considered for the results presented in this section is photon loss. A more complete picture would also include phase noise, since unlike the logical manifolds explored in chapter 2 and chapter 4, this is not a topology that suppresses noise, and would need to address it with specific driving terms. Seeing as photon loss is generally seen as a harder error channel to suppress, we focus the discussion on it.

Results from figure 5.3 look at the percent of the ground state calculated for the AFM Heisenberg model (equation 3.9). These show that using a good choice of parameters, even though there is a general performance hit as the number of qubits in the variational algorithm increases, the ground state energy estimation seems to taper off a bit. In itself, this image alone demonstrates the usefulness of RQE, and given that there is still a lot of work to be done in the aforementioned parameter space, is very promising for the continuous development of the technique and further exploration of different quantum systems. But this parameter space was primarily explored to have a standard by which to compare results using a two-quadrature, time-parameterized coupling strength. Results for this are shown in figure 5.4, where we fix the shadow resonator energy to $\omega_S = 3$ for all the different system sizes. We also note that for both sets of results shown in figure 5.3 and figure 5.4, the parameter space for the 18 qubits system is greatly reduced—a quarter of that for all the other systems—due to computational limitations.

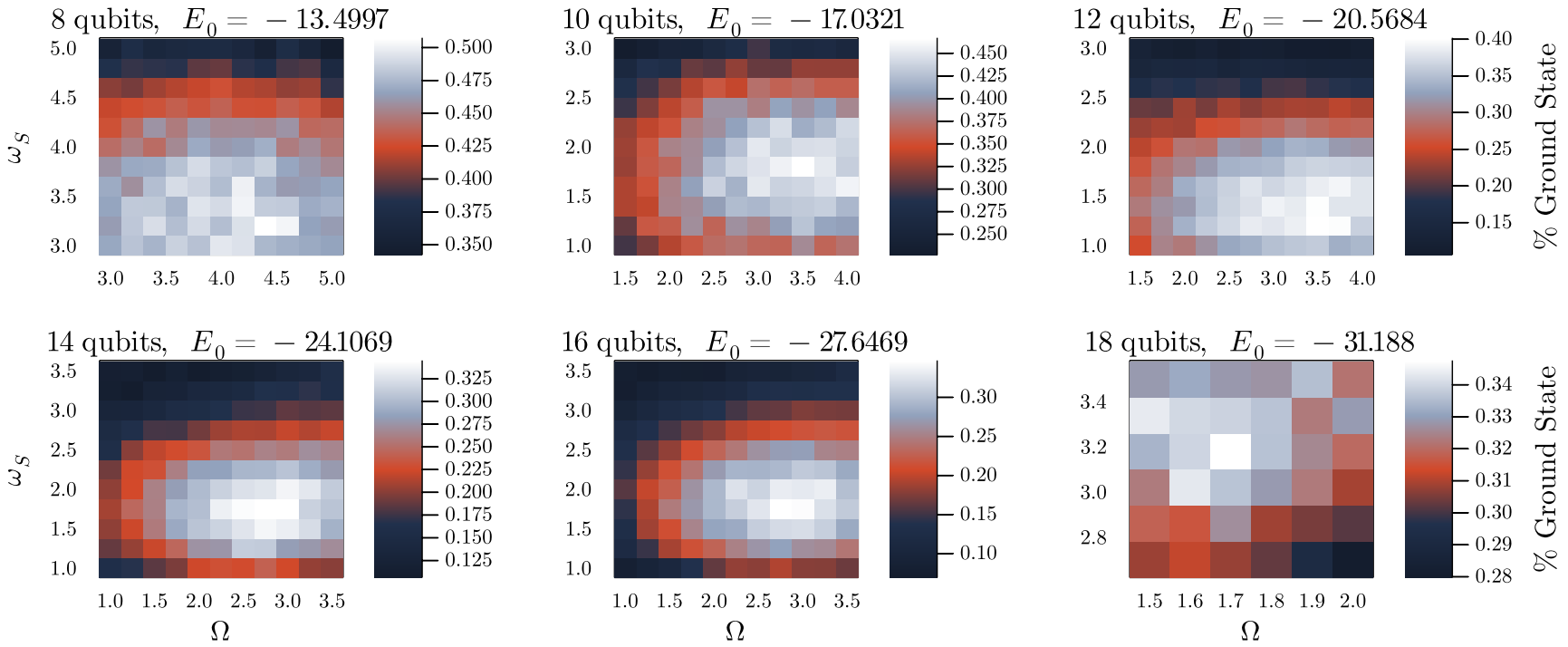

Figure 5.3: Parameter scans for the primary-shadow coupling Ω using a fixed value, and the shadow resonator energies ω_S. We see already that a strong photon loss error channel introduces a big performance hit in the ground state energy estimation, as good parameter choices indicated in these plots give slightly above 50% for 8 qubits, and down to about 35% for 14 and 16 qubits. for absolutely best parameter choices, we would expect the 18 qubit case to have the highest performance hit, but this parameter exploration provides a good quantitative and qualitative sense for the benefits of using the driven-dissipative error correction mechanism.

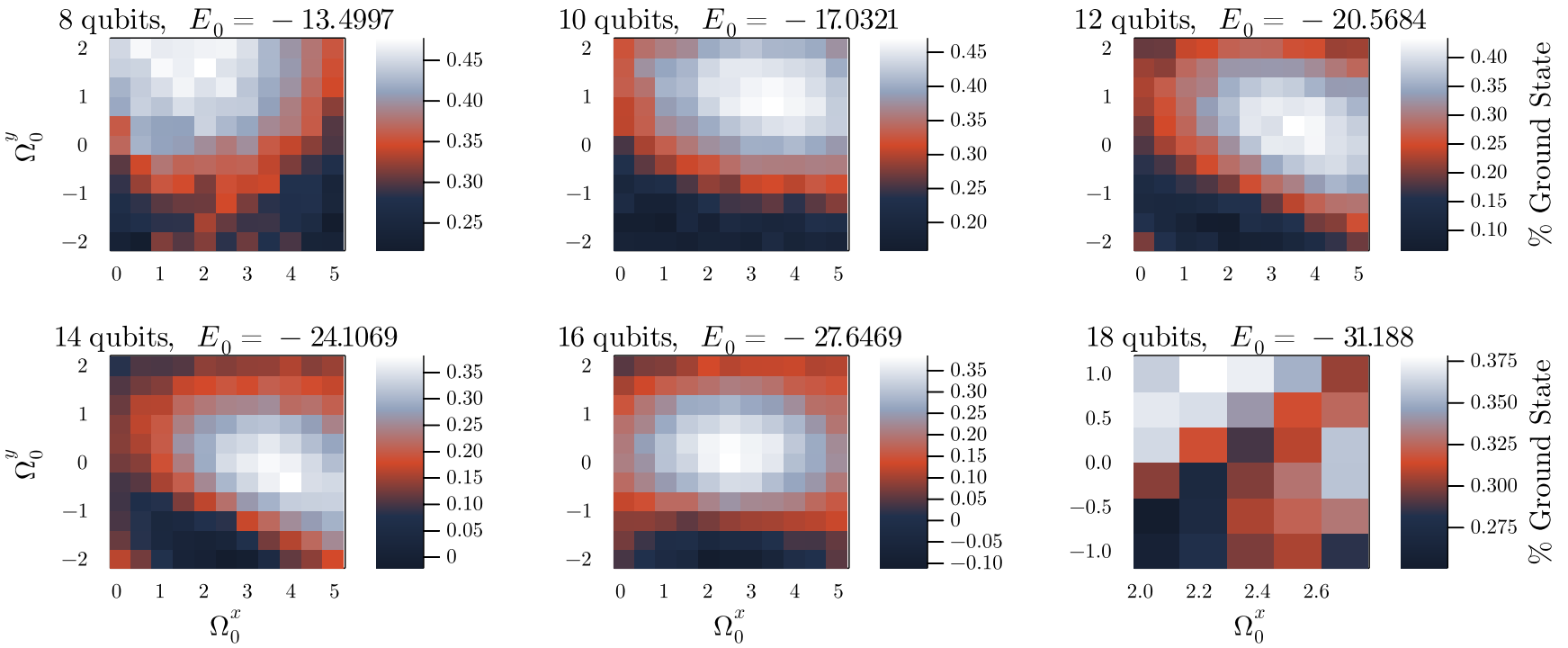

Figure 5.4: Using a fixed $\omega_S = 3$, we do parameter scans for the primary-shadow coupling quadrature amplitudes Ω_0^x and Ω_0^y, exploring the overall amplitude (as opposed to more complex pulse-shaping). We see a general, though slight, advantage using the DRAG-like shapes for the coupling strength quadratures, particularly for the larger qubit systems. Note that the smaller number of qubit systems actually show a performance hit for the parameter space explored.

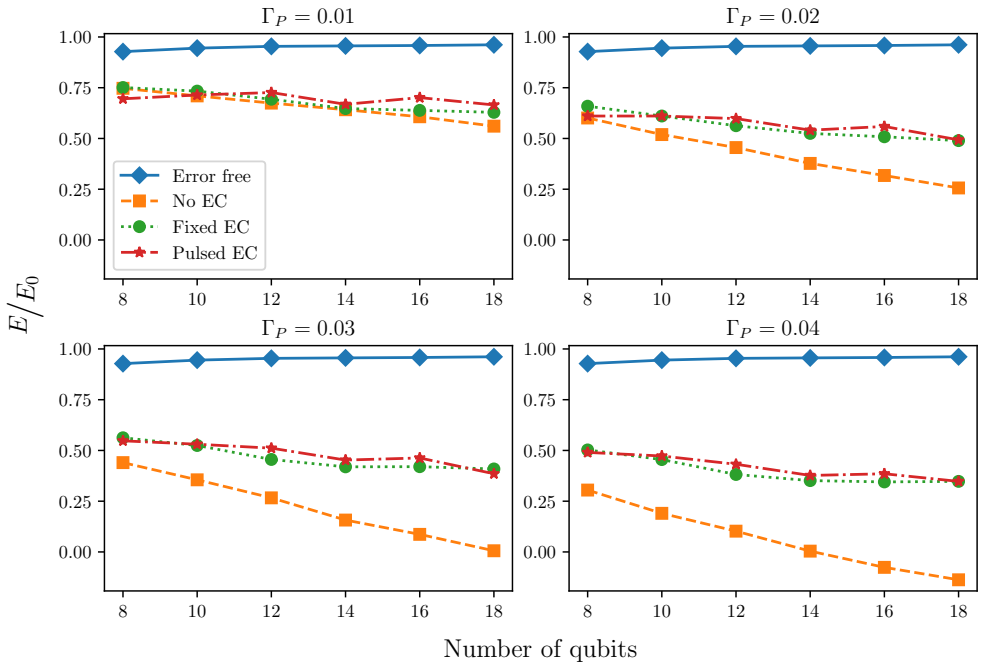

Figure 5.5: Looking at the performance of different system sizes using results from figures 5.3 and figure 5.4 for different photon loss rates. Here, it's hard to see much of a benefit, and in some particular cases the fixed coupling is better. Not that the fixed coupling results for 12 qubits are far from preferred parameters that would give better results, as is clear from figure 5.3.

There is a slightly noticeable advantage in using the two-quadrature, time-parameterized coupling over a single-quadrature fixed coupling. It is not a very dramatic performance improvement, but we note that using a fixed shadow resonator energy for all system sizes will definitely present a limiting factor in how well this method will perform. The fact that we are able to see an advantage without exploring different values of ω_S speaks to the advantage that this method can provide. Especially considering that when looking at the results in figure 5.3, the performance of the variational algorithm can be seen to have a definite dependence on the shadow resonator energy ω_S. Additionally, while it is also clear from those same results that the range of parameters that were explored is locally optimal, we do not know what the rest of the parameter space looks like, and so we can conclude that there is still a big benefit in using, with areas to improve, a fixed coupling strength. Ultimately, this entire set of results is promising, and motivates continued research into RQE.

We use the results from figures 5.3 and 5.4, which were obtained assuming a photon loss rate $\Gamma_P = 0.04$, and apply them for loss rates $\{0.01, 0.02, 0.03, 0.04\}$. Figure 5.5 shows the percent of the true ground state that these different methods are able to achieve. While it generally seems that the time-parameterized coupling does perform better than the fixed coupling, it is only marginally so. It is also clear from these results that the parameters for the fixed coupling in the 12 qubit case are far from a good set, which is also clear looking at its parameter scan in figure 5.3. Also note that for a handful of cases, there is no improvement in using a pulsed coupling over fixed. Particularly for 8 and 10 qubits with an error rate $\Gamma_P = 0.01$, 8 qubits for $\Gamma_P = 0.02$, 8 and 18 qubits for $\Gamma_P = 0.03$, and 8 qubits for $\Gamma_P = 0.04$. This could be largely attributed to using a fixed shadow energy ω_S, since we see a more noticeable improvement using an intermediate number of qubits for all different loss rate cases. Additionally, looking at how far apart the error corrected results are still from the error-free ground state energy calculations, this clearly motivates the use of more sophisticated optimization algorithms over the parameter spaces moving forward.

CHAPTER 6

CONCLUSIONS

To conclude this thesis, I go over a quick discussion on the results that have been presented thus far, as well as future directions that all of this can take moving forward. The projects presented here show a very promising use of driven-dissipative techniques and pulse-shaping for near term applications of quantum computing. Although there is still a lot of work to do on the experimental end for a wider adaptation of driven-dissipative techniques in superconducting qubit architectures, the theory and simulation for many of it's applications are incredibly promising.

6.1 Proposing a pulse-reset scheme

The work presented in chapter 2 proposed techniques in addressing limiting factors in the driven-dissipative mechanism that is the hallmark of autonomous quantum error correction. These are mainly from a careful balance in the strength of the off-resonant drive that refills photon losses, and the lossiness of the bath systems that are used for the off-resonant coupling. The off-resonant drive needs to be strong enough so that errors are quickly corrected back to a target state to stabilize at the occurrence of an error, but not so strong that off-resonant transitions induce occupations of leakage states. The decay rate of the lossy system needs to be lossy enough so that as the coupling mechanism refills photon losses, with high likelihood the lossy system decays back to its subsystem ground state and the target state is stabilized. However, too much noise from the lossy system induces linewidth broadening for higher energy states, which in turn increase the probability of off-resonant transitions into leakage states.

To address these limiting factors, we proposed a cyclical pulse-reset scheme that suppresses both of the stated problems. We looked at limiting the issue of the coupling drive strength by implementing numerical optimization of pulse-shaping techniques inspired by the DRAG and GRAPE protocols. This allowed us to greatly increase the operation fidelity by suppressing off-resonant transitions into leakage states. This

numerically optimized pulse is applied during the pulse cycle of the scheme, and is completely turned off during the reset cycle. The second critical component of this scheme is that during the pulse cycle, the decay rate of the lossy system is artificially brought down so that it is no longer lossy. This can be experimentally achieved by adding another reservoir that is red-sideband coupled to the first lossy system, thereby introducing a control for when to induce a reset of a quantum state. In simulation, we simply specify this as time-parameterized loss rate. So by lowering the loss rate during the pulse cycle, and by making the loss rate high during the reset cycle (to induce resets) with the coupling to the primary system completely turned off, we suppress leakage induced from linewidth broadening in the presence of the lossy system. This technique was demonstrated on small logical qubits, where we demonstrated a general advantage in the prolonging of the logical manifold coherence.

The main roadblock to consider going forward is that schemes for state stabilization still suffer from low fidelities experimentally, with a plethora of physical considerations limiting the performance. Additionally, since the time-parameterization of the reservoir decay rate is done artificially in simulation, a realistic implementation might not provide the observed advantages due to the intricacies involved in coupling multiple systems. The biggest upside is that, in theory, there are no assumptions about any of this work that would not make it realizable with the state fo the art.

6.2 Error-divisible gates

A very important result that came out of the numerical pulse-shaping in the pulse-reset scheme that was not directly laid out by the scheme itself, was the use of counter-oscillating frequencies in the pulse-shaped quadratures for the suppression of leakage. This was more formally developed in chapter 3 using perturbation theory to demonstrate why the use of oscillatory terms can cancel out unwanted, and we proposed a criteria using this formality to demonstrate how this can implement error-divisible gates. First, we provide the motivation for and define what a fractional gate is. This is useful for

NISQ algorithms, of which a lot make use of small-angle, two-qubit rotations. Generally implementing these small-angle rotations using a stock gate set tends to proliferate two-qubit gate error throughout the quantum circuit, thereby limiting the performance of the quantum algorithm. This scheme provides a simple protocol to implement the two-qubit gates natively at no cost to gate error. This is successfully demonstrated in simulation for fractional iSWAP gates and XX gates, where we achieve error divisibility down to 1/6 and 1/4 of a full rotation, respectively.

While all the theory and simulations did not assume any hardware specifications, an experimental demonstration of error-divisibility has unfortunately been elusive. Indeed, the motivation for this protocol is to provide an advantage in the NISQ era of quantum computing, and an experimental realization would give credence to that. However, the struggles in experimentally realizing this protocol may have a lot to do with a different experimental project—the VSLQ! As discussed in chapter 4, physical challenges in the design of the VSLQ has made an experimental demonstration of the VSLQ logical manifold difficult. The VSLQ is also a great candidate for demonstration of error-divisible gates, where we are developing a high level of control between two transmon qubits. Unfortunately, this meant delays in the VSLQ realizations meant delays in the demonstration of error-divisible gates. Another interesting thing to explore is if this protocol is robust for Clifford gates (appendix D.3) operating on more than two qubits, since that would provide another utility for NISQ algorithms. For now, physically implementing this protocol remains an open door.

6.3 The VSLQ-Star protocol

The VSLQ device as was introduced in chapter 1, and explored further in chapter 2, faced difficulties in the experimental realization, as briefly touched on this last section. While nothing about the design made it impossible to realize, the four-photon exchange driving term that was fundamental to the stabilization fo the logical manifold introduced problems such as frequency crowding and crosstalk. To that end, a new protocol was

developed that achieved the same stabilization of logical codewords that does not require a four-photon process. The new protocol, called the VSLQ-Star protocol, only used two-photon processes and linear couplers, greatly reducing dispersive shifts introduced from frequency crowding and making the device much simpler to implement.

One focal notion in this updated protocol is the addition of frequency detunings to separate the desired logical codewords from other system eigenstates. These type of clever operations on the system are what allows error correction to happen, but it is done at the cost of losing some intuition as to how exactly this works since we introduce multiple rotating wave transformations to get the desired Hamiltonian that stabilizes the codewords. As the implementation of this physically simpler device is being achieved, chapter 4 explores the detunings space to determine a preferred set of choices that would allow the easiest realization of logical state stabilization, as well as gain intuition into the interplay of the detunings with the new Hamiltonian. This parameter exploration determined working parameters that show notable improvements in the logical lifetime using relatively weak drives, which is particularly useful in experiment. As progress continues, the results presented in this chapter will hopefully facilitate a demonstration of AQEC with this protocol. This might have its limitations, however, seen as simulations are still not a perfect one-to-one mapping to the lab implementation. Thus, continued collaboration with the experimental effort remains crucial moving forward with the VSLQ.

6.4 Relaxational quantum eigensolver

While a recurring theme in the projects in this thesis focus around experimental feasibility on state of the art devices, perhaps the one with the most immediate potential is the relaxational quantum eigensolver. This is in large part due to the fact that variational algorithms are a very deep subject of exploration at the time of writing as they are designed to run on near-term devices. Furthermore, the implementation of the driven-dissipative coupling to a lossy reservoir in this case does not rely on transitions to more exotic manifolds like it does in the VSLQ. Everything about RQE is ready to be

tested now, indeed, the demonstrations of an advantage using RQE are in the plans to be shown using commercially available quantum processing hardware, as all the interactions for the problem Hamiltonian as well as the shadow couplings are digitized into a gate model, allowing us to directly code it up on a cloud-based machine without requiring any intricate, hardware-level manipulations.

The main contribution from this thesis in chapter 5 is a demonstration of an advantage in RQE by emulating a digitized version of using time-parameterized coupling between the primary qubits and the shadow qubits. Like the detunings space exploration for the VSLQ-Star, the exploration og parameters spaces here is far from optimal, and more intricate uses of nonlinear optimization techniques for multi-variate cost functions will be implemented for RQE algorithms in generla moving forward. But hte feasible advantage demonstrated in this chapter with only minimal fine tuning of a small parameter space is very encouraging, and suggests that including the two-quadrature parameterization of the coupling strength in future RQE optimization protocols should provide a better advantage for ground state estimation. More computationally expensive endeavors include something like what was done in chapter 2, where the coupling strength pulse shape is optimized. While this work only scanned over different overall quadrature amplitudes, it would be possible to use optimization algorithms for each individual pixel strength, though this might be prohibitively expensive for large system sizes. If this were the case, finding optimal pulse shapes for more feasible system sizes could still be applied for larger sizes. Other methods to use is to simply try different overall envelopes. This work used very naive sinusoidal shapes, but using more exotic envelope waveforms such as the ones in chapter 3 could provide a bigger improvement.

6.5 Future directions

There is seemingly a lot of potential for finding immediate use in driven-dissipative systems. A repeated theme here is that while a lot of analysis explicitly considers transmon devices, all of this is generally possible with strongly anharmonic devices as well,

further expanding the potential use for techniques like the ones presented in this thesis. Undoubtedly, work that can be immediately implemented on physical devices should be thoroughly explored to hopefully more efficiently support the development of the field. The way I see it, currently we are at an inflection point were the field is simultaneously trying to find applications for near-term devices, while also working towards the ever promising regime of fault-tolerant quantum computing. The great thing about the work in this thesis is that it tries to contribute to both efforts, since while the techniques are particularly relevant in noisy devices (and become obsolete as single qubit lifetimes get better), it also provides a blue print to achieve fault-tolerance faster. This is of course the motivation for the VSLQ, and future work in incorporating small logical qubit devices—like the VSLQ—into broader digital error correction codes is a very exciting prospect and direction to take as the VSLQ itself gets closer to reality. But given the many hurdles that still need to be cleared for demonstrating AQEC in the regimes covered in this work, such a hybrid QEC approach is still far in the future, despite the fact that the constituent parts are all immediately realizable today—putting it all together is quite the challenge! Nevertheless, this is something that the author is very interested in, and seems like a very natural progression for the field to take moving forward. In the meantime, furthering efforts for a demonstration of VSLQ state stabilization are high on the priority queue, as well as explorations for NISQ. The latter of those two are highly prized, and there is so much more to understand in RQE, with many more applications to explore its use with. The work here barely scratched a small region of all the possibilities RQE has to offer.

REFERENCES

[1] C.-F. Li, G.-C. Guo, and J. Piilo. Non-Markovian quantum dynamics: What does it mean? 127(5):50001, October 2019. ISSN 0295-5075. doi: 10.1209/0295-5075/127/50001. URL https://doi.org/10.1209/0295-5075/127/50001. Publisher: IOP Publishing.

[2] Christopher Chamberland, Kyungjoo Noh, Patricio Arrangoiz-Arriola, Earl T. Campbell, Connor T. Hann, Joseph Iverson, Harald Putterman, Thomas C. Bohdanowicz, Steven T. Flammia, Andrew Keller, Gil Refael, John Preskill, Liang Jiang, Amir H. Safavi-Naeini, Oskar Painter, and Fernando G. S. L. Brandão. Building a fault-tolerant quantum computer using concatenated cat codes. *arXiv:2012.04108 [quant-ph]*, December 2020. URL http://arxiv.org/abs/2012.04108. arXiv: 2012.04108.

[3] P. Magnard, P. Kurpiers, B. Royer, T. Walter, J. C. Besse, S. Gasparinetti, M. Pechal, J. Heinsoo, S. Storz, A. Blais, and A. Wallraff. Fast and Unconditional All-Microwave Reset of a Superconducting Qubit. *Physical Review Letters*, 121(6), aug 2018. ISSN 10797114.

[4] Eliot Kapit. Hardware-Efficient and Fully Autonomous Quantum Error Correction in Superconducting Circuits. *Physical Review Letters*, 116(15):150501, apr 2016. ISSN 0031-9007. doi: 10.1103/PhysRevLett.116.150501. URL https://link.aps.org/doi/10.1103/PhysRevLett.116.150501.

[5] Eliot Kapit. The upside of noise: engineered dissipation as a resource in superconducting circuits. *Quantum Science and Technology*, 2(3):033002, sep 2017. ISSN 2058-9565. doi: 10.1088/2058-9565/aa7e5d. URL http://stacks.iop.org/2058-9565/2/i=3/a=033002?key=crossref.ebb11baf69e9704628b76846b7082fc9.

[6] Austin G. Fowler, Matteo Mariantoni, John M. Martinis, and Andrew N. Cleland. Surface codes: Towards practical large-scale quantum computation. *Physical Review A - Atomic, Molecular, and Optical Physics*, 86(3), sep 2012. ISSN 10502947.

[7] Eliot Kapit. Universal two-qubit interactions, measurement, and cooling for quantum simulation and computing. *Physical Review A - Atomic, Molecular, and Optical Physics*, 92(1):012302, jul 2015. ISSN 10941622.

[8] Philip Krantz, Morten Kjaergaard, Fei Yan, Terry P. Orlando, Simon Gustavsson, and William D. Oliver. A quantum engineer's guide to superconducting qubits. *Applied Physics Reviews*, 6(2):021318–021318, June 2019. doi: 10.1063/1.5089550. URL http://arxiv.org/abs/1904.06560.

[9] Jens Koch, Terri M. Yu, Jay Gambetta, A. A. Houck, D. I. Schuster, J. Majer, Alexandre Blais, M. H. Devoret, S. M. Girvin, and R. J. Schoelkopf. Charge-insensitive qubit design derived from the Cooper pair box. *Physical Review A - Atomic, Molecular, and Optical Physics*, 76(4), October 2007. doi: 10.1103/PhysRevA.76.042319.

[10] V. Peano and M. Thorwart. Dynamics of the quantum Duffing oscillator in the

driving induced bistable regime. *Chemical Physics*, 322(1):135–143, March 2006. ISSN 0301-0104. doi: 10.1016/j.chemphys.2005.06.047. URL https://www.sciencedirect.com/science/article/pii/S0301010405002636.

[11] E Paladino, Y. Galperin, G Falci, and B L Altshuler. 1/ f noise: Implications for solid-state quantum information. *Reviews of Modern Physics*, 86(2):361–418, 2014. doi: 10.1103/RevModPhys.86.361.

[12] Frederick C. Wellstood, Cristian Urbina, and John Clarke. Low-frequency noise in dc superconducting quantum interference devices below 1 K. *Applied Physics Letters*, 50(12):772–774, 1987. doi: 10.1063/1.98041.

[13] M. D. Reed, L. DiCarlo, S. E. Nigg, L. Sun, L. Frunzio, S. M. Girvin, and R. J. Schoelkopf. Realization of three-qubit quantum error correction with superconducting circuits. *Nature*, 482(7385):382–385, feb 2012. ISSN 0028-0836. doi: 10.1038/nature10786. URL http://www.nature.com/articles/nature10786.

[14] Joachim Cohen and Mazyar Mirrahimi. Dissipation-induced continuous quantum error correction for superconducting circuits. *Physical Review A*, 90(6):062344, dec 2014. ISSN 1050-2947. doi: 10.1103/PhysRevA.90.062344. URL https://link.aps.org/doi/10.1103/PhysRevA.90.062344.

[15] Eliot Kapit, Mohammad Hafezi, and Steven H. Simon. Induced Self-Stabilization in Fractional Quantum Hall States of Light. *Physical Review X*, 4(3):031039, sep 2014. ISSN 2160-3308. doi: 10.1103/PhysRevX.4.031039. URL https://link.aps.org/doi/10.1103/PhysRevX.4.031039.

[16] Michael Nielsen and Isaac Chuang. *Quantum Computation and Quantum Information*. Cambridge University Press, 2010.

[17] John Napp and John Preskill. Optimal Bacon-Shor codes. *arXiv:1209.0794 [quant-ph]*, September 2012. URL http://arxiv.org/abs/1209.0794. arXiv: 1209.0794.

[18] PL Kapitza. Dynamic stability of the pendulum with vibrating suspension point. *Soviet Physics–JETP*, 21(5):588–597, 1951.

[19] David Rodríguez Pérez and Eliot Kapit. Improved autonomous error correction using variable dissipation in small logical qubit architectures. *Quantum Science and Technology*, 6(1):015006, November 2020. ISSN 2058-9565. doi: 10.1088/2058-9565/abc3cb. URL https://doi.org/10.1088/2058-9565/abc3cb. Publisher: IOP Publishing.

[20] Y. Ma, Y. Xu, X. Mu, W. Cai, L. Hu, W. Wang, X. Pan, H. Wang, Y. P. Song, C. L. Zou, and L. Sun. Error-transparent operations on a logical qubit protected by quantum error correction. *Nature Physics*, sep 2020. ISSN 17452481. URL http://arxiv.org/abs/1909.06803.

[21] Jeffrey M. Gertler, Brian Baker, Juliang Li, Shruti Shirol, Jens Koch, and Chen Wang. Protecting a Bosonic Qubit with Autonomous Quantum Error Correction. apr 2020. URL http://arxiv.org/abs/2004.09322.

[22] Lasse Bjørn Kristensen, Morten Kjaergaard, Christian Kraglund Andersen, and Nikolaj Thomas Zinner. Hybrid Quantum Error Correction in Qubit Architectures. sep 2019. URL http://arxiv.org/abs/1909.09112.

[23] Zaki Leghtas, Gerhard Kirchmair, Brian Vlastakis, Robert J. Schoelkopf, Michel H. Devoret, and Mazyar Mirrahimi. Hardware-Efficient Autonomous Quantum Memory Protection. *Physical Review Letters*, 111(12):120501, sep 2013. ISSN 0031-9007. doi: 10.1103/PhysRevLett.111.120501. URL https://link.aps.org/doi/10.1103/PhysRevLett.111.120501.

[24] Mazyar Mirrahimi, Zaki Leghtas, Victor V Albert, Steven Touzard, Robert J Schoelkopf, Liang Jiang, and Michel H Devoret. Dynamically protected cat-qubits: a new paradigm for universal quantum computation. *New Journal of Physics*, 16(4): 045014, apr 2014. ISSN 1367-2630. doi: 10.1088/1367-2630/16/4/045014. URL http://stacks.iop.org/1367-2630/16/i=4/a=045014?key=crossref.df77b77b2a64682c9a452e70666578dc.

[25] L. Sun, A. Petrenko, Z. Leghtas, B. Vlastakis, G. Kirchmair, K. M. Sliwa, A. Narla, M. Hatridge, S. Shankar, J. Blumoff, L. Frunzio, M. Mirrahimi, M. H. Devoret, and R. J. Schoelkopf. Tracking photon jumps with repeated quantum non-demolition parity measurements. *Nature*, 511(7510):444–448, jul 2014. ISSN 0028-0836. doi: 10.1038/nature13436. URL http://www.nature.com/articles/nature13436.

[26] Z Leghtas, S Touzard, I M Pop, A Kou, B Vlastakis, A Petrenko, K M Sliwa, A Narla, S Shankar, M J Hatridge, M Reagor, L Frunzio, R J Schoelkopf, M Mirrahimi, and M H Devoret. Quantum engineering. Confining the state of light to a quantum manifold by engineered two-photon loss. *Science (New York, N.Y.)*, 347(6224):853–7, feb 2015. ISSN 1095-9203. doi: 10.1126/science.aaa2085. URL http://www.ncbi.nlm.nih.gov/pubmed/25700514.

[27] Victor V. Albert, Chi Shu, Stefan Krastanov, Chao Shen, Ren-Bao Liu, Zhen-Biao Yang, Robert J. Schoelkopf, Mazyar Mirrahimi, Michel H. Devoret, and Liang Jiang. Holonomic Quantum Control with Continuous Variable Systems. *Physical Review Letters*, 116(14):140502, apr 2016. ISSN 0031-9007. doi: 10.1103/PhysRevLett.116.140502. URL https://link.aps.org/doi/10.1103/PhysRevLett.116.140502.

[28] Nissim Ofek, Andrei Petrenko, Reinier Heeres, Philip Reinhold, Zaki Leghtas, Brian Vlastakis, Yehan Liu, Luigi Frunzio, S. M. Girvin, L. Jiang, Mazyar Mirrahimi, M. H. Devoret, and R. J. Schoelkopf. Extending the lifetime of a quantum bit with error correction in superconducting circuits. *Nature*, 536(7617):441–445, aug 2016. ISSN 0028-0836. doi: 10.1038/nature18949. URL http://www.nature.com/articles/nature18949.

[29] Joachim Cohen, W. Clarke Smith, Michel H. Devoret, and Mazyar Mirrahimi. Degeneracy-Preserving Quantum Nondemolition Measurement of Parity-Type Observables for Cat Qubits. *Physical Review Letters*, 119(6):060503, aug 2017. ISSN 0031-9007. doi: 10.1103/PhysRevLett.119.060503. URL

http://link.aps.org/doi/10.1103/PhysRevLett.119.060503.

[30] S O Mundhada, A Grimm, S Touzard, U Vool, S Shankar, M H Devoret, and M Mirrahimi. Generating higher-order quantum dissipation from lower-order parametric processes. *Quantum Science and Technology*, 2(2):024005, jun 2017. ISSN 2058-9565. doi: 10.1088/2058-9565/aa6e9d. URL http://stacks.iop.org/2058-9565/2/i=2/a=024005?key=crossref.283b92f53abbdb9f8fc284f87f80149c.

[31] Chen Wang, Yvonne Y Gao, Philip Reinhold, R W Heeres, Nissim Ofek, Kevin Chou, Christopher Axline, Matthew Reagor, Jacob Blumoff, K M Sliwa, L Frunzio, S M Girvin, Liang Jiang, M Mirrahimi, M H Devoret, and R J Schoelkopf. A Schrödinger cat living in two boxes. *Science (New York, N.Y.)*, 352(6289):1087–91, may 2016. ISSN 1095-9203. doi: 10.1126/science.aaf2941. URL http://www.ncbi.nlm.nih.gov/pubmed/27230374.

[32] Reinier W. Heeres, Philip Reinhold, Nissim Ofek, Luigi Frunzio, Liang Jiang, Michel H. Devoret, and Robert J. Schoelkopf. Implementing a universal gate set on a logical qubit encoded in an oscillator. *Nature Communications*, 8(1):94, dec 2017. ISSN 2041-1723. doi: 10.1038/s41467-017-00045-1. URL http://www.nature.com/articles/s41467-017-00045-1.

[33] Shruti Puri, Samuel Boutin, and Alexandre Blais. Engineering the quantum states of light in a Kerr-nonlinear resonator by two-photon driving. *npj Quantum Information*, 3(1):18, dec 2017. ISSN 2056-6387. doi: 10.1038/s41534-017-0019-1. URL http://www.nature.com/articles/s41534-017-0019-1.

[34] Marios H. Michael, Matti Silveri, R. T. Brierley, Victor V. Albert, Juha Salmilehto, Liang Jiang, and S. M. Girvin. New Class of Quantum Error-Correcting Codes for a Bosonic Mode. *Physical Review X*, 6(3):031006, jul 2016. ISSN 2160-3308. doi: 10.1103/PhysRevX.6.031006. URL https://link.aps.org/doi/10.1103/PhysRevX.6.031006.

[35] Félix Beaudoin, Marcus P. Da Silva, Zachary Dutton, and Alexandre Blais. First-order sidebands in circuit QED using qubit frequency modulation. *Physical Review A - Atomic, Molecular, and Optical Physics*, 86(2):022305, aug 2012. ISSN 10502947. doi: 10.1103/PhysRevA.86.022305. URL https://journals.aps.org/pra/abstract/10.1103/PhysRevA.86.022305.

[36] J. D. Strand, Matthew Ware, Félix Beaudoin, T. A. Ohki, B. R. Johnson, Alexandre Blais, and B. L.T. Plourde. First-order sideband transitions with flux-driven asymmetric transmon qubits. *Physical Review B - Condensed Matter and Materials Physics*, 87(22):220505, jun 2013. ISSN 10980121. doi: 10.1103/PhysRevB.87.220505. URL https://journals.aps.org/prb/abstract/10.1103/PhysRevB.87.220505.

[37] Marco Roth, Marc Ganzhorn, Nikolaj Moll, Stefan Filipp, Gian Salis, and Sebastian Schmidt. Analysis of a parametrically driven exchange-type gate and a two-photon excitation gate between superconducting qubits. *Physical Review A*, 96(6):062323, dec 2017. ISSN 24699934. doi: 10.1103/PhysRevA.96.062323. URL https://journals.aps.org/pra/abstract/10.1103/PhysRevA.96.062323.

[38] A. Wallraff, D. I. Schuster, A. Blais, J. M. Gambetta, J. Schreier, L. Frunzio, M. H. Devoret, S. M. Girvin, and R. J. Schoelkopf. Sideband transitions and two-tone spectroscopy of a superconducting qubit strongly coupled to an on-chip cavity. *Physical Review Letters*, 99(5):050501, jul 2007. ISSN 00319007. doi: 10.1103/PhysRevLett.99.050501. URL https://journals.aps.org/prl/abstract/10.1103/PhysRevLett.99.050501.

[39] P. J. Leek, S. Filipp, P. Maurer, M. Baur, R. Bianchetti, J. M. Fink, M. Göppl, L. Steffen, and A. Wallraff. Using sideband transitions for two-qubit operations in superconducting circuits. *Physical Review B - Condensed Matter and Materials Physics*, 79(18):180511, may 2009. ISSN 10980121. doi: 10.1103/PhysRevB.79.180511. URL https://journals.aps.org/prb/abstract/10.1103/PhysRevB.79.180511.

[40] S. Novikov, T. Sweeney, J. E. Robinson, S. P. Premaratne, B. Suri, F. C. Wellstood, and B. S. Palmer. Raman coherence in a circuit quantum electrodynamics lambda system. *Nature Physics*, 12(1):75–79, jan 2016. ISSN 17452481. doi: 10.1038/nphys3537. URL https://www.nature.com/articles/nphys3537.

[41] Yao Lu, S. Chakram, N. Leung, N. Earnest, R. K. Naik, Ziwen Huang, Peter Groszkowski, Eliot Kapit, Jens Koch, and David I. Schuster. Universal Stabilization of a Parametrically Coupled Qubit. *Physical Review Letters*, 119(15), oct 2017. ISSN 10797114.

[42] Ziwen Huang, Yao Lu, Eliot Kapit, David I. Schuster, and Jens Koch. Universal stabilization of single-qubit states using a tunable coupler. *Physical Review A*, 97(6): 1–11, 2018. ISSN 24699934. doi: 10.1103/PhysRevA.97.062345.

[43] M. D. Reed, B. R. Johnson, A. A. Houck, L. Dicarlo, J. M. Chow, D. I. Schuster, L. Frunzio, and R. J. Schoelkopf. Fast reset and suppressing spontaneous emission of a superconducting qubit. *Applied Physics Letters*, 96(20):203110, may 2010. ISSN 00036951. doi: 10.1063/1.3435463. URL http://aip.scitation.org/doi/10.1063/1.3435463.

[44] Sergio O. Valenzuela, William D. Oliver, David M. Berns, Karl K. Berggren, Leonid S. Levitov, and Terry P. Orlando. Microwave-induced cooling of a superconducting qubit. *Science*, 314(5805):1589–1592, dec 2006. ISSN 00368075. doi: 10.1126/science.1134008.

[45] K. Geerlings, Z. Leghtas, I. M. Pop, S. Shankar, L. Frunzio, R. J. Schoelkopf, M. Mirrahimi, and M. H. Devoret. Demonstrating a driven reset protocol for a superconducting qubit. *Physical Review Letters*, 110(12):120501, mar 2013. ISSN 00319007. doi: 10.1103/PhysRevLett.110.120501.

[46] Ruichao Ma, Clai Owens, Andrew Houck, David I. Schuster, and Jonathan Simon. Autonomous stabilizer for incompressible photon fluids and solids. *Physical Review A*, 95(4), apr 2017. ISSN 24699934.

[47] Navin Khaneja, Timo Reiss, Cindie Kehlet, Thomas Schulte-Herbrüggen, and Steffen J. Glaser. Optimal control of coupled spin dynamics: Design of NMR pulse

sequences by gradient ascent algorithms. *Journal of Magnetic Resonance*, 172(2): 296–305, feb 2005. ISSN 10907807. doi: 10.1016/j.jmr.2004.11.004.

[48] F. Motzoi, J. M. Gambetta, P. Rebentrost, and F. K. Wilhelm. Simple Pulses for Elimination of Leakage in Weakly Nonlinear Qubits. *Physical Review Letters*, 103 (11), sep 2009. ISSN 00319007.

[49] Mikko Möttönen, Rogerio De Sousa, Jun Zhang, and K Birgitta Whaley. High-fidelity one-qubit operations under random telegraph noise. *Physical Review A - Atomic, Molecular, and Optical Physics*, 73(2), 2006. ISSN 10941622.

[50] Matthias Steffen, John M Martinis, and Isaac L Chuang. Accurate control of Josephson phase qubits. *Physical Review B - Condensed Matter and Materials Physics*, 68(22), 2003. ISSN 1550235X.

[51] Shabnam Safaei, Simone Montangero, Fabio Taddei, and Rosario Fazio. Optimized single-qubit gates for Josephson phase qubits. *Physical Review B - Condensed Matter and Materials Physics*, 79(6):064524, feb 2009. ISSN 10980121. doi: 10.1103/PhysRevB.79.064524. URL https://journals.aps.org/prb/abstract/10.1103/PhysRevB.79.064524.

[52] Marco A Pravia, Nicolas Boulant, Joseph Emerson, Amro Farid, Evan M Fortunato, Timothy F Havel, R Martinez, and David G Cory. Incoherent noise and quantum information processing. *Quantum Computation and Quantum Information American Journal of Physics*, 119:558, 2003. doi: 10.1063/1.1619132. URL https://doi.org/10.1063/1.1619132.

[53] Eliot Kapit. Error-Transparent Quantum Gates for Small Logical Qubit Architectures. *Physical Review Letters*, 120(5):50503, 2018. ISSN 1079-7114. doi: 10.1103/PhysRevLett.120.050503. URL https://doi.org/10.1103/PhysRevLett.120.050503.

[54] Austin G. Fowler, Matteo Mariantoni, John M. Martinis, and Andrew N. Cleland. Surface codes: Towards practical large-scale quantum computation. *Physical Review A - Atomic, Molecular, and Optical Physics*, 86(3), September 2012. doi: 10.1103/PhysRevA.86.032324.

[55] Barbara M. Terhal. Quantum error correction for quantum memories. *Reviews of Modern Physics*, 87(2):307–346, April 2015. doi: 10.1103/RevModPhys.87.307. URL https://link.aps.org/doi/10.1103/RevModPhys.87.307. Publisher: American Physical Society.

[56] R. Barends, J. Kelly, A. Megrant, A. Veitia, D. Sank, E. Jeffrey, T. C. White, J. Mutus, A. G. Fowler, B. Campbell, Y. Chen, Z. Chen, B. Chiaro, A. Dunsworth, C. Neill, P. O'Malley, P. Roushan, A. Vainsencher, J. Wenner, A. N. Korotkov, A. N. Cleland, and John M. Martinis. Superconducting quantum circuits at the surface code threshold for fault tolerance. *Nature*, 508(7497):500–503, April 2014. ISSN 1476-4687. doi: 10.1038/nature13171. URL https://www.nature.com/articles/nature13171. Number: 7497 Publisher: Nature Publishing Group.

[57] John Preskill. Quantum Computing in the NISQ era and beyond. *Quantum*, 2:79, August 2018. doi: 10.22331/q-2018-08-06-79. URL https://quantum-journal.org/papers/q-2018-08-06-79/. Publisher: Verein zur Förderung des Open Access Publizierens in den Quantenwissenschaften.

[58] Frank Arute, Kunal Arya, Ryan Babbush, Dave Bacon, Joseph C. Bardin, Rami Barends, Rupak Biswas, Sergio Boixo, Fernando G. S. L. Brandao, David A. Buell, Brian Burkett, Yu Chen, Zijun Chen, Ben Chiaro, Roberto Collins, William Courtney, Andrew Dunsworth, Edward Farhi, Brooks Foxen, Austin Fowler, Craig Gidney, Marissa Giustina, Rob Graff, Keith Guerin, Steve Habegger, Matthew P. Harrigan, Michael J. Hartmann, Alan Ho, Markus Hoffmann, Trent Huang, Travis S. Humble, Sergei V. Isakov, Evan Jeffrey, Zhang Jiang, Dvir Kafri, Kostyantyn Kechedzhi, Julian Kelly, Paul V. Klimov, Sergey Knysh, Alexander Korotkov, Fedor Kostritsa, David Landhuis, Mike Lindmark, Erik Lucero, Dmitry Lyakh, Salvatore Mandrà, Jarrod R. McClean, Matthew McEwen, Anthony Megrant, Xiao Mi, Kristel Michielsen, Masoud Mohseni, Josh Mutus, Ofer Naaman, Matthew Neeley, Charles Neill, Murphy Yuezhen Niu, Eric Ostby, Andre Petukhov, John C. Platt, Chris Quintana, Eleanor G. Rieffel, Pedram Roushan, Nicholas C. Rubin, Daniel Sank, Kevin J. Satzinger, Vadim Smelyanskiy, Kevin J. Sung, Matthew D. Trevithick, Amit Vainsencher, Benjamin Villalonga, Theodore White, Z. Jamie Yao, Ping Yeh, Adam Zalcman, Hartmut Neven, and John M. Martinis. Quantum supremacy using a programmable superconducting processor. *Nature*, 574(7779):505–510, October 2019. ISSN 1476-4687. doi: 10.1038/s41586-019-1666-5. URL https://www.nature.com/articles/s41586-019-1666-5. Number: 7779 Publisher: Nature Publishing Group.

[59] Edward Farhi, Jeffrey Goldstone, and Sam Gutmann. A Quantum Approximate Optimization Algorithm. *arXiv:1411.4028 [quant-ph]*, November 2014. URL http://arxiv.org/abs/1411.4028. arXiv: 1411.4028.

[60] Matthew P. Harrigan, Kevin J. Sung, Matthew Neeley, Kevin J. Satzinger, Frank Arute, Kunal Arya, Juan Atalaya, Joseph C. Bardin, Rami Barends, Sergio Boixo, Michael Broughton, Bob B. Buckley, David A. Buell, Brian Burkett, Nicholas Bushnell, Yu Chen, Zijun Chen, Ben Chiaro, Roberto Collins, William Courtney, Sean Demura, Andrew Dunsworth, Daniel Eppens, Austin Fowler, Brooks Foxen, Craig Gidney, Marissa Giustina, Rob Graff, Steve Habegger, Alan Ho, Sabrina Hong, Trent Huang, L. B. Ioffe, Sergei V. Isakov, Evan Jeffrey, Zhang Jiang, Cody Jones, Dvir Kafri, Kostyantyn Kechedzhi, Julian Kelly, Seon Kim, Paul V. Klimov, Alexander N. Korotkov, Fedor Kostritsa, David Landhuis, Pavel Laptev, Mike Lindmark, Martin Leib, Orion Martin, John M. Martinis, Jarrod R. McClean, Matt McEwen, Anthony Megrant, Xiao Mi, Masoud Mohseni, Wojciech Mruczkiewicz, Josh Mutus, Ofer Naaman, Charles Neill, Florian Neukart, Murphy Yuezhen Niu, Thomas E. O'Brien, Bryan O'Gorman, Eric Ostby, Andre Petukhov, Harald Putterman, Chris Quintana, Pedram Roushan, Nicholas C. Rubin, Daniel Sank, Andrea Skolik, Vadim Smelyanskiy, Doug Strain, Michael Streif, Marco Szalay, Amit Vainsencher, Theodore White, Z. Jamie Yao, Ping Yeh, Adam Zalcman, Leo Zhou, Hartmut Neven, Dave Bacon, Erik Lucero, Edward Farhi, and Ryan Babbush.

Quantum approximate optimization of non-planar graph problems on a planar superconducting processor. *Nature Physics*, 17(3):332–336, March 2021. ISSN 1745-2481. doi: 10.1038/s41567-020-01105-y. URL https://www.nature.com/articles/s41567-020-01105-y. Number: 3 Publisher: Nature Publishing Group.

[61] Alberto Peruzzo, Jarrod McClean, Peter Shadbolt, Man-Hong Yung, Xiao-Qi Zhou, Peter J. Love, Alán Aspuru-Guzik, and Jeremy L. O'Brien. A variational eigenvalue solver on a photonic quantum processor. *Nature Communications*, 5(1):4213, July 2014. ISSN 2041-1723. doi: 10.1038/ncomms5213. URL https://www.nature.com/articles/ncomms5213. Number: 1 Publisher: Nature Publishing Group.

[62] Jarrod R. McClean, Jonathan Romero, Ryan Babbush, and Alán Aspuru-Guzik. The theory of variational hybrid quantum-classical algorithms. *New Journal of Physics*, 18(2):023023, February 2016. ISSN 1367-2630. doi: 10.1088/1367-2630/18/2/023023. URL https://doi.org/10.1088/1367-2630/18/2/023023. Publisher: IOP Publishing.

[63] J. Majer, J. M. Chow, J. M. Gambetta, Jens Koch, B. R. Johnson, J. A. Schreier, L. Frunzio, D. I. Schuster, A. A. Houck, A. Wallraff, A. Blais, M. H. Devoret, S. M. Girvin, and R. J. Schoelkopf. Coupling superconducting qubits via a cavity bus. *Nature*, 449(7161):443–447, September 2007. ISSN 1476-4687. doi: 10.1038/nature06184. URL https://www.nature.com/articles/nature06184. Number: 7161 Publisher: Nature Publishing Group.

[64] Fei Yan, Philip Krantz, Youngkyu Sung, Morten Kjaergaard, Daniel L. Campbell, Terry P. Orlando, Simon Gustavsson, and William D. Oliver. Tunable Coupling Scheme for Implementing High-Fidelity Two-Qubit Gates. *Physical Review Applied*, 10(5):054062, November 2018. doi: 10.1103/PhysRevApplied.10.054062. URL https://link.aps.org/doi/10.1103/PhysRevApplied.10.054062. Publisher: American Physical Society.

[65] Yuan Xu, Ji Chu, Jiahao Yuan, Jiawei Qiu, Yuxuan Zhou, Libo Zhang, Xinsheng Tan, Yang Yu, Song Liu, Jian Li, Fei Yan, and Dapeng Yu. High-Fidelity, High-Scalability Two-Qubit Gate Scheme for Superconducting Qubits. *Physical Review Letters*, 125(24):240503, December 2020. doi: 10.1103/PhysRevLett.125.240503. URL https://link.aps.org/doi/10.1103/PhysRevLett.125.240503. Publisher: American Physical Society.

[66] Peng Zhao, Peng Xu, Dong Lan, Xinsheng Tan, Haifeng Yu, and Yang Yu. Switchable Next-Nearest-Neighbor Coupling for Controlled Two-Qubit Operations. *Physical Review Applied*, 14(6):064016, December 2020. doi: 10.1103/PhysRevApplied.14.064016. URL https://link.aps.org/doi/10.1103/PhysRevApplied.14.064016. Publisher: American Physical Society.

[67] Michele C. Collodo, Johannes Herrmann, Nathan Lacroix, Christian Kraglund

Andersen, Ants Remm, Stefania Lazar, Jean-Claude Besse, Theo Walter, Andreas Wallraff, and Christopher Eichler. Implementation of Conditional Phase Gates Based on Tunable ZZ Interactions. *Physical Review Letters*, 125(24):240502, December 2020. doi: 10.1103/PhysRevLett.125.240502. URL https://link.aps.org/doi/10.1103/PhysRevLett.125.240502. Publisher: American Physical Society.

[68] S. E. Rasmussen and N. T. Zinner. Simple implementation of high fidelity controlled-$i$swap gates and quantum circuit exponentiation of non-Hermitian gates. *Physical Review Research*, 2(3):033097, July 2020. doi: 10.1103/PhysRevResearch.2.033097. URL https://link.aps.org/doi/10.1103/PhysRevResearch.2.033097. Publisher: American Physical Society.

[69] Navin Khaneja and Steffen J. Glaser. Cartan decomposition of SU(2n) and control of spin systems. *Chemical Physics*, 267(1):11–23, June 2001. ISSN 0301-0104. doi: 10.1016/S0301-0104(01)00318-4. URL https://www.sciencedirect.com/science/article/pii/S0301010401003184.

[70] B. Foxen, C. Neill, A. Dunsworth, P. Roushan, B. Chiaro, A. Megrant, J. Kelly, Zijun Chen, K. Satzinger, R. Barends, F. Arute, K. Arya, R. Babbush, D. Bacon, J. C. Bardin, S. Boixo, D. Buell, B. Burkett, Yu Chen, R. Collins, E. Farhi, A. Fowler, C. Gidney, M. Giustina, R. Graff, M. Harrigan, T. Huang, S. V. Isakov, E. Jeffrey, Z. Jiang, D. Kafri, K. Kechedzhi, P. Klimov, A. Korotkov, F. Kostritsa, D. Landhuis, E. Lucero, J. McClean, M. McEwen, X. Mi, M. Mohseni, J. Y. Mutus, O. Naaman, M. Neeley, M. Niu, A. Petukhov, C. Quintana, N. Rubin, D. Sank, V. Smelyanskiy, A. Vainsencher, T. C. White, Z. Yao, P. Yeh, A. Zalcman, H. Neven, and J. M. Martinis. Demonstrating a Continuous Set of Two-Qubit Gates for Near-Term Quantum Algorithms. *Physical Review Letters*, 125(12):120504, September 2020. doi: 10.1103/PhysRevLett.125.120504. URL https://link.aps.org/doi/10.1103/PhysRevLett.125.120504. Publisher: American Physical Society.

[71] Deanna M. Abrams, Nicolas Didier, Blake R. Johnson, Marcus P.da Silva, and Colm A. Ryan. Implementation of XY entangling gates with a single calibrated pulse. *Nature Electronics*, 3(12):744–750, December 2020. doi: 10.1038/s41928-020-00498-1. URL https://www.nature.com/articles/s41928-020-00498-1. Publisher: Nature Research.

[72] Eric C. Peterson, Gavin E. Crooks, and Robert S. Smith. Fixed-Depth Two-Qubit Circuits and the Monodromy Polytope. *Quantum*, 4:247, March 2020. doi: 10.22331/q-2020-03-26-247. URL https://quantum-journal.org/papers/q-2020-03-26-247/. Publisher: Verein zur Förderung des Open Access Publizierens in den Quantenwissenschaften.

[73] Haonan Xiong, Quentin Ficheux, Aaron Somoroff, Long B Nguyen, Ebru Dogan, Dario Rosenstock, Chen Wang, Konstantin N Nesterov, Maxim G Vavilov, and Vladimir E Manucharyan. Arbitrary controlled-phase gate on fluxonium qubits using

differential ac-Stark shifts. Technical report, 2021.

[74] Yu Chen, C. Neill, P. Roushan, N. Leung, M. Fang, R. Barends, J. Kelly, B. Campbell, Z. Chen, B. Chiaro, A. Dunsworth, E. Jeffrey, A. Megrant, J. Y. Mutus, P. J. J. O'Malley, C. M. Quintana, D. Sank, A. Vainsencher, J. Wenner, T. C. White, Michael R. Geller, A. N. Cleland, and John M. Martinis. Qubit Architecture with High Coherence and Fast Tunable Coupling. *Physical Review Letters*, 113(22):220502, November 2014. doi: 10.1103/PhysRevLett.113.220502. URL https://link.aps.org/doi/10.1103/PhysRevLett.113.220502. Publisher: American Physical Society.

[75] Eliot Kapit. Error-Transparent Quantum Gates for Small Logical Qubit Architectures. *Physical Review Letters*, 120(5):50503–50503, 2018. doi: 10.1103/PhysRevLett.120.050503. URL https://doi.org/10.1103/PhysRevLett.120.050503. Publisher: American Physical Society.

[76] Robert Feldt. robertfeldt/BlackBoxOptim.jl, June 2021. URL https://github.com/robertfeldt/BlackBoxOptim.jl. original-date: 2013-10-28T05:23:11Z.

[77] F. Motzoi, J. M. Gambetta, P. Rebentrost, and F. K. Wilhelm. Simple Pulses for Elimination of Leakage in Weakly Nonlinear Qubits. *Physical Review Letters*, 103 (11), September 2009. doi: 10.1103/PhysRevLett.103.110501.

[78] Mikko Möttönen, Rogerio De Sousa, Jun Zhang, and K Birgitta Whaley. High-fidelity one-qubit operations under random telegraph noise. *Physical Review A - Atomic, Molecular, and Optical Physics*, 73(2), 2006. doi: 10.1103/PhysRevA.73.022332.

[79] Shabnam Safaei, Simone Montangero, Fabio Taddei, and Rosario Fazio. Optimized single-qubit gates for Josephson phase qubits. *Physical Review B - Condensed Matter and Materials Physics*, 79(6):064524–064524, February 2009. doi: 10.1103/PhysRevB.79.064524. URL https://journals.aps.org/prb/abstract/10.1103/PhysRevB.79.064524. Publisher: American Physical Society.

[80] Matthias Steffen, John M Martinis, and Isaac L Chuang. Accurate control of Josephson phase qubits. *Physical Review B - Condensed Matter and Materials Physics*, 68(22), 2003. doi: 10.1103/PhysRevB.68.224518.

[81] Pranav Mundada, Gengyan Zhang, Thomas Hazard, and Andrew Houck. Suppression of Qubit Crosstalk in a Tunable Coupling Superconducting Circuit. *Physical Review Applied*, 12(5):054023, November 2019. ISSN 2331-7019. doi: 10.1103/PhysRevApplied.12.054023. URL https://link.aps.org/doi/10.1103/PhysRevApplied.12.054023.

[82] Sarah Sheldon, Easwar Magesan, Jerry M. Chow, and Jay M. Gambetta. Procedure for systematically tuning up cross-talk in the cross-resonance gate. *Physical Review A*, 93(6):060302, June 2016. ISSN 2469-9926, 2469-9934. doi:

10.1103/PhysRevA.93.060302. URL https://link.aps.org/doi/10.1103/PhysRevA.93.060302.

[83] Adam Winick, Joel J. Wallman, and Joseph Emerson. Simulating and mitigating crosstalk. *arXiv:2006.09596 [quant-ph]*, June 2020. URL http://arxiv.org/abs/2006.09596. arXiv: 2006.09596.

[84] Shai Machnes, Elie Assémat, David Tannor, and Frank K. Wilhelm. Tunable, Flexible, and Efficient Optimization of Control Pulses for Practical Qubits. *Physical Review Letters*, 120(15):150401, April 2018. doi: 10.1103/PhysRevLett.120.150401. URL https://link.aps.org/doi/10.1103/PhysRevLett.120.150401. Publisher: American Physical Society.

[85] J. Stehlik, D. M. Zajac, D. L. Underwood, T. Phung, J. Blair, S. Carnevale, D. Klaus, G. A. Keefe, A. Carniol, M. Kumph, Matthias Steffen, and O. E. Dial. Tunable Coupling Architecture for Fixed-frequency Transmons. *arXiv:2101.07746 [quant-ph]*, January 2021. URL http://arxiv.org/abs/2101.07746. arXiv: 2101.07746.

[86] X. Dai, D. M. Tennant, R. Trappen, A. J. Martinez, D. Melanson, M. A. Yurtalan, Y. Tang, S. Novikov, J. A. Grover, S. M. Disseler, J. I. Basham, R. Das, D. K. Kim, A. J. Melville, B. M. Niedzielski, S. J. Weber, J. L. Yoder, D. A. Lidar, and A. Lupascu. Calibration of flux crosstalk in large-scale flux-tunable superconducting quantum circuits. *arXiv:2105.14360 [quant-ph]*, May 2021. URL http://arxiv.org/abs/2105.14360. arXiv: 2105.14360.

[87] L. DiCarlo, J. M. Chow, J. M. Gambetta, Lev S. Bishop, B. R. Johnson, D. I. Schuster, J. Majer, A. Blais, L. Frunzio, S. M. Girvin, and R. J. Schoelkopf. Demonstration of two-qubit algorithms with a superconducting quantum processor. *Nature*, 460(7252):240–244, July 2009. ISSN 1476-4687. doi: 10.1038/nature08121. URL https://www.nature.com/articles/nature08121. Number: 7252 Publisher: Nature Publishing Group.

[88] R. Barends, J. Kelly, A. Megrant, D. Sank, E. Jeffrey, Y. Chen, Y. Yin, B. Chiaro, J. Mutus, C. Neill, P. O'Malley, P. Roushan, J. Wenner, T. C. White, A. N. Cleland, and John M. Martinis. Coherent Josephson Qubit Suitable for Scalable Quantum Integrated Circuits. *Physical Review Letters*, 111(8):080502, August 2013. doi: 10.1103/PhysRevLett.111.080502. URL https://link.aps.org/doi/10.1103/PhysRevLett.111.080502. Publisher: American Physical Society.

[89] G. S. Paraoanu. Microwave-induced coupling of superconducting qubits. *Physical Review B*, 74(14):140504, October 2006. doi: 10.1103/PhysRevB.74.140504. URL https://link.aps.org/doi/10.1103/PhysRevB.74.140504. Publisher: American Physical Society.

[90] Moein Malekakhlagh, Easwar Magesan, and David C. McKay. First-principles analysis of cross-resonance gate operation. *Physical Review A*, 102(4):042605, October 2020. doi: 10.1103/PhysRevA.102.042605. URL https://link.aps.org/doi/10.1103/PhysRevA.102.042605. Publisher: American

Physical Society.

[91] Chad Rigetti and Michel Devoret. Fully microwave-tunable universal gates in superconducting qubits with linear couplings and fixed transition frequencies. *Physical Review B*, 81(13):134507, April 2010. doi: 10.1103/PhysRevB.81.134507. URL https://link.aps.org/doi/10.1103/PhysRevB.81.134507. Publisher: American Physical Society.

[92] Easwar Magesan and Jay M. Gambetta. Effective Hamiltonian models of the cross-resonance gate. *Physical Review A*, 101(5):052308, May 2020. doi: 10.1103/PhysRevA.101.052308. URL https://link.aps.org/doi/10.1103/PhysRevA.101.052308. Publisher: American Physical Society.

[93] David C. McKay, Stefan Filipp, Antonio Mezzacapo, Easwar Magesan, Jerry M. Chow, and Jay M. Gambetta. Universal Gate for Fixed-Frequency Qubits via a Tunable Bus. *Physical Review Applied*, 6(6):064007, December 2016. doi: 10.1103/PhysRevApplied.6.064007. URL https://link.aps.org/doi/10.1103/PhysRevApplied.6.064007. Publisher: American Physical Society.

[94] S. A. Caldwell, N. Didier, C. A. Ryan, E. A. Sete, A. Hudson, P. Karalekas, R. Manenti, M. P. da Silva, R. Sinclair, E. Acala, N. Alidoust, J. Angeles, A. Bestwick, M. Block, B. Bloom, A. Bradley, C. Bui, L. Capelluto, R. Chilcott, J. Cordova, G. Crossman, M. Curtis, S. Deshpande, T. El Bouayadi, D. Girshovich, S. Hong, K. Kuang, M. Lenihan, T. Manning, A. Marchenkov, J. Marshall, R. Maydra, Y. Mohan, W. O'Brien, C. Osborn, J. Otterbach, A. Papageorge, J.-P. Paquette, M. Pelstring, A. Polloreno, G. Prawiroatmodjo, V. Rawat, M. Reagor, R. Renzas, N. Rubin, D. Russell, M. Rust, D. Scarabelli, M. Scheer, M. Selvanayagam, R. Smith, A. Staley, M. Suska, N. Tezak, D. C. Thompson, T.-W. To, M. Vahidpour, N. Vodrahalli, T. Whyland, K. Yadav, W. Zeng, and C. Rigetti. Parametrically Activated Entangling Gates Using Transmon Qubits. *Physical Review Applied*, 10(3):034050, September 2018. doi: 10.1103/PhysRevApplied.10.034050. URL https://link.aps.org/doi/10.1103/PhysRevApplied.10.034050. Publisher: American Physical Society.

[95] T. P. Orlando, J. E. Mooij, Lin Tian, Caspar H. van der Wal, L. S. Levitov, Seth Lloyd, and J. J. Mazo. Superconducting persistent-current qubit. *Physical Review B*, 60(22):15398–15413, December 1999. doi: 10.1103/PhysRevB.60.15398. URL https://link.aps.org/doi/10.1103/PhysRevB.60.15398. Publisher: American Physical Society.

[96] J. E. Mooij, T. P. Orlando, L. Levitov, Lin Tian, Caspar H. van der Wal, and Seth Lloyd. Josephson Persistent-Current Qubit. *Science*, 285(5430):1036–1039, August 1999. doi: 10.1126/science.285.5430.1036. URL https://www.science.org/doi/10.1126/science.285.5430.1036. Publisher: American Association for the Advancement of Science.

[97] Long B. Nguyen, Yen-Hsiang Lin, Aaron Somoroff, Raymond Mencia, Nicholas Grabon, and Vladimir E. Manucharyan. High-Coherence Fluxonium Qubit. *Physical Review X*, 9(4):041041, November 2019. doi: 10.1103/PhysRevX.9.041041. URL https://link.aps.org/doi/10.1103/PhysRevX.9.041041. Publisher: American Physical Society.

[98] Ioan M. Pop, Kurtis Geerlings, Gianluigi Catelani, Robert J. Schoelkopf, Leonid I. Glazman, and Michel H. Devoret. Coherent suppression of electromagnetic dissipation due to superconducting quasiparticles. *Nature*, 508(7496):369–372, April 2014. ISSN 0028-0836, 1476-4687. doi: 10.1038/nature13017. URL http://www.nature.com/articles/nature13017.

[99] Vladimir E. Manucharyan, Jens Koch, Leonid I. Glazman, and Michel H. Devoret. Fluxonium: Single Cooper-Pair Circuit Free of Charge Offsets. *Science*, 326(5949): 113–116, October 2009. ISSN 0036-8075, 1095-9203. doi: 10.1126/science.1175552. URL https://www.science.org/doi/10.1126/science.1175552.

[100] Naomichi Hatano and Masuo Suzuki. Finding Exponential Product Formulas of Higher Orders. In R. Beig, W. Beiglböck, W. Domcke, B.-G. Englert, U. Frisch, P. Hänggi, G. Hasinger, K. Hepp, W. Hillebrandt, D. Imboden, R. L. Jaffe, R. Lipowsky, H. v. Löhneysen, I. Ojima, D. Sornette, S. Theisen, W. Weise, J. Wess, J. Zittartz, Arnab Das, and Bikas K. Chakrabarti, editors, *Quantum Annealing and Other Optimization Methods*, volume 679, pages 37–68. Springer Berlin Heidelberg, Berlin, Heidelberg, November 2005. ISBN 978-3-540-27987-7 978-3-540-31515-5. doi: 10.1007/11526216_2. URL http://link.springer.com/10.1007/11526216_2. Series Title: Lecture Notes in Physics.

[101] P. Kaelo and M. M. Ali. Some Variants of the Controlled Random Search Algorithm for Global Optimization. *Journal of Optimization Theory and Applications*, 130(2): 253–264, August 2006. ISSN 1573-2878. doi: 10.1007/s10957-006-9101-0. URL https://doi.org/10.1007/s10957-006-9101-0.

[102] Steven G. Johnson. stevengj/nlopt, July 2021. URL https://github.com/stevengj/nlopt. original-date: 2013-08-27T16:59:11Z.

[103] Tyson Jones, Anna Brown, Ian Bush, and Simon C. Benjamin. QuEST and High Performance Simulation of Quantum Computers. *Scientific Reports*, 9(1):10736, July 2019. ISSN 2045-2322. doi: 10.1038/s41598-019-47174-9. URL https://www.nature.com/articles/s41598-019-47174-9. Number: 1 Publisher: Nature Publishing Group.

[104] A. V. Lebedev, G. B. Lesovik, V. M. Vinokur, and G. Blatter. Extended quantum Maxwell demon acting over macroscopic distances. *Physical Review B*, 98(21):214502, December 2018. ISSN 2469-9950, 2469-9969. doi: 10.1103/PhysRevB.98.214502. URL https://link.aps.org/doi/10.1103/PhysRevB.98.214502.

APPENDIX A

MASTER EQUATION SIMULATOR FOR GENERAL STATES AND HAMILTONIANS

The following code can be found on my GitHub: github.com/Bebotron/myModules, in the file `QuantumSimulations.jl`. The source code at the time of writing is below.

```
# QuantumSimulations.jl

module QuantumSimulations
   import LinearAlgebra
   export tensor
   export meEvolveState
   export tpEvolveState

   tensor(first, args...) = LinearAlgebra.kron(first, tensor(args...))
   function tensor(arg)
      if ndims(arg[1]) == 0
         output = arg
      else
         output = LinearAlgebra.kron(arg[1], arg[2])
         for i in 3:size(arg,1)
            output = LinearAlgebra.kron(output, arg[i])
         end
      end
      return output
   end

   timePropagator(dt, H, psi) = -im*dt*H*psi

   function tpRK4(dt, H, psi)
      k1 = timePropagator(dt, H, psi)
      k2 = timePropagator(dt, H, psi + 0.5*k1)
      k3 = timePropagator(dt, H, psi + 0.5*k2)
      k4 = timePropagator(dt, H, psi + k3)
      psi += (k1 + 2*k2 + 2*k3 + k4)/6
      return psi
   end

   function lindbladME(H, rho, collapse, coeff)
      newrho = im*(rho*H - H*rho)
      for i in 1:size(coeff,1)
         newrho += coeff[i]*(collapse[i]*rho*collapse[i]' - 0.5*(collapse[i]'
    collapse[i]*rho + rho*collapse[i]'collapse[i]))
      end
      return newrho
```

```
end

function meRK4(dt, H, rho, collapse, coeff)
   k1 = lindbladME(H, rho, collapse, coeff)
   k2 = lindbladME(H, rho + k1*dt*0.5, collapse, coeff)
   k3 = lindbladME(H, rho + k2*dt*0.5, collapse, coeff)
   k4 = lindbladME(H, rho + k3*dt, collapse, coeff)
   rho += dt*(k1 + 2*(k2 + k3) + k4)/6
   return rho
end

function meEvolveState(initialState, target, H0, collapse, fCOp, Ht, fHam,
tvec, timedep)
   dt = tvec[2] - tvec[1]
   dataList = zeros(length(target)*length(initialState) + 1, length(tvec))
   currentState = copy(initialState)
   coeff = zeros(length(collapse))
   Hinit = copy(H0)
   if !timedep
      for i in 1:size(fCOp,1) coeff[i] = fCOp[i] end
      for i in 1:size(fHam,1) Hinit += fHam[i]*Ht[i] end
   end
   for i in 1:length(tvec)
      H = Hinit;
      if timedep
         for j in 1:size(fCOp,1) coeff[j] = fCOp[j, i] end
         for j in 1:size(fHam,1) H += fHam[j, i]*Ht[j] end
      end
      dataList[1, i] = tvec[i]
      for k in 1:length(initialState)
         for j in 1:length(target)
            dataList[(k - 1)*length(target) + j + 1, i] = real(
LinearAlgebra.tr(target[j]*currentState[k]'))
         end
         currentState[k] = meRK4(dt, H, currentState[k], collapse, coeff)
      end
   end
   return dataList
end

function tpEvolveState(initialState, H0, target, Ht, fHam, tvec)
   dt = tvec[2] - tvec[1]
   dataList = zeros(length(target)*length(initialState) + 1, length(tvec))
   currentState = copy(initialState)
   for i in 1:length(tvec)
```

```
82          H = H0
83          for j in 1:size(fHam,1)
84             H += fHam[j, i]*Ht[j]
85          end
86          dataList[1, i] = tvec[i]
87          for k in 1:length(initialState)
88             for j in 1:length(target)
89                dataList[(k - 1)*length(target) + j + 1, i] = abs(target[j]'
   currentState[k])^2
90             end
91             currentState[k] = LinearAlgebra.normalize(tpRK4(dt, H,
   currentState[k]))
92          end
93       end
94       return dataList
95    end
96
97 end
```

APPENDIX B

SURFACE CODE MEASURE-CYCLE EXAMPLE

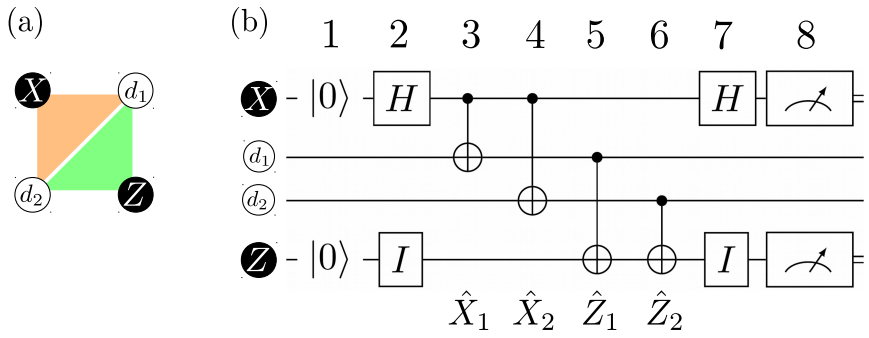

Figure B.1: Simplified example of a surface code cycle projecting to the quiescent state and detecting physical qubit errors. (a) To keep this example manageable, only two data qubits and two stabilizer qubits are considered. (b) The cycle composed of pieces from figure 1.3(b) and (c), where the X-stabilizer cycle uses the stabilizer qubit as the control, and the Z-stabilizer cycle uses the Z-stabilizer as the target.

Below is an example of what a surface code measurement cycle looks like to help illustrate the idea introduced in section 1.2.1 of what the quiescent state is, how the measurement cycle leaves it unchanged, and how it detects errors. This follows the appendix example in [6], where instead of denoting the ground and excited states as $|g\rangle$ and $|e\rangle$, respectively, we denote them as the computational basis $\{|0\rangle, |1\rangle\}$ for consistency with the rest of the thesis. The example considers only two data qubits (a and b), and two stabilizer qubits (one X and one Z) for simplicity, as shown in figure B.1. The state of this system is denoted $|\psi_n\rangle = |q_X q_a q_b q_Z\rangle$, with n following the numbered steps in figure B.1. Starting with $|\psi_1\rangle$ ins step 1, where the data qubits can start in any arbitrary state and the stabilizer qubits are set to ground, we have

$$\begin{aligned} |\psi_1\rangle &= |0\rangle \otimes (A\,|00\rangle + B\,|01\rangle + C\,|10\rangle + D\,|11\rangle) \otimes |0\rangle \\ &= A\,|0000\rangle + B\,|0010\rangle + C\,|0100\rangle + D\,|0110\rangle\,, \end{aligned} \tag{B.1}$$

where A, B, C, D are arbitrary probability amplitudes and we ignore normalization for clarity. Step 2 applies a Hadamard to the X-stabilizer, where $H\,|0\rangle = |+\rangle = |0\rangle + |1\rangle$ and

$H|1\rangle = |-\rangle = |0\rangle - |1\rangle$ (again, ignoring normalization), we get

$$\begin{aligned} |\psi_2\rangle = H_X |\psi_1\rangle &= (|0\rangle + |1\rangle) \otimes (A|00\rangle + B|01\rangle + C|10\rangle + D|11\rangle) \otimes |0\rangle \\ &= A|0000\rangle + A|1000\rangle + B|0010\rangle + B|1010\rangle \\ &\quad + C|0100\rangle + C|1100\rangle + D|0110\rangle + D|1110\rangle . \end{aligned} \tag{B.2}$$

A CNOT flips the state of the target based on the value of the control qubit. For step 3, with the X-stabilizer as a control qubit a as a target ($|0q\rangle \to |0q\rangle, |1q\rangle \to |1\bar{q}\rangle$), we get

$$\begin{aligned} |\psi_3\rangle = \mathrm{CNOT}_{X,a} |\psi_2\rangle &= A|0000\rangle + A|1100\rangle + B|0010\rangle + B|1110\rangle \\ &\quad + C|0100\rangle + C|1000\rangle + D|0110\rangle + D|1010\rangle . \end{aligned} \tag{B.3}$$

Steps 4, 5, and 6 follow a similar operation, with the noted difference that step 4 is like 3 in which the X-stabilizer is the control qubit, and in steps 5 and 6, the data qubits are the control qubits and the Z-stabilizer is the target. The operations give us

$$\begin{aligned} |\psi_4\rangle = \mathrm{CNOT}_{X,b} |\psi_3\rangle &= A|0000\rangle + A|1110\rangle + B|0010\rangle + B|1100\rangle \\ &\quad + C|0100\rangle + C|1010\rangle + D|0110\rangle + D|1000\rangle \end{aligned} \tag{B.4a}$$

$$\begin{aligned} |\psi_5\rangle = \mathrm{CNOT}_{a,Z} |\psi_4\rangle &= A|0000\rangle + A|1111\rangle + B|0010\rangle + B|1101\rangle \\ &\quad + C|0101\rangle + C|1010\rangle + D|0111\rangle + D|1000\rangle \end{aligned} \tag{B.4b}$$

$$\begin{aligned} |\psi_6\rangle = \mathrm{CNOT}_{b,Z} |\psi_5\rangle &= A|0000\rangle + A|1110\rangle + B|0011\rangle + B|1101\rangle \\ &\quad + C|0101\rangle + C|1011\rangle + D|0110\rangle + D|1000\rangle \end{aligned} \tag{B.4c}$$

where the last step before measuring doing another Hadamard on the X-syndrome,

$$\begin{aligned}
|\psi_7\rangle = H_X\,|\psi_6\rangle &= A\,|{+}000\rangle + A\,|{-}110\rangle + B\,|{+}011\rangle + B\,|{-}101\rangle \\
&\quad + C\,|{+}101\rangle + C\,|{-}011\rangle + D\,|{+}110\rangle + D\,|{-}000\rangle \\
&= A(|0000\rangle + |1000\rangle + |0110\rangle - |1110\rangle) + B(|0011\rangle + |1011\rangle + |0101\rangle - |1101\rangle) \\
&\quad + C(|0101\rangle + |1101\rangle + |0011\rangle - |1011\rangle) + D(|0110\rangle + |1110\rangle + |0000\rangle - |1000\rangle) \\
&= A\big[|0\rangle\,(|00\rangle + |11\rangle)\,|0\rangle + |1\rangle\,(|00\rangle - |11\rangle)\,|0\rangle\big] \\
&\quad + B\big[|0\rangle\,(|01\rangle + |10\rangle)\,|1\rangle + |1\rangle\,(|01\rangle - |10\rangle)\,|1\rangle\big] \\
&\quad + C\big[|0\rangle\,(|10\rangle + |01\rangle)\,|1\rangle + |1\rangle\,(|10\rangle - |01\rangle)\,|1\rangle\big] \\
&\quad + D\big[|0\rangle\,(|11\rangle + |00\rangle)\,|0\rangle + |1\rangle\,(|11\rangle - |00\rangle)\,|0\rangle\big] \\
&= (A+D)\,|0\rangle\,(|00\rangle + |11\rangle)\,|0\rangle + (A-D)\,|1\rangle\,(|00\rangle - |11\rangle)\,|0\rangle \\
&\quad + (B+C)\,|0\rangle\,(|01\rangle + |10\rangle)\,|1\rangle + (B-C)\,|1\rangle\,(|01\rangle - |10\rangle)\,|1\rangle\,.
\end{aligned} \tag{B.5}$$

Separating the stabilizer qubit kets from the data qubit Bell states not only helps simplify this expression, but also visually conveys the point of the surface code that when the stabilizer qubits are measured in step 8, the data qubits project to one of the four possible Bells states, and do not collapse. Measuring the stabilizer qubits would return $+1$ for a $|0\rangle$ state, and -1 for a $|1\rangle$ state. Thus the possible outcomes from measuring the stabilizers are

$$\begin{aligned}
\{+1,+1\} &\to |00\rangle + |11\rangle \\
\{-1,+1\} &\to |00\rangle - |11\rangle \\
\{+1,-1\} &\to |01\rangle + |10\rangle \\
\{-1,-1\} &\to |01\rangle - |10\rangle\,.
\end{aligned} \tag{B.6}$$

These are the possible quiescent states—recall we had no requirement what the initial state of $|q_a q_b\rangle$ should be, yet at the end of the cycle, we are guaranteed to get one of these possible states for the collective system. Furthermore, Starting from one of these quiescent states as an input for a cycle, it is easily shown that the output will be the same input

quiescent state, as is determined by the probability amplitudes in equation B.5. Errors that occur in the data qubits are then reflected by a change in the sign of the corresponding stabilizer qubit measurement, making the surface code capable of detecting errors without altering the state of the logical manifold.

APPENDIX C

SIMULATION DATA

This chapter lists simulation data for plots presented in the main text.

C.1 Error-divisible two-qubit gates

Tables C.1 and C.2 show the data used to generate the waveforms and results in Fig. 3.2 and Fig. 3.3. This set of data was obtained by numerically tuning the listed parameters for each individual two-qubit rotation. Note that for the really small gates (4 ns and smaller), this protocol starts to break down, thus we do not see a similar pattern in parameters choices determined by the numerical exploration.

We note that it would be convenient for a realization of this technique to use the same set of parameters for all partial rotations of a gate. For example, using device parameters for the current experimental realization—qubit nonlinearities $-0.16346 \times 2\pi$ GHz and $-0.254655 \times 2\pi$ GHz—and ignoring qubit energies in the rotating frame, if we modify equation 3.3 to $\Omega(t) = \Omega_0(t)\left[c + \alpha \sin(2\pi f)\right]$ such that c and α can be arbitrarily tuned, using equation 3.4a we can numerically find get the results in figure. C.1.

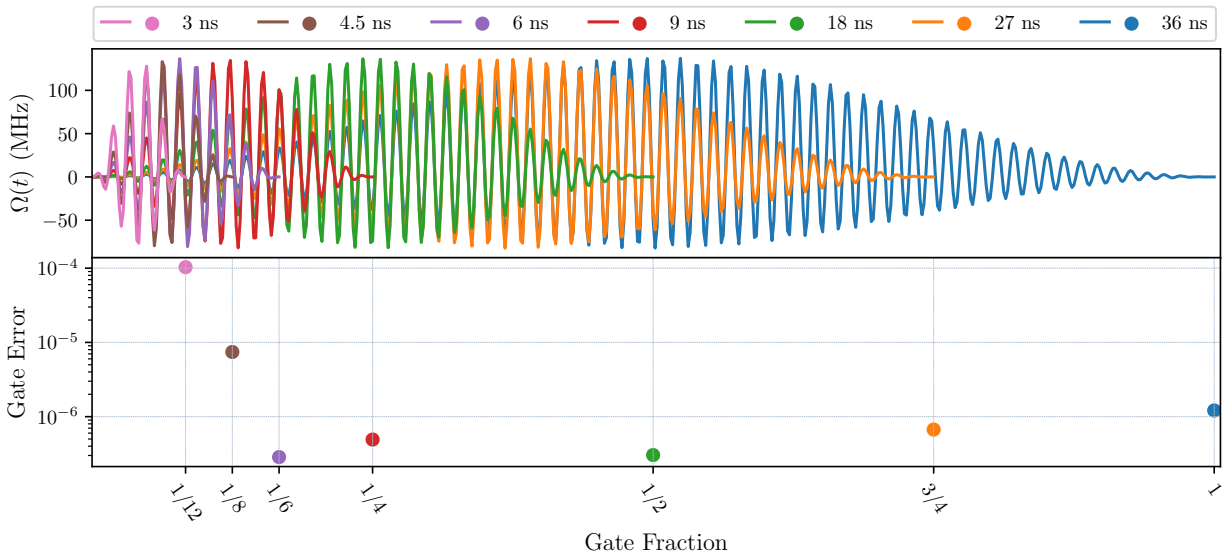

Figure C.1: Fractional gates using the same set of parameters. $\{A, f, \alpha, c\} = \{82.645 \text{ MHz}, 1.868 \text{ GHz}, 1.333, 0.336\}$ to generate the waveforms at the top, giving the gate errors $\{1.21, 0.67, 0.30, 0.49, 0.29, 7.43, 102.99\} \times 10^{-6}$, shown in the bottom.

Table C.1: Parameters for iSWAP waveform results in Fig. 3.2 and error rates in Fig. 3.3.

iSWAP waveforms

Cosine profile—Eq. 3.4a

		Non positive definite ($\alpha = 2$)			Positive definite ($\alpha = 1$)		
Fraction	t_g (ns)	A (MHz)	f (MHz)	Error (10^{-5})	A (MHz)	f (MHz)	Error (10^{-5})
1	36	13.91	-515.31	0.51	13.89	-377.61	5.93
3/4	27	13.91	-524.11	0.23	13.86	-374.14	0.44
1/2	18	13.87	-529.38	0.20	13.85	-410.17	14.67
1/4	9	13.84	-528.47	1.10	13.74	-528.06	17.98
1/5	6	13.77	-642.43	8.99	13.66	-644.62	16.67
1/8	4.5	13.04	-571.80	20.46	13.38	-548.56	8.46
1/12	3	10.25	-784.42	97.44	40.00	-183.81	113.59

Tangent profile—Eq. 3.4b

Fraction	t_g (ns)	A (MHz)	f (MHz)	γ	Error (10^{-5})	A (MHz)	f (MHz)	γ	Error (10^{-5})
1	36	8.82	-523.28	9.37	0.36	8.83	-369.09	9.35	0.49
3/4	27	10.17	-525.38	6.32	0.45	8.06	-384.34	13.99	4.67
1/2	18	10.59	-525.40	5.74	0.56	8.16	-363.04	12.67	1.63
1/4	9	9.94	-591.50	6.40	1.74	10.23	-458.40	6.11	7.09
1/5	6	14.92	-576.66	3.62	0.58	14.85	-565.25	3.63	7.58
1/8	4.5	9.58	-593.94	9.06	0.51	9.50	-603.31	7.79	3.87
1/12	3	6.94	-684.12	15.00	4.60	40.00	-167.78	6.87	1.11

Table C.2: Parameters for XX waveform results in Fig. 3.2 and error rates in Fig. 3.3. Note the smaller full gate time compared to iSWAP gates.

XX waveforms

Cosine profile—Eq. 3.4a

		Non positive definite ($\alpha = 2$)			Positive definite ($\alpha = 1$)		
Fraction	t_g (ns)	A (MHz)	f (MHz)	Error (10^{-5})	A (MHz)	f (MHz)	Error (10^{-5})
1	24	10.42	-854.11	7.11	10.42	-698. 30	20.21
3/4	18	10.42	-861.22	4.42	10.41	-717. 74	16.50
1/2	12	10.41	-850.74	2.88	10.39	-768. 57	11.88
1/4	6	10.32	-955.75	11.16	10.31	-961. 83	14.13
1/5	4	8.33	0.00	172.07	8.30	-923.54	171.03
1/8	3	6.27	0.00	191.99	40.00	-171.60	133.28
1/12	2	5.00	-9.06	123.77	40.00	-251. 10	83.48

Tangent profile—Eq. 3.4b

Fraction	t_g (ns)	A (MHz)	f (MHz)	γ	Error (10^{-5})	A (MHz)	f (MHz)	γ	Error (10^{-5})
1	24	7.66	-851.68	6.25	5.20	8.28	-715.89	5.38	20.31
3/4	18	10.08	-870.65	4.11	4.03	8.12	-752.41	5.56	16.74
1/2	12	6.62	-898.74	9.29	4.33	6.56	-801.57	9.52	9.59
1/4	6	12.52	-901.87	3.34	1.92	12.98	-909.24	3.24	5.21
1/5	4	6.34	-892.32	13.41	2.38	6.24	-903.65	13.65	2.29
1/8	3	5.18	0.00	15.00	66.43	5.18	0.00	15.00	66.43
1/12	2	5.00	-20.70	15.00	93.95	18.28	-250.01	8.09	79.21

Table C.3: Data for results plotted in Fig. 3.5, comparing the percent of the ground state energy that each type of gate set is able to produce.

Number of qubits	Stock	Continuous	Error-divisible
4	0.507243	0.575992	0.817031
6	0.509382	0.585032	0.802391
8	0.512273	0.59149	0.770956
10	0.514339	0.59568	0.757204
12	0.515807	0.598545	0.754664

APPENDIX D

MISCELLANEOUS REFERENCES

I list here a collection of useful references that will hopefully aid in clarifying some content in the main text that cannot be easily clarified with external references.

D.1 Rotating Frame Hamiltonian derivation for two-qubit system

We explicitly derive the rotating frame Hamiltonian (Eq. 3.1) for the two coupled qubits. Starting from the two coupled qubits with energies ω_1, ω_2, and nonlinearity δ, the system is described by the Duffing oscillator Hamiltonian in the energy basis as well as a coupling Hamiltonian,

$$H = \omega_1 \hat{n}_1 + \omega_2 \hat{n}_2 - \frac{\delta}{2}\left(a_1^\dagger a_1^\dagger a_1 a_1 + a_2^\dagger a_2^\dagger a_2 a_2\right) + g(t)\left(a_1^\dagger + a_1\right)\left(a_2^\dagger + a_2\right), \tag{D.1}$$

with $\hat{n}_j = a_j^\dagger a_j$, $g(t) = g_0 A(t)\cos(2\pi(\omega_1 - \omega_2)t)$, and we have let $\hbar = 1$. Recognizing this Hamiltonian with a time-independent and time-dependent parts, $H(t) = H_0 + V(t)$, this obeys the Schrödinger equation $i\partial_t |\psi(t)\rangle = H(t)|\psi(t)\rangle$. We apply a unitary rotation transformation $U_R(t)$ such that a new state can be defined

$$|\phi(t)\rangle = U_R(t)|\psi(t)\rangle . \tag{D.2}$$

Looking at the time evolution of $|\phi(t)\rangle$,

$$\begin{aligned} i\partial_t |\phi(t)\rangle &= i\partial_t \left(U_R(t)|\psi(t)\rangle\right) \\ &= i\partial_t U_R(t)|\psi(t)\rangle + U_R(t)(i\partial_t |\psi(t)\rangle) \\ &= i\dot{U}_R(t)|\psi(t)\rangle + U_R(t)H(t)|\psi(t)\rangle \\ &= i\dot{U}_R(t)U_R^\dagger(t)|\phi(t)\rangle + U_R(t)H(t)U_R^\dagger(t)|\phi(t)\rangle , \end{aligned} \tag{D.3}$$

where we have used D.2 to replace $|\psi(t)\rangle = U_R^\dagger(t)|\phi(t)\rangle$. From here, it's clear that the state $|\phi(t)\rangle$ also obeys the Schrödinger equation with a modified Hamiltonian

$$i\partial_t |\phi(t)\rangle = \left(i\dot{U}_R(t)U_R^\dagger(t) + U_R(t)H(t)U_R^\dagger(t)\right)|\phi(t)\rangle . \tag{D.4}$$

This is our rotating frame Hamiltonian $i\partial_t |\phi(t)\rangle = H_R(t) |\phi(t)\rangle$. Separating the time dependent part of the Hamiltonian D.1, we express $H_R(t)$ as

$$H_R(t) = i\dot{U}_R(t)U_R^\dagger(t) + U_R(t)H_0U_R^\dagger(t) + U_R(t)V(t)U_R^\dagger(t), \tag{D.5}$$

allowing us to separate this problem into solving three smaller parts. Letting $U_R(t) = e^{i(\omega_1\hat{n}_1+\omega_2\hat{n}_2)t}$, we have

$$i\dot{U}_R(t)U_R^\dagger(t) = -(\omega_1\hat{n}_1 + \omega_2\hat{n}_2) \tag{D.6a}$$

$$U_R(t)H_0U_R^\dagger(t) = \omega_1\hat{n}_1 + \omega_2\hat{n}_2 - \frac{\delta}{2}\left(a_1^\dagger a_1^\dagger a_1 a_1 + a_2^\dagger a_2^\dagger a_2 a_2\right) \tag{D.6b}$$

$$U_R(t)V(t)U_R^\dagger(t) = -g(t)\left(a_1^\dagger e^{i\omega_1 t} + a_1 e^{-i\omega_1 t}\right)\left(a_2^\dagger e^{i\omega_2 t} + a_2 e^{-i\omega_2 t}\right) \tag{D.6c}$$

where we have used the relations $a^\dagger e^{-i\omega\hat{n}t} = e^{i\omega\hat{n}t}a^\dagger e^{i\omega t}$ and $ae^{-i\omega\hat{n}t} = e^{i\omega\hat{n}t}ae^{-i\omega t}$. Replacing $g(t)$ (ignoring 2π and using $\cos[(\omega_1 - \omega_2)t]$ for the moment) and using Euler's formula, D.6c becomes

$$\begin{aligned} U_R(t)V(t)U_R^\dagger(t) = -\frac{g_0}{2}A(t)\Big(&a_1^\dagger a_2^\dagger e^{2i\omega_1 t} + a_1^\dagger a_2 e^{2i(\omega_1-\omega_2)t} + a_1 a_2^\dagger \cancel{e^{0}}^{1} + a_1 a_2 e^{-i2\omega_2 t} \\ &+ a_1^\dagger a_2^\dagger e^{2i\omega_1 t} + a_1^\dagger a_2 \cancel{e^{0}}^{1} + a_1 a_2^\dagger e^{-2i(\omega_1-\omega_2)t} + a_1 a_2 e^{-2i\omega_1 t}\Big). \end{aligned} \tag{D.7}$$

Making the rotating wave approximation, we can toss all fast-oscillating terms and keep slow-oscillating and stationary ones. Note that if ω_1 and ω_2 are close or far apart only changes the final result by a factor of 2 under the approximation, since the terms oscillating at $(\omega_1 - \omega_2)$ are the same as the stationary ones. Putting together D.6 and D.7, our approximated, rotating frame Hamiltonian is

$$H_{\mathrm{RF}} = -\frac{\delta}{2}\left(a_1^\dagger a_1^\dagger a_1 a_1 + a_2^\dagger a_2^\dagger a_2 a_2\right) - A(t)g_0\left(a_1^\dagger a_2 + a_1 a_2^\dagger\right). \tag{D.8}$$

Letting $H_{RF} = H_0 + H_1$, with $H_0 = \frac{\delta}{2}\left(a_1^\dagger a_1^\dagger a_1 a_1 + a_2^\dagger a_2^\dagger a_2 a_2\right)$ and $H_1 = -A(t)g_0\left(a_1^\dagger a_2 + a_1 a_2^\dagger\right)$, we perturbatively find the effective Hamiltonian, treating $A(t)$ as fixed for the moment. Ignoring states of higher energy than $|2\rangle$, the eigensystem for H_0 is given by

$$0\{|0_1 0_2\rangle, |0_1 1_2\rangle, |1_1 0_2\rangle, |1_1 1_2\rangle\}, -\delta\{|0_1 2_2\rangle, |2_1 0_2\rangle, |1_1 2_2\rangle, |2_1 1_2\rangle\}, -2\delta|2_1 2_2\rangle. \tag{D.9}$$

Since the action of H_1 on any $|2\rangle$ state results in a $|3\rangle$ state, we ignore any corrections on those and focus on perturbative corrections for the $|0\rangle, |1\rangle$ subspace (0 eigenenergy states in D.9). Because these are degenerate, we diagonalize the perturbing Hamiltonian H_1 in this unperturbed eigenstate $|n^0\rangle$ subspace. Building out the $\langle n_i^0| H_1 \left|n_j^0\right\rangle$ matrix, we get

$$\begin{pmatrix} 0 & 0 & 0 & 0 \\ 0 & 0 & -A(t)g_0 & 0 \\ 0 & -A(t)g_0 & 0 & 0 \\ 0 & 0 & 0 & 0 \end{pmatrix}, \tag{D.10}$$

giving us the first-order corrections to the degenerate states

$$0(|0_1 0_2\rangle, |1_1 1_2\rangle), \pm\frac{A(t)g_0}{\sqrt{2}}(|1_1 0_2\rangle \mp |0_1 1_2\rangle). \tag{D.11}$$

The only state in this subspace with a non-zero, second order correction is $|1_1 1_2\rangle$, yielding $|0_1 2_2\rangle$ and $|2_1 0_2\rangle$ upon the action of H_1, giving us

$$\frac{4A(t)^2 g_0^2}{\delta} |1_1 1_2\rangle. \tag{D.12}$$

Eliminating second-excited energy states now $\left(a^\dagger \to \sigma^+,\ a \to \sigma^-\right)$, and up to second order in perturbation theory—combining D.11 and D.12, we get the effective Hamiltonian

$$H \simeq -A(t)g_0\left(\sigma_1^+\sigma_2^- + \sigma_1^-\sigma_2^+\right) + \frac{A(t)^2 g_0^2}{\delta}(1+\sigma_1^z)(1+\sigma_2^z). \tag{D.13}$$

This dispersive shift gives an effective CZ and partial iSWAP. To counter this, we can choose $A(t) = A_0(t)[1 + B\sin(2\pi f t)]$, where $A_0(t)$ is a slow-evolving wave envelope. Given $f \gg g_0$, the leading exchange term in D.13 remains unaffected, while the oscillatory effects create off-resonant dispersive shifts that counter the effects of the $\sigma_1^z\sigma_2^z$ term.

D.2 Circuit implementations for SWAP and iSWAP gates

We use the following notation:

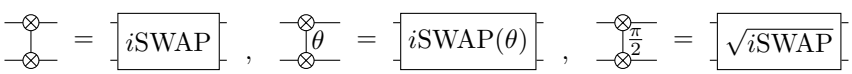

where $i\text{SWAP}(\theta) = \exp\left[i\theta/2\left(\sigma_1^+\sigma_2^- + \sigma_1^-\sigma_2^+\right)\right]$, with a full $i\text{SWAP} = i\text{SWAP}(\pi)$, and $\sqrt{i\text{SWAP}} = i\text{SWAP}(\pi/2)$. Using a stock native gate set—with CNOT as the base two-qubit gate, we can implement the two-qubit SWAP and iSWAP gates.

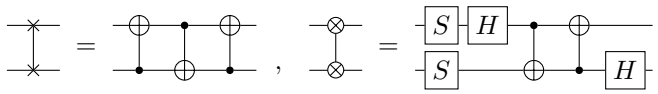

With access to a broader set of native two-qubit gates, arbitrary two-qubit gates can be implemented more efficiently. For example, with access to a native $\sqrt{i\text{SWAP}}$, we can achieve the lowest-error implementation of SWAP that the authors are aware of from [104],

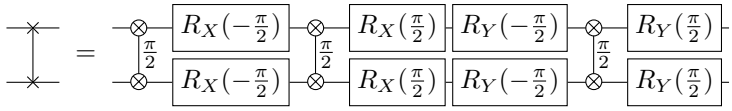

This explicitly demonstrates the benefit of having access to a native partial gate like $\sqrt{i\text{SWAP}}$ for implementation of other two-qubit gates. More broadly, any arbitrary $i\text{SWAP}(\theta)$ rotation can be implemented using native $\sqrt{i\text{SWAP}}$ gates,

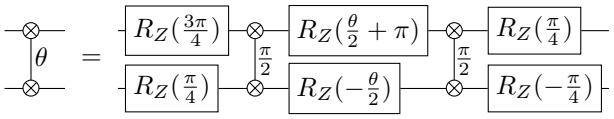

This decomposition highlights the benefit of having access to a native set of arbitrary θ rotations that would allow the reduction of two-qubit gate error proliferation, as well as energy loss by virtue of spending less time on a single gate.

D.3 The Clifford group

The Clifford group is defined as the set of gates that normalizes the Pauli group P_n, where P_1 is simply the group of pauli matrices

$$P_1 = \pm(1, i)\{\sigma^0, \sigma^x, \sigma^y, \sigma^z\}, \tag{D.14}$$

with $\sigma^0 = I$ being the 2×2 identity matrix. For n-qubits, we can more generally write

$$P_n = \left\{ e^{i\theta\pi/2} \bigotimes_{m=1}^{n} \sigma_m^k \;\middle|\; \theta = 0, 1, 2, 3, \text{and } k = 0, x, y, z \right\}. \tag{D.15}$$

Thus for the Clifford group, we have

$$C_n = \left\{ U \mid \forall P \in P_n,\ UPU^\dagger \in P_n \right\}. \tag{D.16}$$

Note that the set $\{\sigma^x, \sigma^z\}$ is sufficient to generate P_n, and the set $\{S, H, \text{CNOT}\}$ generates C_n as well as P_n, where S is the phase gate

$$S = \begin{pmatrix} 1 & 0 \\ 0 & e^{i\pi/2} \end{pmatrix} = \begin{pmatrix} 1 & 0 \\ 0 & i \end{pmatrix}, \tag{D.17}$$

H is the Hadamard gate

$$H = \frac{1}{\sqrt{2}} \begin{pmatrix} 1 & 1 \\ 1 & -1 \end{pmatrix}, \tag{D.18}$$

and CNOT is the two-qubit controlled-NOT gate

$$\text{CNOT} = \begin{pmatrix} 1 & 0 & 0 & 0 \\ 0 & 1 & 0 & 0 \\ 0 & 0 & 0 & 1 \\ 0 & 0 & 1 & 0 \end{pmatrix}. \tag{D.19}$$

The set of Clifford gates is of particular interest because the Gottesman-Knill theorem states that a quantum circuit composed of only Clifford gates can be simulated efficiently on a classical computer, and thus much of the research effort in quantum gates focuses on implementations of Clifford gates. Lastly, note that the Clifford group does not provide a universal set of stock gates for quantum computing. However, with the addition of the $\frac{\pi}{8}$ gate,

$$T = \frac{\pi}{8} = e^{i\pi/8} \begin{pmatrix} e^{-i\pi/8} & 0 \\ 0 & e^{i\pi/8} \end{pmatrix} = \begin{pmatrix} 1 & 0 \\ 0 & e^{i\pi/4} \end{pmatrix}, \tag{D.20}$$

the Clifford group does form a universal gate set.

APPENDIX E

PERMISSIONS FOR COPYRIGHTED MATERIAL

E.1 License for figure 1.6

The figure in section 1.3.1 is licensed under a Creative Commons license CC BY 4.0, specified in the supplemental file "catCodeFigure_license.pdf", also found in https://creativecommons.org/licenses/by/4.0/legalcode. Among other things, it grants a worldwide, royalty-free, irrevocable license to reproduce and share the licensed material (figure 1.6), on the condition of granting attribution ([2]).

E.2 License for chapter 2

The entirety of chapter 2 is reproduced from IOP Quantum Science and Technology, licensed by the Copyright Clearance Center CCC, granting permission for the republication of the entirety of the article. The license is specified in the supplemental file "improvedEC_license.pdf", and can be found at https://marketplace.copyright.com/rs-ui-web/mp/license/5c7d5ac9-60e1-4e7b-8580-d813f3d7de8c/7cc48563-ea5f-46bd-9627-92b51a6b21ca.